Hydrogen Absorption Properties in High Entropy Alloys Containing Refractory Elements

Anis Bouzidi

Thesis

to obtain the degree of

Doctor of Philosophy from University of Paris-Est Créteil

Speciality in **Materials Science**

Hydrogen Absorption Properties in High Entropy Alloys Containing Refractory Elements

Submitted by

Anis BOUZIDI

Thesis defended: November 14th, 2023

Jury :

Pr. Jean-Louis BOBET	University of Bordeaux, ICMCB, CNRS, Pessac	President
Dr. Patricia de RANGO	Institut Néel, CNRS, Grenoble	Reviewer
Pr. Frédéric PRIMA	Chimie ParisTech, IRCP, CNRS, Paris	Reviewer
Pr. Lotfi BESSAIS	University of Paris-Est Créteil, ICMPE, CNRS, Thiais	Examiner
Dr. Claudia ZLOTEA	ICMPE, CNRS, Thiais	Supervisor

Summary

Hydrogen as a clean energy carrier has become a viable idea to achieve the decarbonization of the energy sector. As an energy carrier, hydrogen needs to be produced, transported stored, and used in stationary and mobile applications. However, the implementation of a full scale economy based on hydrogen requires more efforts to overcome the technical issues related to its storage. Among the various types of ways to store hydrogen, the solid-state storage in the form of metal hydrides presents a safe and promising solution.

The aim of this project is to investigate a new class of functional materials for solid-state hydrogen storage named High entropy alloys (HEAs). The possible combinations in the multidimensional space of HEAs are extremely broad, which makes experimental research difficult to organize. This project proposes a novel strategy of adding 10% of a fifth element *M* (with *M* = Mg, Al, Cr, Mn, Fe, Co, Ni, Cu, Zn, Mo, and Ta) to the quaternary alloy $Ti_{0.325}V_{0.275}Zr_{0.125}Nb_{0.275}$. An investigation of the effects of the chemical composition on the hydrogen sorption properties will be conducted and a comparison between the novel alloys and the parent material will be drawn. Different methods of synthesis are employed such as arc melting, ball milling, and reactive ball milling to obtain *bcc* single phased HEAs. Moreover, correlations are established between empirical parameters such as the atomic size mismatch (δ) and the valence electron concentration (VEC), and the hydrogen sorption properties i.e., the maximum capacity of hydrogen uptake, the onset temperature of hydrogen release, lattice parameters (for the as-cast alloys and their hydrides), and the volume expansion following hydrogenation. Furthermore, an in-depth investigation of selected HEAs with the highest capacity of hydrogen absorption will be studied using various characterization techniques regarding the structural transitions upon desorption of hydrogen, hydrogen cycling properties, and the thermodynamics of hydrogenation.

The novel proposed methodology allowed to rationalize the effect of the chemical composition of this series of HEAs on the hydrogen storage performances.

Keywords: Hydrogen storage, high entropy alloys, hydrides, empirical parameters.

Résumé

L'hydrogène en tant que vecteur d'énergie est devenu une idée envisageable pour atteindre la décarbonisation du secteur de l'énergie. Cependant, l'hydrogène doit être produit, transporté, stocké afin d'être utilisé dans des applications stationnaires et mobiles. Néanmoins, la mise en œuvre d'une économie à grande échelle basée sur l'hydrogène nécessite davantage d'efforts pour surmonter les problèmes techniques liés à son stockage. Parmi les différents types de stockage de l'hydrogène, le stockage à l'état solide sous forme d'hydrures métalliques constitue une solution sûre et prometteuse.

Ce mémoire de thèse vise à étudier les propriétés de stockage de l'hydrogène à l'état solide d'une nouvelle classe de matériaux fonctionnels appelée alliages à haute entropie (AHE). Les possibilités de combinaison de ces AHE sont très vastes et par conséquent beaucoup de recherches expérimentales sont indispensables afin d'éclaircir la relation entre la composition chimique de ces matériaux et leurs propriétés de sorption de l'hydrogène. Ce projet propose une nouvelle stratégie qui consiste à étudier l'effet de l'addition de 10% d'un cinquième élément *M* (avec *M* = Mg, Al, Cr, Mn, Fe, Co, Ni, Cu, Zn, Mo, et Ta) à un alliage quaternaire $Ti_{0.325}V_{0.275}Zr_{0.125}Nb_{0.275}$. Une étude des effets de la composition chimique sur les propriétés de sorption de l'hydrogène a été réalisé et comparé entre les nouveaux alliages et le matériau quaternaire. Trois méthodes de synthèse différentes ont été utilisées pour la préparation de ces alliages : fusion à l'arc, broyage mécanique sous gaz inerte (Ar) et broyage mécanique sous gaz réactif (H_2). De plus, des corrélations ont été établies entre les paramètres empiriques tels que l'écart quadratique moyen des rayons atomiques noté δ et la concentration d'électrons de valence (VEC) avec les propriétés de sorption de l'hydrogène i.e., la capacité maximale d'absorption de l'hydrogène, la température de désorption de l'hydrogène, les paramètres de mailles (alliages et leurs hydrures) et l'expansion volumique après l'hydrogénation. Par ailleurs, une étude approfondie sur les alliages ayant la plus grande capacité d'absorption d'hydrogène a été menée en utilisant diverses techniques de caractérisation pour caractériser les transitions de phases lors de la désorption de l'hydrogène, les propriétés de cyclage de l'hydrogène et les propriétés thermodynamiques d'hydrogénation.

La nouvelle méthodologie proposée a permis de mettre en évidence l'effet de la composition chimique des AHEs sur les performances de stockage de l'hydrogène.

Mots-clés : Stockage de l'hydrogène, alliages à haute entropie, hydrures, paramètres empiriques.

Table of content

Remerciement

Je tiens à remercier Madame Patricia DE RANGO, directrice de recherche à l'Institut Néel de Grenoble, ainsi que Monsieur Frédéric PRIMA, Professeur de l'Institut Chimie ParisTech à Paris, pour avoir accepté d'évaluer et rapporter cette thèse. Je remercie également Monsieur Jean-Louis BOBET, Professeur à l'université de Bordeaux, et Monsieur Lotfi BESSAIS, Professeur à l'université Paris-Est Créteil, d'avoir accepté de faire partie de mon jury de thèse.

Je remercie chaleureusement Madame Claudia ZLOTEA, chercheuse à l'Institut de Chimie et des Matériaux Paris-Est, pour la confiance qu'elle m'a accordée, pour toutes les connaissances partagées, pour sa rigueur et son exigence dans le travail, pour ses conseils et ses qualités humaines qui ont été précieux pour l'accomplissement de ce travail.

Je remercie également tous les membres de l'Institut de Chimie et des Matériaux Paris-Est, qui m'ont apporté leurs aides en particulier Fabrice COUTURAS, Valérie LALANNE, Benjamin VILLEROY, Olivier ROULEAU et Rémy PIRES.

Je remercie Gladys BERNARI, Dominique ALAIN et Marcelle AMMOUR pour leur aide et pour les démarches administratives.

Je tiens à remercier tous les Stagiaires, Doctorants et Docteurs que j'ai côtoyés et qui ont contribué à la bonne atmosphère de la vie au laboratoire. Certains sont encore là, d'autres partis. Je tiens à remercier particulièrement : Hamdi, Jorge, Wang, Anna, Bruno, Maxime, Abou, Raihana, Nayely, Hao, Jihed, Faye, Ghofrane, Hugo, Julie, Yona, Wissal, Runan, Sébastien, Vladimir, Zeineb, Agustine, Yaxin et 'Julien'. Je remercie également Minh que j'ai connu depuis notre Master MAN et je lui souhaite de très bonne chance pour le futur.

Enfin, mes derniers et plus particuliers remerciements vont à ma famille et mes proches : mes parents et ma petite sœur qui m'ont toujours soutenus, mes grands-parents pour tout l'amour que vous m'avez toujours prodigué, mon frère Wassim sans qui je ne serais pas ce que je suis aujourd'hui, Sami mon cher oncle qui m'a encouragé et m'a aidé sur tous les plans, Aicha ma fiancée pour son amour et son soutien, Yassine pour ses encouragements et sa présence durant toutes ces années, Ghassen pour tous les bons moments partagés ensemble et Momo pour ses conseils, encouragements et les riches discussions.

CHAPTER I

Introduction

In the 21st century, humankinds biggest challenge is the over-reliance on fossil fuels as a primary energy source. Fossil fuels are non-renewable energy sources, and the rate of their consumption is exponentially fast. For example, petroleum (crude oil) is a fossil fuel that is formed from the remains of ancient marine substances (algae, plants...). The transformation of these organic remains to petroleum takes millions of years of intense heat and pressure, hence, their reserves are consumed faster than the rate of their formation. The fossil fuels production, transport, and use has led to enormous environmental pollution. The reaction of combustion of these energy sources generates air pollutants such as CO_2, CH_4, and SF_6. They are considered as primary greenhouse gases and they represent one of the main gases responsible for climate change. A shift from fossil fuels to renewable energy sources must take place to avoid the long term climate risks. In 2015, 196 Parties at the UN Climate Change Conference agreed to the Paris agreement [1]. The aim of the agreement is to keep the global warming well below 2 °C. By ensuring an energy transition for the long-term, greenhouse gas emission will be reduced. Consequently, to achieve net zero emissions, it is crucial to shift from fossil fuels to the use of renewable energy sources such as biomass, geothermal resources, sunlight, and more interestingly hydrogen as an energy vector which has been hailed as the ‘fuel of the future’.

1. Energy vector: Hydrogen

Hydrogen is the most abundant chemical element in the universe. Under ambient temperature and pressure conditions, hydrogen is a light gas with a density of 0.08988 kg/m^3. Pure hydrogen is odorless, colorless, tasteless, non-toxic, and highly flammable. The energy density of hydrogen is the highest of all the fuels (142 MJ/Kg) (figure 1.1) [2]. On earth, pure hydrogen is very scarce, and it mainly exists combined with other elements such as carbon or oxygen forming hydrocarbons or water. In the burning process, hydrogen will produce only water by the reaction with oxygen. Therefore, there’s no pollution products from hydrogen combustion. For all the mentioned reasons, hydrogen is a great candidate as a clean energy carrier. The three main segments for building an infrastructure of hydrogen are production, storage/distribution, and utilization. The main disadvantage for the efficient utilization of hydrogen as an energy carrier is its low volumetric energy density. For an efficient, higher energy density, and cost effective characteristics, storage methods need to be developed to achieve the full potential of hydrogen under safe and mild operating conditions.

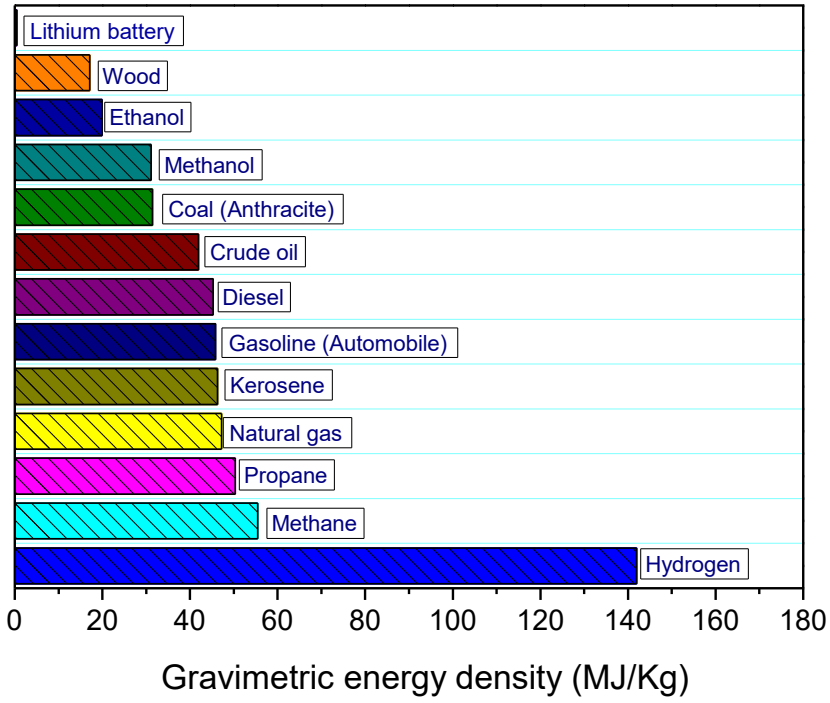

Figure 1.1. Gravimetric energy density of some fuels.

The objective of storage technologies is to contain hydrogen in safe, effective, and a compact volume for a future use under mild conditions. There are three modes to store hydrogen and they can be categorized *via* the hydrogen bond with the material of storage: (a) no bonding with the containing material, (b) van der Waals bonding, and (c) chemical bonding.

1.1 Hydrogen storage technologies

Hydrogen storage materials are evolving each year and they are classified into three categories by the nature of the hydrogen bonding with its container:

a) The first mode is the storage of hydrogen in its pure molecular form without any type of physical or chemical bonding with the containing material. At a large scale, the most employed way is hydrogen storage in the form of gas or liquid. Hydrogen gas if compressed at 100 bar and 20°C, its density will be 7.8 kg/m^3 which is considered as low density to be used as a fuel. Furthermore, tanks that are used commercially store hydrogen at 700 bar (density = 39 kg/m^3) and this type of tank is expensive to be manufactured [3]. Additionally, using tanks of compressed H_2 in mobile application is considered as a huge risk due to explosions, even when there is a small leak. Another way to increase the hydrogen density in tanks is by liquefaction of hydrogen [3].

Hydrogen in the liquid form can reach a density of 70 kg/m^3 at 1 bar. The transformation from gaseous to liquid state takes place by decreasing the temperature until reaching -253°C at 1 bar of pressure. The concern about liquification of hydrogen is the need of high energy investment to reach and maintain low temperatures (cryogenic). Cryogenic tanks must be thermally well insulated to avoid hydrogen boil off (transformation of liquid hydrogen to gas). Nevertheless, liquid hydrogen density is still low but fulfills the energetic needs for stationary applications.

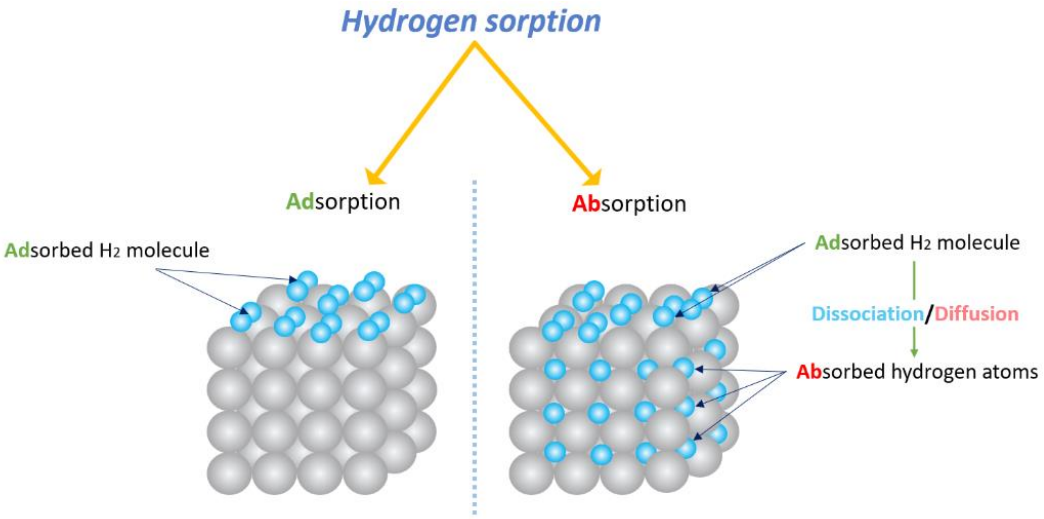

Figure 1.2. Schematic representation between hydrogen **ad**sorption and **ab**sorption.

b) The second mode is when hydrogen is bonding *via* a van der Waals bond with a material that possess an important specific surface area. In this type of storage, hydrogen is **ad**sorbed (*via* physisorption) on solid nano-porous materials such as, activated carbon [4], metal-organic frameworks (MOFs) [5], and zeolites [6]. These materials are known as adsorbents, and they possess a high specific surface and an important porous volume which is the main characteristic feature for a maximum gravimetric capacity. As illustrated in figure 1.2, the **ad**sorption occurs without any modification of the hydrogen molecule and presents excellent reversibility and fast kinetics during **ad**sorption/desorption. However, due to the weak hydrogen bonding between the H_2 molecule and the host material, non-standard conditions need to be applied to achieve an important hydrogen density. Hence, cryogenic temperatures (-196°C) are required using liquid nitrogen and pressures between 10 to 100 bar.

c) The third mode is when hydrogen is stored in a solid material *via* **ab**sorption by forming chemical bonds between the hydrogen atoms and the material. Prior to the absorption, the H_2 molecules are dissociated at the surface, followed by the

penetration of hydrogen atoms to the subsurface, and finally diffusion throughout the crystal lattice of the host material (figure 1.2). The resulting material of this process is known as a metal hydride (the hydride formation process will be thoroughly developed in chapter II). Metal hydrides are classified *via* the nature of the chemical bond between the metal and hydrogen. These bonds are stronger than the van der Waals bond, therefore, more energy is needed to release the hydrogen. Nevertheless, the strong bonds permit hydrogen to be condensed more at standard conditions. There are three types of hydrides, depending on the nature of bonding:

1- Metallic hydrides: by definition, hydrogen is bonded to metal atoms *via* a metallic bond. Hydrogen will occupy interstitial positions because of its small volume as illustrated in figure 1.3.

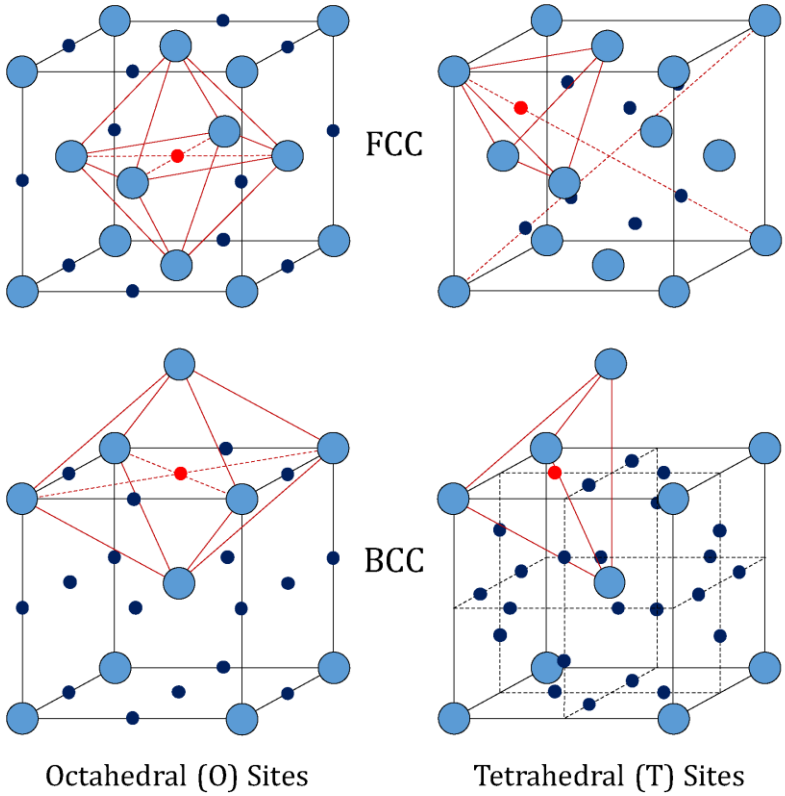

Figure 1.3. Example of possible hydrogen atoms interstitial occupation sites (Octahedral (O) and Tetrahedral (T)) inside a body centered cubic (*bcc*) (bottom) and a face centered cubic (*fcc*) host metal (top) [7].

The most studied alloys are body centered cubic (*bcc*) ($Im\bar{3}m$) and intermetallic AB type compounds. At standard pressure and temperature conditions, “A” stands for an element forming a stable hydride, whereas “B” is a non-hydride forming element.

The hydrogen storage capacities of these materials differ depending on the properties of each composition. Intermetallics such as, $LaNi_5$ and FeTi can reach a maximum hydrogen uptake of 1.4 wt.% and 1.89 wt.%, respectively [8]. Furthermore, *bcc* alloys such as, TiV_2 and $V_{40}Ti_{21.5}Cr_{38.5}$ absorb hydrogen reaching maximum capacity of 2.6 wt.% [8] and 2.44 wt.% [9], respectively.

2- Ionic hydrides: The reaction of hydrogen with alkali and alkaline earth metals will result in hydrogen accepting an electron from the metal forming an H^- ion and the ionic bond is created. Ionic hydrides have a high melting and boiling temperatures. A known ionic hydride is MgH_2 that was subject of numerous studies for its high hydrogen storage capacity of 7.6 wt.% and its good reversibility [10]. However, the material suffers from slow kinetics and high thermodynamic stability, thus limiting its practical applications.

3- Complex hydrides: Hydrogen will form a covalent bond with metallic or non-metallic elements, forming a complex anion such as, NH_2^-, BH_4^-, and AlH_4^- [11]. The anion is then balanced by a cation, generally a lightweight element from alkaline earth or alkali groups resulting in having a mixture of both ionic and covalent bonds. This enables the hydride to have a high gravimetric hydrogen storage uptake. The most studied complex hydride is alanate ($NaAlH_4$) with a reversible storage capacity of 5.6 wt.% [12]. However, the dehydrogenation (decomposition) process is done in multi-steps and with very slow kinetics making the complex hydrides impractical for mobile applications.

Storage technology	Liquid hydrogen tank	Cryo-adsorption	Interstitial Metal hydride	Compressed hydrogen	Alanate	Salt like metal hydride
	LH_2	Activated carbon, MOFs	$FeTiH_x$/ $LaNi_5H_x$	CGH_2	$NaAlH_4$	MgH_2
						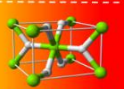
Type of bond	No bond 	Van der Waals 	Metallic bond 	No bond 	Covalent bond 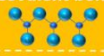	Ionic bond 
Capacity of storage	100 wt.%	6.5 wt.%	2.0 wt.%	100 wt.%	5.5 wt.%	7.5 wt.%
Operating temperature (°C)	-253	> -200	0-30	25	70-170	330
Corresponding energy to release hydrogen (MJ/Kg)	0.45	3.5	15	n/a	23	37

Figure 1.4. Hydrogen storage technologies and their corresponding characteristics (LH_2: liquid hydrogen; CGH_2: compressed gas of hydrogen) (inspired from reference [13]).

Figure 1.4 summarizes all the presented modes of the available technologies with their corresponding type of hydrogen bonding, storage capacity, and operational conditions.

1.2 Solid-state hydrogen storage

From all the presented modes for hydrogen storage, solid-state hydrogen storage is the most promising mode. In fact, hydrides present many advantages when compared to other modes such as, high volumetric density than gaseous or liquid (cryogenic) storage: 110 kg/m^3 for MgH_2 > 70 kg/m^3 for liquid hydrogen at -253°C > 39 kg/m^3 for gaseous storage at 700 bar. Another advantage for using hydrogen in mobile applications, for example, hydrides working conditions are near standard temperature and pressure (STP) conditions. Hence, safety is much better when compared to gaseous or liquid hydrogen tanks. All the above mentioned advantages are perfect if they exist in one single material candidate, but they are spread among different types of materials. As a matter of fact, depending on the nature of the hydride the disadvantages vary: ionic and complex hydrides suffer from unfavorable thermodynamics, for instance, most of the complex hydrides require high desorption temperatures, furthermore, due to their stability, the desorption of hydrogen requires the use of suitable catalysts [14]. The MgH_2 hydride needs to be heated above 300°C for hydrogen desorption. Even though metallic hydrides have a reversible reaction near STP, they have low gravimetric capacities (example: TiFe) and suffer from degrading capacities during hydrogen absorption/desorption cycles.

To summarize, hydrides are very promising candidates that ensure the requested criteria for an efficient hydrogen storage way despite the disadvantages that each type of hydride suffers from. Our main strategy is to be able to mix multiple elements and vary their nature and stoichiometry to fulfill multiple criteria and overcome the drawbacks previously mentioned. Therefore, materials with multiple elements might present a promising strategy for hydrogen storage.

1.3 High Entropy Alloys

Since the bronze age, the concept of metal alloying was applied in everyday life to produce various alloys such as, brass, bronze, and steel. Nowadays, the concept of mixing metals is known as conventional alloying which is based on the use of a single principal element and adding small amounts of different elements to upgrade the mechanical properties (figure 1.5 (left)). The research was generally focused on improving the properties of conventional alloys by changing the nature of the added elements or the number of

substitutions. In 2004, a novel paradigm emerged from two independent studies. Yeh *et al.* and Cantor *et al.* reported the first two multicomponent alloys $CuCoNiCrAl_xFe$ [15] and FeCrMnNiCo [16] respectively. These alloys formed simple structures which wasn't expected. In contrast to conventional alloys, this new metallurgical concept is based on multicomponent materials with at least five elements, named high entropy alloys (HEAs) (figure 1.5 (right)). Until now, researchers still define them *via* two different ways. The first way is to define HEAs based on composition, on the other hand, others define HEAs by their entropy. The main motivation of HEAs research is the ability of mixing multiple elements which form a single phase solid solution with the prediction of creating an alloy with superior properties.

The first definition of HEAs emerged from the work of Yeh *et al.* in 2004 [15]. The HEAs were defined by composition. It states that compositions containing at least five elements with the concentration of each element being between 5-35 at.% of the alloy is considered an HEA. This definition is only based on composition and neither includes entropy, nor the type of solid solution formed phase.

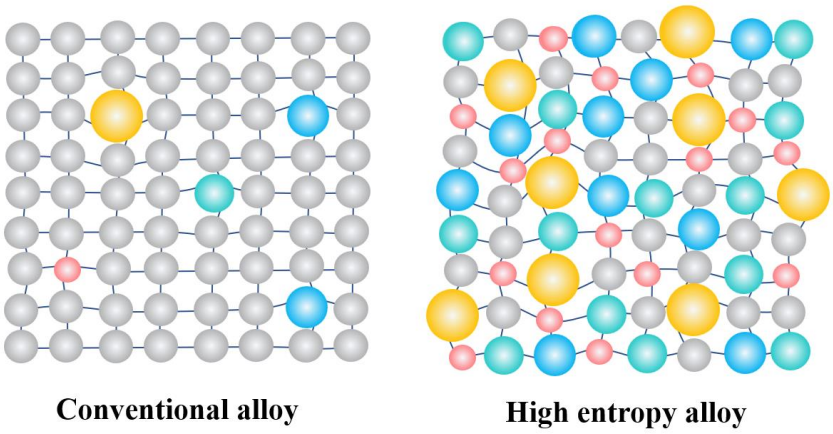

Figure 1.5. Schematic representation of the difference between conventional (left) and high entropy alloys (right).

The second definition is based on the value of the alloy's entropy [17]. The evaluation of the entropy of non-equimolar alloys is provided from the configurational entropy of an alloy (ΔS_{config}) that is calculated from the following formula:

$$\Delta S_{config} = -R \sum_{i=1}^{n} X_i ln X_i \qquad \text{Equation 1.1}$$

Where X_i represents the mole fraction of the i^{th} element and R is the gas constant. Hence, the classification of alloys depends on the value of the configurational entropy of each

composition. For low entropy alloys, $\Delta S_{config} \leq 1R$, whereas for medium entropy alloys $1R \leq \Delta S_{config} \leq 1.5R$, and the configuration entropy for HEAs is $\Delta S_{config} \geq 1.5R$ (as illustrated in figure 1.6).

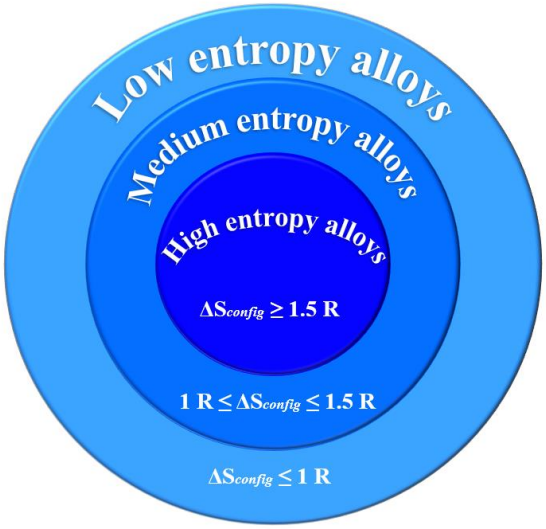

Figure 1.6. Classification of alloys based on their entropy of configuration.

HEAs could be also directly defined by the inability to discriminate between major or minor elements, hence, all the elements in a HEA are equally important without discerning between major and minor elements, contrary to conventional alloys. A systematic study of reported HEAs proposed that the mixture of at least five principal elements results in four core effects [18]:

1- The high entropy effect dictates that the high configurational entropy from the mixing of at least five elements could lead to simplifying the structure to only obtain simple solid solutions such as, body centered cubic (*bcc*) ($Im\bar{3}m$), face centered cubic (*fcc*) ($Fm\bar{3}m$), and hexagonal close packed (*hcp*) ($P6_3/mmc$) instead of intermetallic compounds.

2- The second core effect is the sluggish diffusion of atoms in HEAs that is defined by the large fluctuations in lattice potential energy from the different sizes of atoms creating an important diffusion barrier in the diffusion path.

3- The third core effect is the lattice distortion effect. In fact, HEAs contain at least five elements with different atomic sizes, thus, the lattice is highly distorted as illustrated in figure 1.7. The effect of lattice distortion has demonstrated a positive effect on the properties of HEAs such as, upgrading the mechanical properties by enhancing the strength and hardness [19]…

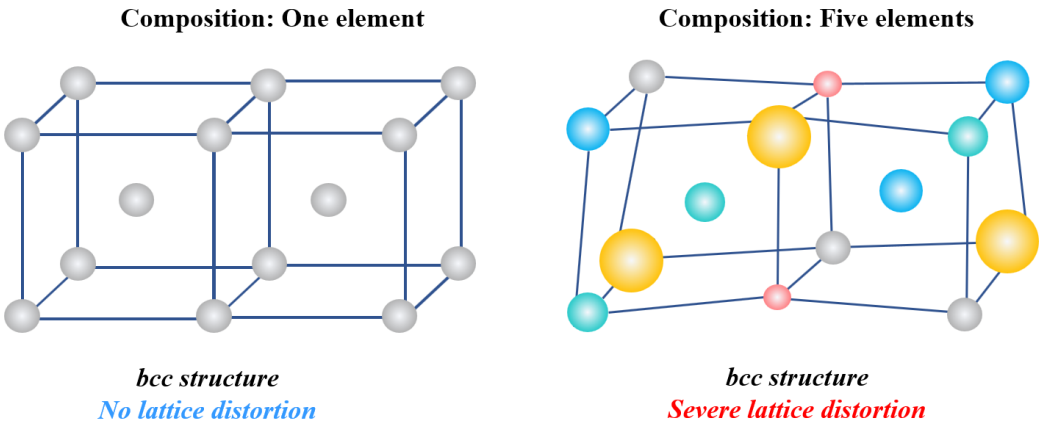

Figure 1.7. Schematic representation of lattice distortion effect in *bcc* structure (inspired by [20]).

4- The fourth core effect is the cocktail one which illustrates that one may obtain exceptional and greater results from of a synergistic mixture.

Additionally, there are many parameters used for HEAs properties predictions such as the electronegativity mismatch ($\Delta\chi$), the mixing enthalpy (ΔH_{mix}), the mixing entropy (ΔS_{mix}), the valence electron concentration (VEC), and the atomic size difference (δ) [21,22]. Among all the latter mentioned parameters we will use the VEC and δ to draw correlations with hydrogen sorption properties in HEAs. Following the rules of Hume-Rothery, one can predict the formation of solid solutions. In fact, alloys containing similar radius sizes atoms are favored to form solid solutions. There are empirical approaches that help predicting the formation of solid solution and the type of crystalline structure in HEAs. The first parameter illustrates the lattice distortion of an alloy by calculating the atomic size difference of its constituent elements (equation 1.2):

$$\delta = \sqrt{\sum_{i=1}^{n} c_i \left(1 - \frac{r_i}{\bar{r}}\right)^2} \qquad \text{Equation 1.2}$$

Where $\bar{r} = \sum_{i=1}^{n} c_i r_i$ and c_i, r_i are the concentration and the atomic radius of the element i and $\bar{r}$ is the average atomic radius of the HEA. Empirical studies stated that complete solid solutions are formed for δ<6.6% and higher distortions will lead to the formation of multiple phases including intermetallic precipitations and even amorphous phases [23] (figure 1.8.a). Hume-Rothery rules of the solid solubility of binary solid solutions can be used as an extension of a high entropy alloy solid solutions that are formed at small δ. Moreover, the valence electron concentration (VEC) could be used to predict the crystalline structure of

HEAs. In fact, *bcc* single phase solid solutions of refractory alloys could exist for VEC<6 whereas for VEC>6, *fcc* single phase solid solutions are formed. However, there's still some multi-phased HEAs that form in both regions (figure 1.8.b) [24].

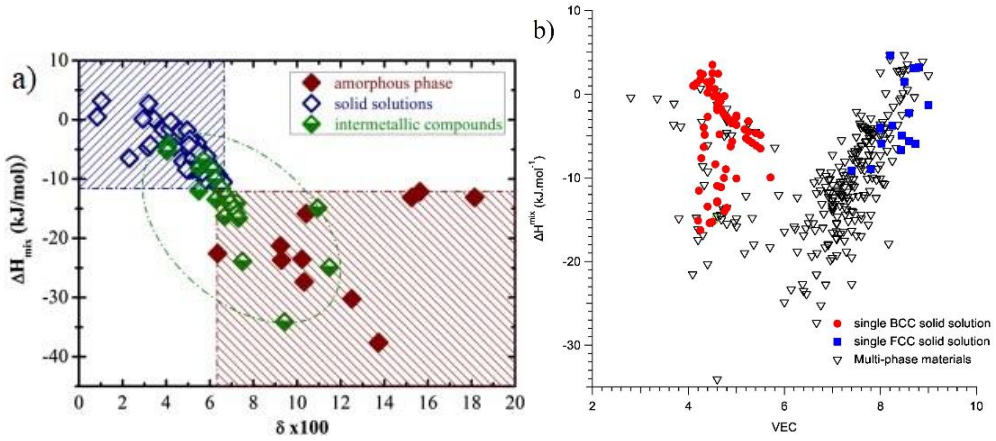

Figure 1.8. (a) Phase selection of HEAs depending on the enthalpy of mixing (ΔH_{mix}) in terms of δ [25], (b) *bcc* and *fcc* crystalline structures regions of formation as predicted by ΔH_{mix} as a function of VEC [24].

1.3.1 Hydrogen sorption in HEAs

Since 2004, HEAs are generally studied for their various and excellent mechanical properties such as, high yield strengths [26], ductility [27], and high hardness values [28] etc. At that time, HEA research was only based on the use of late transition metals. Following these studies, in 2010, Senkov *et al*. used refractory elements into HEAs for the first time [29]. The objective of using refractory based HEAs was to synthesize a material for high temperature applications, thermal, and corrosive protection [30]. Refractory HEAs exhibit various excellent properties that make them suitable for many applications. Interestingly, refractory HEAs when combined with other elements from the *d*-block into a single HEA gives rise to a vast design space for hydrogen storage material candidates.

a) First studies of HEAs for hydrogen storage

One of the first studies for HEAs for hydrogen storage was reported by Kao *et al*. on a series of compositions $Ti_xV_yZr_zMnFeCo$ (where $0.5 \leq x \leq 2.5$, $0.4 \leq y \leq 3.0$, and $0.4 \leq z \leq 3.0$) [31]. The HEAs were adopting a single *C*14 Laves crystal structure. The hydrogen storage capacity varied between 0.03 wt.% and 1.80 wt.% with interesting kinetics of absorption by reaching full hydrogen capacity only after 100 seconds at room temperature [31]. Kunce *et al*. synthesized TiVZrNbMo by Laser Engineered Net Shaping (LENS) [32]. This HEA sample was multi-phased with a *bcc* and orthorhombic phase. Following the

synthesis, at 50°C and under 85 bar of hydrogen, the uptake was 1.79 H/M (2.3 wt.%) and after annealing the hydrogen capacity dropped to 1.45 H/M (1.8 wt.%). The studied HEA contained multiple phases after hydrogenation, hence, there is no clear relationship between the crystal structures and the hydrogen storage properties [32]. Furthermore, by the same method of synthesis (LENS), Kunce *et al*. synthesized ZrTiVCrFeNi and annealed at 1000°C for 24h [33]. The studied HEA is multi-phased with a *C*14 Laves phase and a secondary minor phase of a α-Ti. The maximum hydrogen uptake for the alloy before annealing was 1.81 wt.% and decreases after annealing to reach 1.56 wt.%. In both studied HEAs by Kunce *et al*., it is demonstrated that for HEAs annealing is detrimental to the hydrogen sorption properties by decreasing the hydrogen absorption capacity and the kinetics of hydrogen uptake [32,33]. Moreover, a recent study demonstrated that annealing of HEAs after synthesis can give rise to secondary phases [34].

The mixing of refractory and transition metals is a promising design strategy for finding a suitable HEA candidate for hydrogen storage. Sahlberg *et al*. studied TiVZrNbHf alloy which was synthesized by arc melting [35]. It crystallizes in a single phase *bcc* ($Im\bar{3}m$). At 300°C, the hydrogenation of the studied alloy showed a single step reaction with hydrogen reaching an exceptional hydrogen uptake of 2.5 H/M. In typical *bcc* conventional alloys, this recorded capacity of hydrogen uptake has never been reported. The measured capacity of the studied HEA suggests an occupation of both O and T sites simultaneously which is not common for interstitial hydrides. The distance between both sites (O and T) is usually less than 2 Å, which violates the Switendick criterion for an absorption of 2.5 H/M [36]. However, the metal hydride phase provides an explanation for the high hydrogen uptake. The hydride phase is a body centered tetragonal (*bct*) (I4/mmm) which results in increasing the distance between the interstitial sites. Moreover, it was suggested that the high atomic size difference (δ>6%) of the HEA provided more sites for hydrogen atoms to occupy than conventional alloys. Following this study, Zlotea *et al*. studied the equimolar TiZrNbHfTa alloy. The HEA was synthesized by arc melting and crystallizes in a *bcc* phase. The use of Ta instead of V in the HEA affected the hydrogenation process. In fact, the absorption of hydrogen induced a two-step reaction resulting in a first phase transition at low pressure from an initial *bcc* phase to *bct* monohydride phase and a second phase transition to a *fcc* dihydride phase. This also impacted the hydrogen uptake by decreasing from 2.5 H/M to 2.0 H/M. In this study, it was suggested that the atomic size difference (δ) affected the hydrogen sorption process of HEAs. A HEA with high δ would react with hydrogen in one step (*bcc*→*bct*) with a high hydrogen

absorption capacity, whereas, for low δ, similarly to conventional *bcc* alloys, the hydrogenation reaction will occur *via* two step phase transition (*bcc*→*bct*→*fcc*).

b) The search for correlation with empirical parameters

Instead of varying the concentration of the HEAs constituent elements, Nygård *et al*. studied the effect of addition of different element to a base alloy TiVNb*M* (where M= ∅, Zr, Hf, Ta, Cr, Mo, ZrHf, CrTa and CrMo), TiZrNbHf and TiVCrMo [37]. By arc melting, all the alloys were synthesized and adopt a *bcc* single structure. A correlation is observed between the VEC and the hydride phase, alloys with VEC ≤ 5 will form hydrides that crystallize in a *fcc* structure. Furthermore, most of the alloys absorb hydrogen reaching 2.0 H/M for VEC < 5, whereas for VEC ≥ 5, the absorbed hydrogen capacity starts decreasing drastically. Additionally, the variation of the onset temperature (T_{onset}) of desorption decreases with increasing VEC. Following this work, the same researchers published a similar study with the same empirical approaches. Nygård *et al*. investigated the hydrogen sorption properties of two series of alloys by either varying the ratio of Zr/Ta in the series of alloy $TiVZr_zNbTa_{1-z}$ (where z= 0, 0.15, 0.50, 0.75) or by varying Zr/TiVNb in $TiVZr_{1+z}Nb$ (where z= 0, 0.20, 0.50, 0.75, 1.0) [38]. All the synthesized alloys were prepared by arc melting and adopts a single phase *bcc* structure. All the alloys showed a phase transition from *bcc* to *fcc* during hydrogenation and all the hydrogen capacity uptakes where between 1.8 and 2.0 H/M. No correlation between the atomic size difference (δ) and the hydrogen absorbed capacity (H/M) is observed. However, a linear trend was obtained between the lattice parameter of the *bcc* and *fcc* phases and the ratio of Zr: the more Zr content is increased in the alloy, the higher the lattice parameter will be, because the atomic radius of Zr is higher than the radii of the other constituent elements. The Zr/alloy ratio increases the stability of the hydrides, if Zr/alloy < 12.5 at%, the hydrides will decompose to the initial *bcc*, whereas for Zr/alloy > 12.5 at%, the hydrides will decompose in two *bcc* phases.

In the following years, the research based on empirical parameter criteria focuses on the investigation and prediction of correlations for hydrogen sorption properties. Ek *et al*. reported a systematic investigation to correlate hydrogen sorption properties and various empirical parameters of Ti-V-Zr-Nb-Hf system (ternary, quaternary and quinary alloys) [39]. A total of 21 alloys were synthesized by arc melting, where 17 of them adopted a *bcc* phase structure, whereas TiVZr and TiZrHf formed two *bcc* phase structure and a *hcp* single phase, respectively. The rest of the alloys such as VZrNb, VZrHf, and VZrNbHf were multiphased

containing a main *bcc* phase and a secondary intermetallic phases. The alloys were activated at 340 °C for 2h under dynamic vacuum and cooled down to reach room temperature, most of the alloys absorb hydrogen with slow kinetics (around 6 hours to reach stabilization) reaching a maximum of hydrogen storage capacities between 1.82 and 2.0 H/M. Most of the hydrides adopts *fcc* structure, on the other hand, the TiZrHf, TiVHf, TiZrNbHf, and $TiVZrNb_{0.5}Hf$ alloys form *bct* phases (it is suggested that the formation of the *bct* phase was due to the large amount of Hf and Zr in the alloys). There is no clear correlation between the formed hydride phases, the hydrogen uptake nor the onset temperature with empirical parameters such as δ, and VEC. Nevertheless, a linear trend was drawn between the volumetric expansion per metal $\left\{\left(\frac{V}{z}\right)_{fcc/bct} - \left(\frac{V}{z}\right)_{bcc/hcp}\right\} / \left(\frac{V}{z}\right)_{bcc/hcp}$ with average Pauling electronegativity (χ_p) and VEC. Furthermore, the desorption profiles of the hydrides contained two main events (two peaks), thus, a correlation was observed between the onset temperature (T_{onset}) of the second event and VEC. In fact, the more the VEC is increased, the more the T_{onset} of the second event decreased.

Since HEAs are a mix of many elements, understanding and controlling of their hydrogen sorption properties *via* empirical parameters is challenging. Moreover, the number of possible compositions for HEAs is enormous and one cannot elucidate clear trends for different series of HEAs. The best way for obtaining well-established parameters or data for finding trends, is to limit the variables for a series of alloys and focus on either changing the concentration of elements or by maintaining the stoichiometric composition of the alloy and varying one element.

c) Short review of literature with close compositions to the present work

In literature, there are many reviews of various studies discussing high entropy alloys which have been investigated regarding their hydrogen sorption properties [40–42].

This thesis will focus on HEAs containing four refractory elements Ti, V, Zr, Nb and a fifth one which is a transition metal. Thus, in the following we will review briefly alloys and HEAs with close composition, although, the similarity is broad due to the very large compositional space covered by these previous studies.

Liao *et al*. investigated the hydrogen storage properties of the series of alloys by varying the ratio of the Mn/Mo [43]. The series of alloys, $Ti_{40}V_{30}Cr_{15}Mn_{15-x}Mo_x$ (with x= 0, 2, 4, 6, 8, 10, and 12), was synthesized by arc melting [43]. By increasing the amount of Mo, the

crystalline structure of the alloys changed from crystallizing as a single phase *bcc* structure (alloys where x= 0, 2) to two phase *bcc* structures (alloys with x= 4, 8, 10, 12). The measured PCI showed that all the compositions exhibit two phase transitions during hydrogen absorption. The maximum hydrogen uptake was between 2.29 wt.% and 3.38 wt.% at 30°C. No trend between the hydrogen absorption capacity and the lattice parameter could be drawn. HEAs containing Ti, V, Nb, Zr became widely reported for their hydrogen sorption properties, such as the investigation by Park *et al*. on TiVZrNbCr HEA [44]. The alloy was synthesized by arc melting and adopts a mixture of two *bcc* and *fcc* phases. Moreover, the study of the microstructure of the as cast alloy showed two different phase regions with the following compositions $Ti_{31.1}Zr_{19.6}V_{16.6}Nb_{26.0}Cr_{6.7}$ and $Ti_{9.1}Zr_{20.3}V_{23.4}Nb_{14.1}Cr_{33.1}$. The synthesized alloy could absorb hydrogen without thermal activation. The capacity of the hydrogen absorption was reported to reach 1.77 wt.%. Following the hydrogenation, both initial *bcc* and *fcc* phases transform to two *fcc* with different lattice parameters [44]. A different approach was applied for the design and prediction of the phase formation of HEA by Edalati *et al.* [45]. The approach consisted of using the VEC and thermodynamic calculations which predicted a single phase formation of TiZrCrMnFeNi (with a VEC= 6.4). The HEA was synthesized by arc melting forming a main *C14* Laves phase ($P6_3/mmc$) with a 5% *bcc* phase. At room temperature, the studied HEA had a maximum hydrogen uptake of 1.7 wt.% with fast kinetics [45]. A series of similar composition $Ti_{0.32}Cr_{0.43-x-y}V_{0.25}Fe_xMn_Y$ ($0 \leq x \leq 0.08$, $0 \leq Y \leq 0.08$) was reported by Yoo *et al.* [46]. The series of HEAs was synthesized by arc melting and all the alloys adopt a *bcc* phase. Interestingly, a secondary Laves phase appeared when the Fe concentration increased from 3% to 8%. The hydrogen uptake variation for each composition did not follow any trend, the maximum hydrogen uptake was recorded for $Ti_{0.32}Cr_{0.37}V_{0.25}Fe_{0.03}Mn_{0.03}$ reaching 3.79 wt.% [46]. In this study, the existence of secondary phases had an impact on the assessment of the effect of varying the concentration of elements on the hydrogen sorption properties. Hence, for enhancing the accuracy of the correlation between chemical composition and hydrogen sorption properties, single phase alloys are better suited as they limit the variables which hinders an accurate comparison between alloys.

d) The study of well-defined HEA series: $Ti_{0.30}V_{0.25}Zr_{0.10}Nb_{0.25}M_{0.10}$

Montero *et al*. investigated the phase formation of the quaternary alloy TiVZrNb [47]. The authors optimized the equimolar composition by decreasing the Zr content to ensure the formation of a single-phase structure *via* three different methods of synthesis which are arc

melting (AM), high energy ball milling under argon atmosphere (BM) and reactive ball milling under hydrogen atmosphere (RBM). Following the synthesis by AM, the non-equimolar alloy $Ti_{0.325}V_{0.275}Zr_{0.125}Nb_{0.275}$ (δ = 6.0% and VEC= 4.55) crystallizes in a single-phase *bcc* structure. The same *bcc* structure was also obtained after the synthesis by BM with a slightly larger lattice parameter. The sample prepared by RBM method was a hydride with *fcc* lattice. The samples prepared by AM, BM, and RBM reached a maximum hydrogen absorption capacity of 1.8 H/M, 1.7 H/M, and 1.8 H/M respectively. The measured PCIs of the three samples showed a single plateau at very low pressures. The kinetics of absorption recorded at room temperature for the AM sample were much faster than the BM sample. Both hydride samples of AM and BM showed the same *fcc* phase structure of the RBM sample after hydrogenation. Interestingly, the desorption properties depend on the method of synthesis, the BM, AM, and RBM samples showed 280°C, 220°C, and 180°C as a T_{onset}, respectively. Additionally, the maximum desorption temperature (T_{max}) was 340 °C, 250 °C, and 210 °C for the BM, AM, and RBM samples. Following this study, Montero *et al*. investigated the effect of the addition of 10% of a fifth element to the latter quaternary composition. The series of compositions was $Ti_{0.30}V_{0.25}Zr_{0.10}Nb_{0.25}M_{0.10}$ (*M=Al, Mg, Ta*). The first studied HEA in the series was $Ti_{0.30}V_{0.25}Zr_{0.10}Nb_{0.25}Ta_{0.10}$ which was synthesized by AM [48]. The HEA showed a single step reaction during hydrogenation at room temperature from a *bcc* to an *fcc* phase reaching a maximum hydrogen uptake 2.0 H/M (2.5 wt.%). The addition of 10% of Ta to the quaternary alloy upgraded the desorption properties by decreasing the T_{onset} whilst improving the cycling properties when compared to the parent alloy $Ti_{0.325}V_{0.275}Zr_{0.125}Nb_{0.275}$. The $Ti_{0.30}V_{0.25}Zr_{0.10}Nb_{0.25}Mg_{0.10}$ was synthesized by RBM due to the low melting temperature and the high vapor pressure of Mg. A phase transition occurs during hydrogen absorption from *bcc* to *fcc* hydride phase reaching a capacity of absorption 1.7 H/M (2.7 wt.%) [49]. When compared to the quaternary alloy $Ti_{0.325}V_{0.275}Zr_{0.125}Nb_{0.275}$, the desorption properties of $Ti_{0.30}V_{0.25}Zr_{0.10}Nb_{0.25}Mg_{0.10}$ alloy were not upgraded because both the T_{onset} and T_{max} were increased reaching 250°C and 290°C, respectively. Nevertheless, the cycling properties were upgraded after the addition of 10% of Mg to the parent alloy. The third study was focused on adding 10% of Al, which because of its low mass the gravimetric capacity could be increased relatively to the quaternary alloy. The $Ti_{0.30}V_{0.25}Zr_{0.10}Nb_{0.25}Al_{0.10}$ alloy was synthesized by AM and adopts a single-phase *bcc* structure [50]. During hydrogenation, the alloy experiences a phase transition to a *bct* hydride phase reaching a maximum of absorption capacity of 1.6 H/M (2.6 wt.%). Following the addition of Al, the desorption properties were improved by decreasing the temperature of hydrogen release by

100°C. The 10% addition of Al to the quaternary alloy $Ti_{0.325}V_{0.275}Zr_{0.125}Nb_{0.275}$ affected the hydrogen absorption/desorption cycling performances by reducing the capacity loss and by upgrading the stability of the capacity.

1.4 Scope of the Thesis

Following Montero's results in the series of HEAs $Ti_{0.30}V_{0.25}Zr_{0.10}Nb_{0.25}M_{0.10}$ (*M= Mg, Al, and Ta*), the aim of the present work is to continue with the same strategy of adding 10% of a transition metal element *M* (with *M= Cr, Mn, Fe, Co, Ni, Cu, Zn, and Mo)* to the quaternary alloy $Ti_{0.325}V_{0.275}Zr_{0.125}Nb_{0.275}$. An investigation of the effects of the chemical composition on the hydrogen sorption properties will be conducted and a comparison between the novel alloys and the parent alloy will be drawn. Different methods of synthesis will be employed such as AM, BM, and RBM to synthesize these novel alloys. Moreover, correlations will be established between empirical parameters such as the atomic size mismatch (δ) and the valence electron concentration (VEC), and the hydrogen sorption properties *i.e.*, the maximum capacity of hydrogen uptake, the onset temperature of hydrogen release, lattice parameters (for the as-cast alloys and their hydrides), and the volume expansion following hydrogenation. Furthermore, an in-depth investigation of selected HEAs with the highest capacity of hydrogen absorption will be studied using various characterization techniques regarding the structural transitions upon desorption of hydrogen, hydrogen cycling properties, and the thermodynamics of hydrogenation.

The manuscript will follow the structure below:

Chapter I: Introduction

The first chapter presents the context for current hydrogen storage technologies, followed by a description of solid-state storage materials, a short review of high entropy alloys for hydrogen storage, and finally a presentation of the objectives of this thesis.

Chapter II: Materials and methods

The second chapter contains the description of the various methods and techniques used for the synthesis, characterization of the structure, the microstructure, and the hydrogen sorption properties of the studied HEAs.

Chapter III: Correlation of hydrogen sorption properties with empirical parameters in HEAs

The third chapter will focus on the study and comparison of eleven quinary alloys $Ti_{0.30}V_{0.25}Zr_{0.10}Nb_{0.25}M_{0.10}$ (*M= Mg, Al, Cr, Mn, Fe, Co, Ni, Cu, Zn, Mo, and Ta*) and one quaternary alloy $Ti_{0.325}V_{0.275}Zr_{0.125}Nb_{0.275}$ regarding their structure, microstructure, and hydrogen sorption properties. Consequently, correlations are drawn for the purpose of tracking the effects of varying the chemical composition on the hydrogen sorption properties.

Chapter IV and V: An in-depth study of $Ti_{0.30}V_{0.25}Zr_{0.10}Nb_{0.25}M_{0.10}$ (M= Cr, Mn, and Mo)

The fourth and fifth chapters will be dedicated to thoroughly study three selected HEAs with the highest hydrogen uptake with regards to the phase transitions during the reaction with hydrogen, hydrogenation thermodynamics, and cycling properties.

Chapter VI: Conclusions and perspectives

The final chapter will present the general conclusions of this project by highlighting the most notable results and offer perspectives derived from this work.

References

[1] United Nations Treaty Collection, (n.d.). https://treaties.un.org/pages/ViewDetails.aspx?src=TREATY&mtdsg_no=XXVII-7-d&chapter=27&clang=_en (accessed March 10, 2023).

[2] Energy Density of some Combustibles (in MJ/kg) | The Geography of Transport Systems, (2017). https://transportgeography.org/contents/chapter4/transportation-and-energy/combustibles-energy-content/ (accessed March 13, 2023).

[3] J. Andersson, S. Grönkvist, Large-scale storage of hydrogen, Int. J. Hydrog. Energy. 44 (2019) 11901–11919. https://doi.org/10.1016/j.ijhydene.2019.03.063.

[4] Y. Xia, Z. Yang, Y. Zhu, Porous carbon-based materials for hydrogen storage: advancement and challenges, J. Mater. Chem. A. 1 (2013) 9365–9381. https://doi.org/10.1039/C3TA10583K.

[5] L.J. Murray, M. Dincă, J.R. Long, Hydrogen storage in metal–organic frameworks, Chem. Soc. Rev. 38 (2009) 1294–1314. https://doi.org/10.1039/B802256A.

[6] J. Weitkamp, M. Fritz, S. Ernst, Zeolites as media for hydrogen storage, Int. J. Hydrog. Energy. 20 (1995) 967–970. https://doi.org/10.1016/0360-3199(95)00058-L.

[7] S. Bellini, Y. Sun, F. Gallucci, A. Caravella, Thermodynamic Aspects in Non-Ideal Metal Membranes for Hydrogen Purification, Membranes. 8 (2018) 82. https://doi.org/10.3390/membranes8030082.

[8] J.O. Abe, A.P.I. Popoola, E. Ajenifuja, O.M. Popoola, Hydrogen energy, economy and storage: Review and recommendation, Int. J. Hydrog. Energy. 44 (2019) 15072–15086. https://doi.org/10.1016/j.ijhydene.2019.04.068.

[9] Study of cyclic performance of V-Ti-Cr alloys employed for hydrogen compressor | Elsevier Enhanced Reader, (n.d.). https://doi.org/10.1016/j.ijhydene.2017.12.159.

[10] J.-C. Crivello, B. Dam, R. Denys, M. Dornheim, D. Grant, J. Huot, T. Jensen, P. Jongh, M. Latroche, C. Milanese, D. Milčius, G. Walker, J. Webb, C. Zlotea, V. Yartys, Review of magnesium hydride-based materials: Development and optimisation, Appl. Phys. A. 122 (2016) 122:97. https://doi.org/10.1007/s00339-016-9602-0.

[11] C. Milanese, T.R. Jensen, B.C. Hauback, C. Pistidda, M. Dornheim, H. Yang, L. Lombardo, A. Zuettel, Y. Filinchuk, P. Ngene, P.E. de Jongh, C.E. Buckley, E.M. Dematteis, M. Baricco, Complex hydrides for energy storage, Int. J. Hydrog. Energy. 44 (2019) 7860–7874. https://doi.org/10.1016/j.ijhydene.2018.11.208.

[12] U. Eberle, M. Felderhoff, F. Schüth, Chemical and Physical Solutions for Hydrogen Storage, Angew. Chem. Int. Ed Engl. 48 (2009) 6608–30. https://doi.org/10.1002/anie.200806293.

[13] R. von Helmolt, U. Eberle, Fuel cell vehicles: Status 2007, J. Power Sources. 165 (2007) 833–843. https://doi.org/10.1016/j.jpowsour.2006.12.073.

[14] K.T. Møller, D. Sheppard, D.B. Ravnsbæk, C.E. Buckley, E. Akiba, H.-W. Li, T.R. Jensen, Complex Metal Hydrides for Hydrogen, Thermal and Electrochemical Energy Storage, Energies. 10 (2017) 1645. https://doi.org/10.3390/en10101645.

[15] J.-W. Yeh, S.-K. Chen, S.-J. Lin, J.-Y. Gan, T.-S. Chin, T.-T. Shun, C.-H. Tsau, S.-Y. Chang, Nanostructured High-Entropy Alloys with Multiple Principal Elements: Novel Alloy Design Concepts and Outcomes, Adv. Eng. Mater. 6 (2004) 299–303. https://doi.org/10.1002/adem.200300567.

[16] B. Cantor, I.T.H. Chang, P. Knight, A.J.B. Vincent, Microstructural development in equiatomic multicomponent alloys, Mater. Sci. Eng. A. 375–377 (2004) 213–218. https://doi.org/10.1016/j.msea.2003.10.257.

[17] J.-W. Yeh, Alloy Design Strategies and Future Trends in High-Entropy Alloys, JOM. 65 (2013) 1759–1771. https://doi.org/10.1007/s11837-013-0761-6.

[18] D.B. Miracle, O.N. Senkov, A critical review of high entropy alloys and related concepts, Acta Mater. 122 (2017) 448–511. https://doi.org/10.1016/j.actamat.2016.08.081.
[19] J.-W. Yeh, Physical Metallurgy of High-Entropy Alloys, JOM. 67 (2015) 2254–2261. https://doi.org/10.1007/s11837-015-1583-5.
[20] Q. He, Y. Yang, On Lattice Distortion in High Entropy Alloys, Front. Mater. 5 (2018). https://www.frontiersin.org/articles/10.3389/fmats.2018.00042 (accessed April 25, 2023).
[21] A. Keith, C. Zlotea, P.Á. Szilágyi, Perspective of interstitial hydrides of high-entropy alloys for vehicular hydrogen storage, Int. J. Hydrog. Energy. (2023). https://doi.org/10.1016/j.ijhydene.2023.01.141.
[22] F. Tian, L.K. Varga, N. Chen, J. Shen, L. Vitos, Empirical design of single phase high-entropy alloys with high hardness, Intermetallics. 58 (2015) 1–6. https://doi.org/10.1016/j.intermet.2014.10.010.
[23] X. Yang, Y. Zhang, Prediction of high-entropy stabilized solid-solution in multi-component alloys, Mater. Chem. Phys. 132 (2012) 233–238. https://doi.org/10.1016/j.matchemphys.2011.11.021.
[24] J.P. Couzinié, G. Dirras, L. Perrière, T. Chauveau, E. Leroy, Y. Champion, I. Guillot, Microstructure of a near-equimolar refractory high-entropy alloy, Mater. Lett. 126 (2014) 285–287. https://doi.org/10.1016/j.matlet.2014.04.062.
[25] S. Guo, Q. Hu, C. Ng, C.T. Liu, More than entropy in high-entropy alloys: Forming solid solutions or amorphous phase, Intermetallics. 41 (2013) 96–103. https://doi.org/10.1016/j.intermet.2013.05.002.
[26] O.N. Senkov, C.F. Woodward, Microstructure and properties of a refractory NbCrMo0.5Ta0.5TiZr alloy, Mater. Sci. Eng. A. 529 (2011) 311–320. https://doi.org/10.1016/j.msea.2011.09.033.
[27] A.V. Kuznetsov, D.G. Shaysultanov, N.D. Stepanov, G.A. Salishchev, O.N. Senkov, Tensile properties of an AlCrCuNiFeCo high-entropy alloy in as-cast and wrought conditions, Mater. Sci. Eng. A. 533 (2012) 107–118. https://doi.org/10.1016/j.msea.2011.11.045.
[28] M.-R. Chen, S.-J. Lin, J.-W. Yeh, M.-H. Chuang, S.-K. Chen, Y.-S. Huang, Effect of vanadium addition on the microstructure, hardness, and wear resistance of Al0.5CoCrCuFeNi high-entropy alloy, Metall. Mater. Trans. A. 37 (2006) 1363–1369. https://doi.org/10.1007/s11661-006-0081-3.
[29] O.N. Senkov, G.B. Wilks, D.B. Miracle, C.P. Chuang, P.K. Liaw, Refractory high-entropy alloys, Intermetallics. 18 (2010) 1758–1765. https://doi.org/10.1016/j.intermet.2010.05.014.
[30] O.N. Senkov, D.B. Miracle, K.J. Chaput, J.-P. Couzinie, Development and exploration of refractory high entropy alloys—A review, J. Mater. Res. 33 (2018) 3092–3128. https://doi.org/10.1557/jmr.2018.153.
[31] Y.-F. Kao, P.-H. Lee, J.-H. Sheu, J.-T. Lin, W.-E. Lin, J.-W. Yeh, S.-J. Lin, T.-H. Liou, C.-W. Wang, Hydrogen storage properties of multi-principal-component CoFeMnTi x V y Zr z alloys, Int. J. Hydrog. Energy - INT J Hydrog. ENERG. 35 (2010) 9046–9059. https://doi.org/10.1016/j.ijhydene.2010.06.012.
[32] I. Kunce, M. Polanski, J. Bystrzycki, Microstructure and hydrogen storage properties of a TiZrNbMoV high entropy alloy synthesized using Laser Engineered Net Shaping (LENS), Int. J. Hydrog. Energy. 39 (2014) 9904–9910. https://doi.org/10.1016/j.ijhydene.2014.02.067.

[33] I. Kunce, M. Polanski, J. Bystrzycki, Structure and hydrogen storage properties of a high entropy ZrTiVCrFeNi alloy synthesized using Laser Engineered Net Shaping (LENS), Int. J. Hydrog. Energy. 38 (2013). https://doi.org/10.1016/j.ijhydene.2013.05.071.
[34] M. Moussa, S. Gorsse, J. Huot, J.L. Bobet, Effect of the Synthesis Route on the Microstructure of HfxTi(1−x)NbVZr Refractory High-Entropy Alloys, Metals. 13 (2023) 343. https://doi.org/10.3390/met13020343.
[35] M. Sahlberg, D. Karlsson, C. Zlotea, U. Jansson, Superior hydrogen storage in high entropy alloys, Sci. Rep. 6 (2016) 36770. https://doi.org/10.1038/srep36770.
[36] A.C. Switendick, Band Structure Calculations for Metal Hydrogen Systems*, Z. Für Phys. Chem. 117 (1979) 89–112. https://doi.org/10.1524/zpch.1979.117.117.089.
[37] M.M. Nygård, G. Ek, D. Karlsson, M.H. Sørby, M. Sahlberg, B.C. Hauback, Counting electrons - A new approach to tailor the hydrogen sorption properties of high-entropy alloys, Acta Mater. 175 (2019) 121–129. https://doi.org/10.1016/j.actamat.2019.06.002.
[38] M.M. Nygård, G. Ek, D. Karlsson, M. Sahlberg, M.H. Sørby, B.C. Hauback, Hydrogen storage in high-entropy alloys with varying degree of local lattice strain, Int. J. Hydrog. Energy. 44 (2019) 29140–29149. https://doi.org/10.1016/j.ijhydene.2019.03.223.
[39] G. Ek, M.M. Nygård, A.F. Pavan, J. Montero, P.F. Henry, M.H. Sørby, M. Witman, V. Stavila, C. Zlotea, B.C. Hauback, M. Sahlberg, Elucidating the Effects of the Composition on Hydrogen Sorption in TiVZrNbHf-Based High-Entropy Alloys, Inorg. Chem. 60 (2021) 1124–1132. https://doi.org/10.1021/acs.inorgchem.0c03270.
[40] T.P. Yadav, A. Kumar, S.K. Verma, N.K. Mukhopadhyay, High-Entropy Alloys for Solid Hydrogen Storage: Potentials and Prospects, Trans. Indian Natl. Acad. Eng. 7 (2022) 147–156. https://doi.org/10.1007/s41403-021-00316-w.
[41] L. Kong, B. Cheng, D. Wan, Y. Xue, A review on BCC-structured high-entropy alloys for hydrogen storage, Front. Mater. 10 (2023). https://www.frontiersin.org/articles/10.3389/fmats.2023.1135864 (accessed April 17, 2023).
[42] F. Marques, M. Balcerzak, F. Winkelmann, G. Zepon, M. Felderhoff, Review and outlook on high-entropy alloys for hydrogen storage, Energy Environ. Sci. 14 (2021) 5191–5227. https://doi.org/10.1039/D1EE01543E.
[43] X. Liao, Z. Yin, K. Young, J. Nei, Studies in molybdenum/manganese content in the dual body-centered-cubic phases metal hydride alloys, Int. J. Hydrog. Energy. 41 (2016) 15277–15286. https://doi.org/10.1016/j.ijhydene.2016.06.189.
[44] K.B. Park, J.-Y. Park, Y.D. Kim, J.-I. Choi, H.-T. Im, J.-W. Kang, H.-S. Kang, T.-W. Na, H.-K. Park, Study on hydrogen absorption and surface properties of TiZrVNbCr high entropy alloy, Intermetallics. 130 (2021) 107074. https://doi.org/10.1016/j.intermet.2020.107074.
[45] P. Edalati, R. Floriano, A. Mohammadi, Y. Li, G. Zepon, H.-W. Li, K. Edalati, Reversible room temperature hydrogen storage in high-entropy alloy TiZrCrMnFeNi, Scr. Mater. 178 (2020) 387–390. https://doi.org/10.1016/j.scriptamat.2019.12.009.
[46] J.-H. Yoo, G. Shim, C.-N. Park, W.-B. Kim, S.-W. Cho, Influence of Mn or Mn plus Fe on the hydrogen storage properties of the Ti-Cr-V alloy, Int. J. Hydrog. Energy. 34 (2009) 9116–9121. https://doi.org/10.1016/j.ijhydene.2009.08.064.
[47] J. Montero, C. Zlotea, G. Ek, J.-C. Crivello, L. Laversenne, M. Sahlberg, TiVZrNb Multi-Principal-Element Alloy: Synthesis Optimization, Structural, and Hydrogen Sorption Properties, Molecules. 24 (2019) 2799. https://doi.org/10.3390/molecules24152799.
[48] J. Montero, G. Ek, L. Laversenne, V. Nassif, G. Zepon, M. Sahlberg, C. Zlotea, Hydrogen storage properties of the refractory Ti–V–Zr–Nb–Ta multi-principal element

alloy, J. Alloys Compd. 835 (2020) 155376. https://doi.org/10.1016/j.jallcom.2020.155376.
[49] J. Montero, G. Ek, M. Sahlberg, C. Zlotea, Improving the hydrogen cycling properties by Mg addition in Ti-V-Zr-Nb refractory high entropy alloy, Scr. Mater. 194 (2021) 113699. https://doi.org/10.1016/j.scriptamat.2020.113699.
[50] J. Montero, G. Ek, L. Laversenne, V. Nassif, M. Sahlberg, C. Zlotea, How 10 at% Al Addition in the Ti-V-Zr-Nb High-Entropy Alloy Changes Hydrogen Sorption Properties, Mol. Basel Switz. 26 (2021). https://doi.org/10.3390/molecules26092470.

CHAPTER II
Materials & Methods

Chapter 2. Materials and Methods

The aim of this thesis is to study the hydrogen sorption properties of body centered cubic (*bcc*) ($Im\bar{3}m$) HEAs. The series of compositions is $Ti_{0.30}V_{0.25}Zr_{0.10}Nb_{0.25}M_{0.10}$ with *M* = Cr, Mn, Fe, Co, Ni, Cu, Zn, and Mo. In addition, results from previously studied compositions with *M* = Mg, Al, and Ta will be analyzed. Therefore, this chapter will cover the experimental techniques used for the synthesis and characterization of the alloys. Different methods that were applied to characterize the structural and microstructural properties of the as-cast alloys and their corresponding hydrides will be presented as well as their solid-gas interactions.

2.1 Synthesis

The studied HEAs in this thesis are prepared by diverse methods to successfully obtain *bcc* phased alloys. Table 2.1 presents the various forms of metals from bulk pieces to pure elemental powders.

Element	Form	Size	Purity (%)	Manufacturer
Ti	Pellets	6x6 mm	99.99	Neyco
Ti	Powder	<100 µm	99.9	Alfa Aesar
V	Pellets	6x6 mm	99.9	Neyco
V	Granules	1-3 mm	99.7	Alfa Aesar
Cr	Irregular Chips	1-25 mm	99.99	Alfa Aesar
Mn	Irregular chips	3-12 mm	99.99	Chempur
Fe	Powder	<10 µm	99.5	Alfa Aesar
Co	Powder	<40 µm	99.8	Strem Chem
Ni	Powder	<150 µm	99.99	Alfa Aesar
Cu	Powder	<45 µm	90	Alfa Aesar
Zn	Powder	<150 µm	99.9	Alfa Aesar
Zr	Lopins	3x3 mm	99.95	Neyco
Zr	Powder	<150 µm	99.95	Strem Chem
Nb	Slug	⌀ 6.35x12.7 mm	99.95	Alfa Aesar
Nb	Powder	<250 µm	99.8	Alfa Aesar
Mo	Rod	⌀3x500 mm	99.9	Chempur

Table 2.1. Table of the used pure metals with their corresponding from, size purity and manufacturer.

2.1.1 Arc melting

- **Principle of synthesis**

The most used technique for synthesizing elements with high melting temperatures such as refractory elements is arc melting (HT-AM). In arc melting, a DC voltage is applied to create an electric discharge to melt elements under inert atmosphere usually Argon (Ar). The electric arc is created between a tungsten electrode and a water cooled cooper crucible. The created electric arc will ionize the Ar atmosphere creating a plasma (figure 2.1). The HT-AM can reach a temperature of 3000 °C and can be controlled by adjusting the electric power that is generated from a generator. Prior to melting, the chamber is put under secondary vacuum then filled with 400 mbar of Ar gas to eliminate any O_2 contamination. The synthesized HEAs were cooled down between each melt by water cooled cooper crucible.

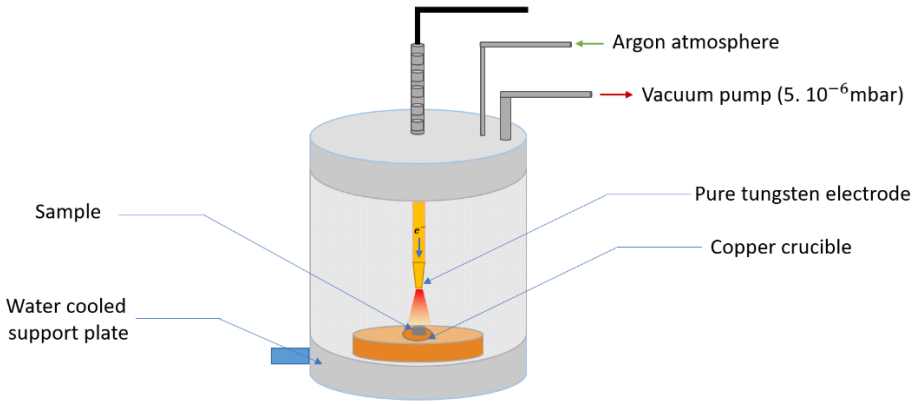

Figure 2.1. Schematic representation of the arc melting.

- **Protocol of synthesis**

The pure metals were cut and weighed to obtain the desired stoichiometry for a total mass sample of 3 g and placed inside the copper crucible. A secondary vacuum was applied on the chamber containing the elements reaching 5.10^{-6} mbar. Following this, the chamber was filled with Ar gas. Each HEA was melted *via* different current (80-90 A) depending on the elements of the composition and different number of remelts were applied to obtain the desired alloy (10-25 remelts). After each melt, the ingot is turned and remelted again to ensure the homogeneity of the sample.

Following the synthesis by HT-AM, not all samples were single phased *bcc*. Therefore, we switched to high energy ball milling under Ar or H_2 atmosphere. Both methods of synthesis will be described in the next section.

2.1.2 High energy ball milling under argon

The planetary ball milling (BM) is used in this project as an alternative to synthesize HEAs to obtain the desired *bcc* phase. The reason of the word planetary is to describe the movement like planet that the vials have during the milling. The vials are connected to a rotating support disk and rotate around their own axes. Both types of rotation affect the contents of the vials and produce a centrifugal force. The vials contain grinding balls, sample in the form of powder under Ar gas. By the kinetic energy that is produced from the collision of the grinding balls, the alloying process is achieved. Moreover, the centrifugal force produced by the vials rotation causes the collision of the grinding balls between each other and friction with the inside wall, resulting of the alloying of all the material (figure 2.2).

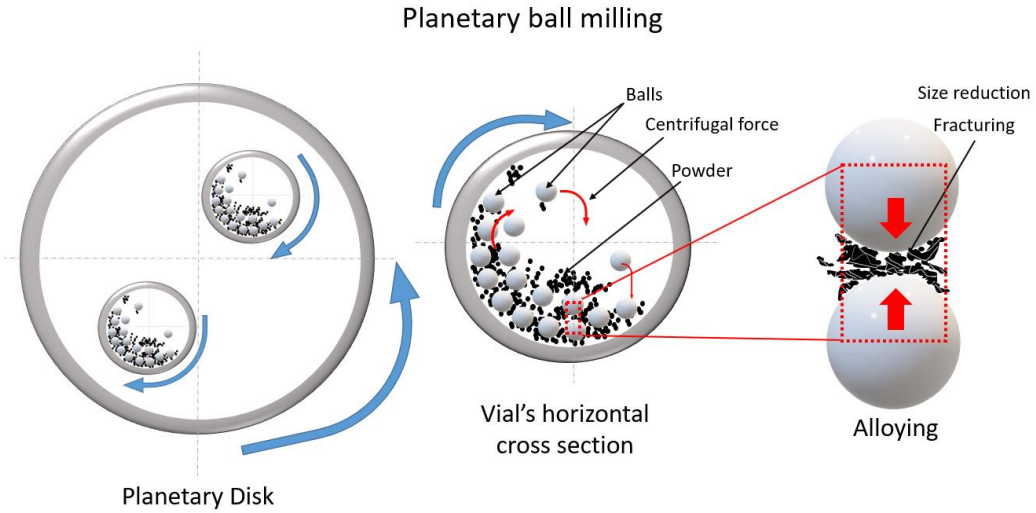

Figure 2.2. Schematic representation of the high energy ball milling under argon atmosphere.

There are various controlled parameters in order to obtain the desired phase such as the ball to material weight ratio that is equal to 26:1 (material mass is 5 g), the size of the grinding balls (7 mm), the rotation speed is 700 rotation per minute (rpm) and the timing of the mill is between 45-60 min. The milling was made by 4-5 cycles of 15 min to ensure the cooling of the system (sample, balls) between sequences.

The weighing of the elements in the form of powder was done inside the glove box to avoid any contaminations. Following this, the vial containing the elements and the grinding balls are sealed by a Viton gasket and placed in the milling machine (type Fritsch instruments, Pulverisette) outside of the glove box.

2.1.3 High energy reactive ball milling

The reactive ball milling (RBM) is similar to ball milling under argon except the milling is done under H_2 atmosphere resulting in direct synthesis of a hydride material [1]. Prior to the milling, 5 g of the elements in the form of powder were introduced in the vial with grinding balls of 12 mm of diameter for a ball to powder ratio 60:1. All the preparation is done inside the glove box, then the vial is taken out and connected to a manometric device to replace the Ar gas with 70 bar of H_2. The vial is fixed in the milling machine type Pulverisette 4. RBM is an interesting method because it enables an *in situ* monitoring of temperature and pressure during the milling. A sensor in the vial is providing data (pressure/temperature) to a radio emitter. Subsequently, the data is digitally transmitted to an external receiver (from Evicomagnetics) that is connected to a computer to collect and plot all data. With the same planetary principle, two different rotations are applied, one for the vial and the other on the planetary desk resulting in an overall rotation speed of 800 rpm (figure 2.3). Contrary to BM under Ar, RBM synthesis is carried out continuously for 120 min without any breaks.

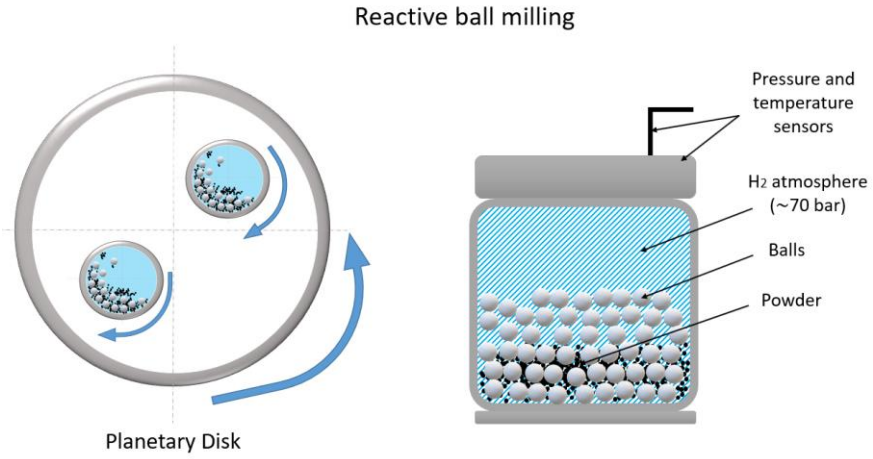

Figure 2.3. Schematic representation of high energy ball milling under hydrogen.

The structure and microstructure of the synthesized materials were characterized by different methods and techniques that will be presented in the next section.

2.2 Structural and microstructural characterizations

The structure of the materials such as as-cast, hydrides and deuterides were characterized *via* different techniques and methods such as, X-ray diffraction, neutron diffraction, and total X-ray scattering for pair distribution function analysis. Whereas for the microstructure, the samples were characterized by Scanning electron microscope (SEM) and energy dispersive

spectroscopy (EDS). All the mentioned techniques and methods will be presented in the following sections.

2.2.1 X-ray diffraction

A common and powerful tool to study the structure of crystalline materials is X-ray diffraction (XRD). The technique is based on the interaction between radiation and matter and allows the identification of the crystalline structure of the samples. The wavelength (λ) of X-ray waves and the distance between plans of atoms (d_{hkl}) of the crystalline structure of the characterized material are similar resulting in a coherent scattering. If there is a long range order, the interaction of the scattered waves with the material will result in the emergence of a diffraction pattern. An incident monochromatic beam with a wave vector k is diffracted after interacting with the atoms of a certain planes (hkl) and the new wave vector of the diffracted beam will be k'. The angle between the incident and the diffracted wave is known as Bragg angle 2θ as illustrated in figure 2.4. A relationship was established by Bragg relating the diffraction order (n), the wavelength (λ), the diffraction angle (θ), and the interatomic distance (d_{hkl}):

$$n\lambda = 2\, d_{hkl} \sin\theta \qquad \text{Equation 2.1}$$

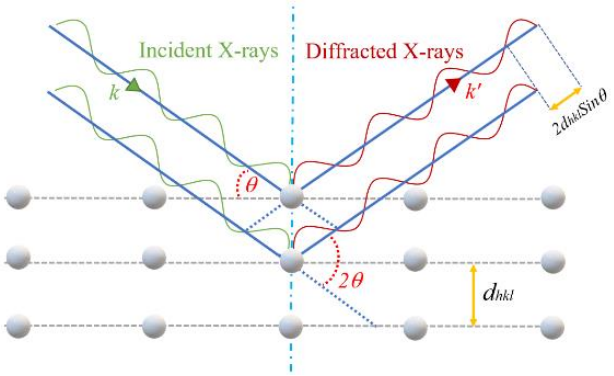

Figure 2.4. Schematic representation X-ray diffraction.

Depending on the type of the diffractometer, the collection of the diffraction signals was based on different geometries: for the lab X-ray diffractometer, the used geometry was the Bragg-Brentano, whereas for synchrotron X-ray diffraction and neutron diffraction the geometry was Debye-Scherrer.

In this thesis, X-ray powder diffraction was carried out by both laboratory and synchrotron sources as described in the following sections.

2.2.1.1 Laboratory X-ray diffraction

The diffractometer Bruker D8 advance was used for the structural characterization of as-cast HEAs and their hydrides. The scan was done in the 2θ range 20-90° and the source of X-rays is a copper anticathode ($K_{\alpha 1}$, λ_1=1.5406 Å; $K_{\alpha 2}$, λ_2=1.5443 Å).

2.2.1.2 Synchrotron radiation X-ray diffraction

A powerful source compared to the laboratory X-ray is the synchrotron (SR) source. In SR, the principle of the production of X-rays is based on accelerating electrons by an accelerator reaching high velocities. At a certain level of velocity, the electrons are then introduced into a large ring. Electrons are guided *via* bending magnets to circulate in the ring. The change of the direction of electrons will result in the production of light that is in the X-ray energy range. Finally, the produced radiation is guided to a beamline that is an experimental end station[2].

Using synchrotron radiation has many advantages. In fact, high energy X-rays are used to characterize materials with very fast data collection to follow *in situ* structural changes during reactions for example hydrogen absorption/desorption of HEAs.

In this thesis, SR-XRD measurements were carried out at the Cristal beamline in SOLEIL facility. *Ex situ* structural characterization was done with different wavelengths (λ=0.7289 Å, λ=0.72907 Å) and the samples were charged in a capillary tube of 0.2 mm diameter. The scanning range was from 1° to 85° (2θ) within a 10 minute acquisition time.

In situ SR-XRD during hydrogen desorption of the hydride samples were carried out with a wavelength of λ=0.67156 Å. The scanning range was from 0.2° to 65°(2θ) within a 3 minute acquisition. The samples were finely grounded, mixed with fumed silica powder to reduce the X-ray absorbance and loaded in a capillary tube of 0.2 mm diameter. The SR-XRD data was recorded during the hydrogen desorption by applying a constant temperature ramp from 25 to 450 °C with a rate of 2°C/min under secondary vacuum. For the *in situ* measurement the capillary were fixed in a sample holder designed for the experiment and was connected to a vacuum pump. The capillary was heated by a hot air blower that was close enough for the heat transfer to the sample as illustrated in figure 2.5.

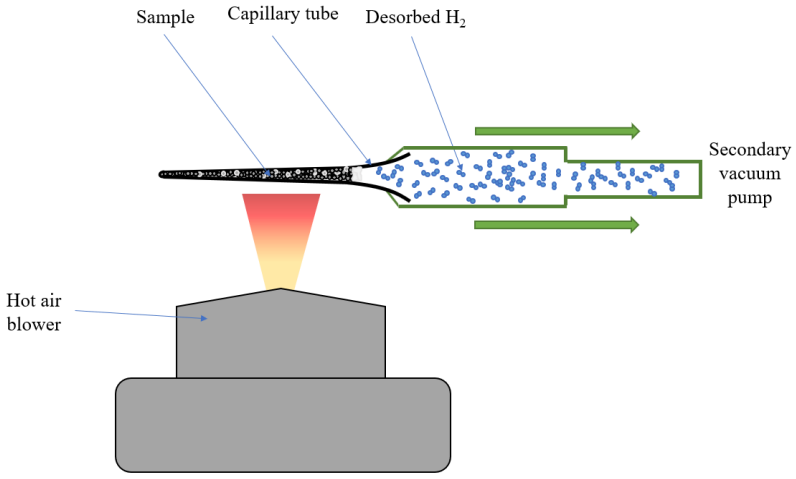

Figure 2.5. Schematic representation X-ray diffraction.

2.2.2 Neutron powder diffraction

Neutron powder diffraction is used in this work to determine the hydrogen (deuterium) desorption properties and the interstitial position of hydrogen/deuterium in the hydride phase. The scattering of X-rays with elements is on the level of the electron cloud and as a result, light weight elements such as, hydrogen have a very weak interaction with X-rays. Contrary to X-rays, neutrons are a non-charged type particle that interacts with the nuclei of atoms and have a more important interaction with hydrogen (deuterium). The scattering power of neutrons with elements is random and no trend can be established with elements of the periodic table, as illustrated in figure 2.6.

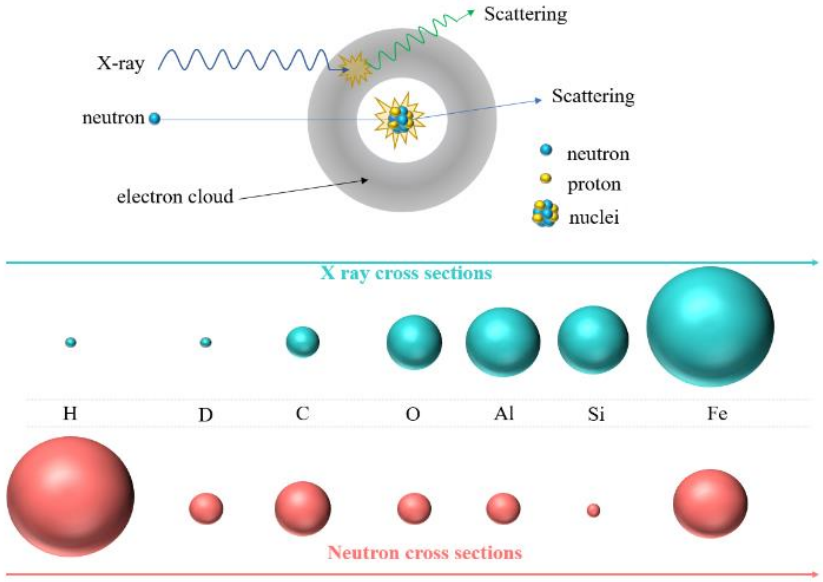

Figure 2.6. Schematic representation of X-ray and neutron scattering (top). Comparison between the scattering cross sections of elements with X-rays and neutrons (bottom).

The hydrogen isotope deuterium is highly visible to neutrons and usually replaces the hydrogen to have a better neutron diffraction resolution. Therefore, deuterium was used instead of hydrogen for neutron diffraction experiments. The neutron diffraction allowed us to determine and locate the position of the deuterium in the crystalline lattice of the deuterated samples.

In situ and *ex situ* powder neutron diffraction experiments were carried out on the D1B beamline at Institute Laue-Langevin (λ=1.2858 Å) (DOI:10.5291/ILL.DATA.CRG-2768). The *ex situ* characterizations of the deuterated samples were performed at room temperature using a vanadium container (30 min time of acquisition) while the *in situ* deuterium desorption experiments were performed on a silica tube loaded with deuterated samples. The silica tube was connected to a secondary vacuum and placed inside a furnace to be heated with a constant

heating rate of 1°C/min while the evolved gas pressure was simultaneously recorded by a vacuum gauge. The scanning range was from 1° to 128° (2θ).

2.2.3 Structural refinement

The X-ray and neutron diffraction data were refined by the Rietveld method. Important structural properties can be obtained from the diffraction peaks position, intensity, and shape. The principle of the Rietveld method is to use experimental diffraction data and create a model, starting from a primary given crystal structure. During the iterative calculation, two types of parameters are refined: structural and instrumental parameters. The refinement uses a least-squares minimization technique (equation 2.2)[3].

$$\Phi=\sum_{i=1}^{n} w_i \, (y_i^{obs} - y_i^{calc})^2 \qquad \text{Equation 2.2}$$

-n : data points of the experimental diffraction pattern

-y_i^{obs}, y_i^{calc}: the observed and calculated intensity

-w_i: the weight assigned at (i) data points π

The diffraction peak intensity is a parameter that can be refined which is proportional to the square of the structure factor F_{hkl} that is described in equation 2.3:

$$F_{hkl}=\sum_{n=1}^{N} f_n e^{2\pi i.(hx_n+ky_n+lz_n)} \qquad \text{Equation 2.3}$$

-f_n: the atomic scattering factor

-$2\pi i.(hx_n + ky_n + lz_n)$: the phase angle of atom *n*

- $x_n + y_n + z_n$: coordinates of atom *n* in the cell

As already explained, X-rays scatter off the electrons (electron cloud) so the parameter f_n is proportional to the atomic number.

The intensity of a reflection I_{hkl} is described by equation 2.4:

$$I_{hkl} = S.M_{hkl}.L_{hkl}.P_{hkl}.|F_{hkl}|^2 \qquad \text{Equation 2.4}$$

-S: the scale factor

-M_{hkl}: the multiplicity of the reflections

-L_{hkl}: the Lorentz-polarization

-P_{hkl}: the preferred crystallographic orientation

-F_{hkl}: the structure factor

Instrumental and experimental parameters that affects the shape, the width and the position of the diffraction peaks were also refined.

The used model for fitting the experimental diffraction profile is the Thompson-Cox-Hasting pseudo-Voigt [4]. All the refinements were carried out by Fullprof Suite[5], this is a software that implements the Rietveld method. The refined parameters were scale factor, the

isotropic displacement parameter, zero offset, lattice parameters, shape parameters: full width at half the maximum (U, V, W, and X), and the phase fractions in the case of a coexistence of multiple phases. The quality of agreement between calculated and experimental profiles is measured and evaluated by a set of agreement factors such as the weight profile residual R_{wp} (equation 2.6), expected profile residual R_{exp} (equation 2.7), and the goodness of the fit χ^2 (equation 2.8):

$$R_{wp}=\left[\frac{\sum_{i=1}^{n} w_i\left(Y_i^{obs}-Y_i^{calc}\right)^2}{\sum_{i=1}^{2} w_i\left(Y_i^{obs}\right)^2}\right]^{1/2} \times 100\% \qquad \text{Equation 2.6}$$

$$R_{eop}=\left[\frac{n-P}{\sum_{i=1}^{2} w_i\left(Y_i^{obs}\right)^2}\right]^{1/2} \times 100\% \qquad \text{Equation 2.7}$$

$$\chi^2=\frac{\sum_{i=1}^{n} w_i\left(Y_i^{obs}-Y_i^{calc}\right)^2}{n-P}=\left(\frac{R_{wp}}{R_{exp}}\right)^2 \qquad \text{Equation 2.8}$$

- n: the total number of measured points

-Y_i^{obs}, Y_i^{calc}: the observed and calculated intensity

-P: number of free least-squared parameters

The values of the agreement factors may differ depending on the techniques/instruments used such as lab XRD, SR-XRD and neutrons, since some of the previously mentioned factors are affected by the ratio of the signal to background. Nevertheless, χ^2 can give a good assessment of the quality of the Rietveld refinement.

2.2.4 Total scattering: Pair distribution function

The pair distribution function (PDF) is a method that is similar to the conventional powder diffraction. The advantage of this technique is the ability to acquire a quantitave insight of the structure of materials. The high energy X-rays are scattered off the material and detected, similar to previously explained XRD technique. However, the used X-ray wavelengths are extremely short, and the angular range is wide. Therefore, the probed reciprocal space is very wide. Materials always display some disorder, for example, thermal vibrations, vacancies, dislocations, and this gives rise to the diffuse scattering. Generally, diffuse scattering is difficult to quantify. If there are defects in the lattice of the material, in the Bragg diffraction experiment the amplitude of the Bragg peaks will only decrease and the diffuse scattering will not be taken to consideration. The lost information is then considered as a part of the diffuse scattering. For all the mentioned reasons, total scattering refers to the consideration of both Bragg scattering and diffuse scattering. PDF is a technique that is based on total scattering and it allows the determination of the local order [6].

The analysis of total scattering experimental data is different from the conventional diffraction that is conducted in reciprocal space, instead it is in real space with PDF function G(r) which is the Fourier transform (F(Q)) (equation 2.9) of the total scattering structure function (equation 2.10).

$$F(Q)=Q[S(Q)-1] \qquad \text{Equation 2.9}$$

$$G(r) = \frac{2}{\pi}\int_{Q_{min}}^{Q_{max}} F(Q)\sin(Qr)\,dQ \qquad \text{Equation 2.10}$$

S(Q) is the structure function that is obtained from the Bragg and diffuse components of the X-ray powder diffraction intensity. The magnitude of the scattering momentum is represented by Q ($Q = 4\pi \sin\theta/\lambda$) and Q_{max}, Q_{min} are experimental set up values that are adjusted to the measurement, for example, the ratio of the signal/noise becomes very important at high Q region, so the Q_{max} will be decreased to avoid the emergence of noisy data.

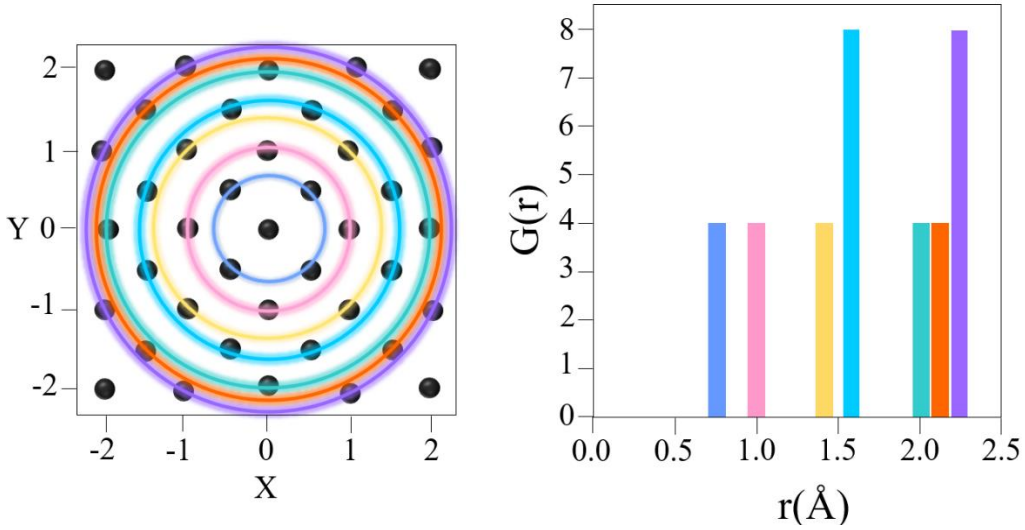

Figure 2.7. Schematic representation of the pair distribution function G(r).

As illustrated in figure 2.7, PDF corresponds to a histogram in terms of interatomic distances. A random atom is chosen to be a center from which all the distances (represented by coordination rings) from the other atoms are measured. All the interatomic distances are extracted and projected over the radius (r). The intensity correlates to the density of atoms at a certain distance (r).

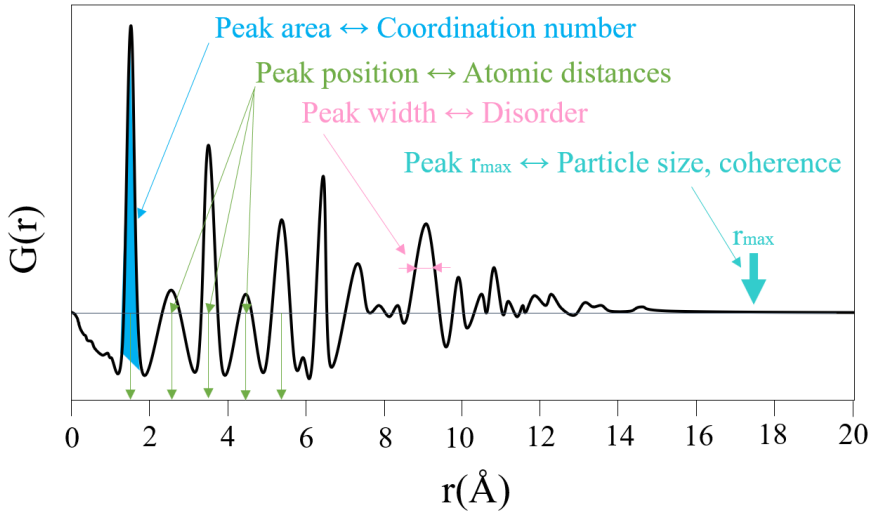

Figure 2.8. High-energy X-ray total scattering derived from PDF providing real space structure information.

A typical PDF pattern is shown in figure 2.8. Information about the real space structure is obtained directly from the plot. The area of peaks represents the existence of pairs depending on their scattering power. The peak position indicates the interatomic distances. The peak width is linked to the disorder of the lattice that can be either a structural disorder or atomic thermal vibration or both. The last measured peak at high (r) gives information about the particle size and the limit of the size of the coherence domain [7].

PDFGui [8] was used as a software for the refinement of the obtained experimental data. The technique consists in a least squares refinement profile similar to the Rietveld refinement but in real space. Several parameters were refined such as: the lattice parameters (a, b, and c) of the hydride phase, the Isotropic thermal displacement of atoms (U_{iso}), delta2 which refers to the coefficient for ($1/r^2$) contribution to the peak sharpening and the PDF peak broadening Q_{broad}.

The experimental data were obtained by high-energy synchrotron XRD measurements on hydride samples using ID15A beamline at ESRF, Grenoble (France). The incident flux was normalized by placing a diode in front of the sample. The diffraction patterns were collected in transmission geometry by using a Pilatus3 X CdTe 2M hybrid photon counting detector. In order to minimize inhomogeneity effects and cover dead zones, a number of diffraction patterns were collected at a slightly different detector positions. With respect to the 99 KeV incident, the detector was off-centered and positioned close to the sample for accessing Q values up to approximately 30-35 $Å^{-1}$. A correction of the images was done for detector geometry, response, distortion, transparency and for the background contributions and X-ray polarization. Data were azimuthally integrated using a modified version [9] of the PyFAI library [10] to give one

dimensional scattering patterns. The G(r) were calculated from these patterns using routines from the Diffpy-CMI library [11] with local modifications for outlier rejection and treatment of background.

2.2.5 Microstructure characterization

2.2.5.1 Scanning electron microscopy

Following the synthesis of as-cast materials, it is important to characterize the homogeneity of the synthesized samples. Moreover, the hydrogen cycling could have an effect on HEAs microstructure by embrittlement or modification of the microstructure. The as-cast/cycled samples microstructure, chemical composition and morphology were analyzed and characterized by a scanning electron microscopy (SEM) and energy dispersive spectroscopy (EDS).

The SEM is a type of electron microscope that is used for studying the surfaces of bulk or powder materials. Figure 2.9 illustrates the main components of SEM, at the top, a beam of electrons is produced by an electron gun. The range of the generated beam is controlled between 1-40 KeV. The beam is then guided vertically through electromagnetic fields and lenses to interact with the sample.

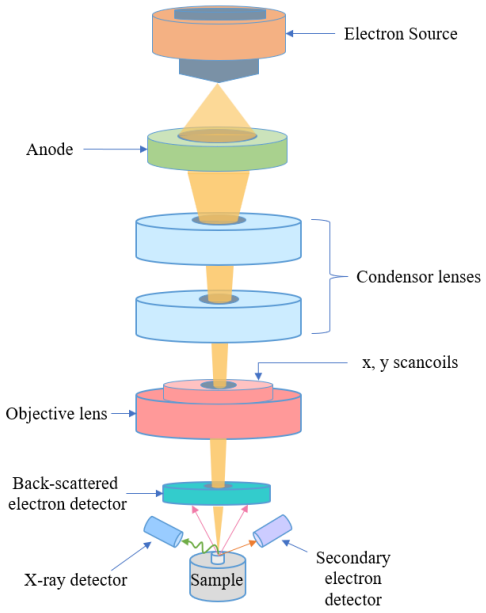

Figure 2.9. Diagram of the working principle and components of SEM.

Electrons interact with the sample producing secondary electrons, backscattered electrons, and characteristic X-rays. As illustrated in figure 2.9, these signals are collected by different detectors. The electron beam hits the surface and penetrates the sample (depending on the used energy and the density of the sample) to a depth of few nanometers. The electron beam-sample interaction takes place in a pear shape as illustrated in figure 2.10.

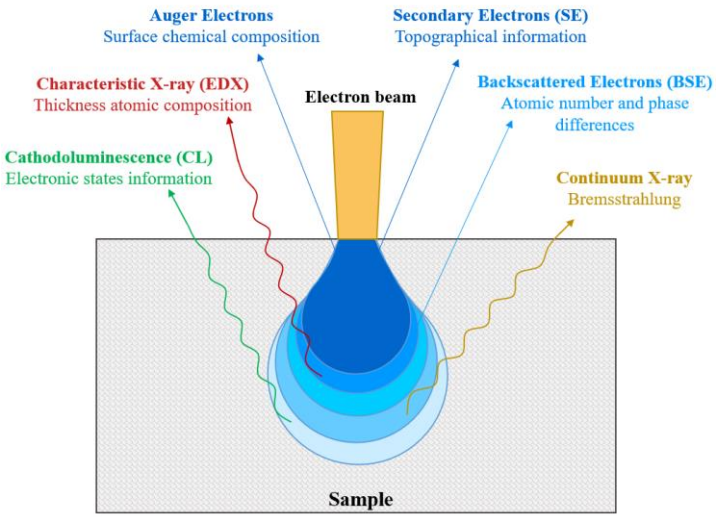

Figure 2.10. Diagram of the working principle and components of SEM.

Secondary electrons (SE) have low energy and come from the interaction of the primary electrons with the atoms of the sample. The primary electrons will interact with the constituent atoms of the sample resulting in an ionization of its electrons (inelastic interaction). The SE have low energy and can easily be absorbed, therefore they are only used for topographic and morphologic information of the surface. Contrary to SE, back-scattered electrons (BSE) are reflected back due to an elastic scattering interaction between the previously mentioned primary electrons and the atoms of the sample. The source of BSE comes from deeper regions when compared to SE. The number of BSE is proportional to the atomic number and regions containing high atomic numbers (heavy elements) will appear bright. Therefore, these types of electrons are useful for displaying the different phases/compositions existing in the sample.

2.2.5.2 Energy dispersive spectroscopy

Energy Dispersive spectroscopy (EDS) is used to determine the chemical composition of the samples. The density of atoms is measured along with their distribution in the sample resulting in a mapping image. The process of differentiating between the different atoms of the sample is based on the collision of beams electrons (incident electrons) with electrons of the atoms sample. This collision will result in the excitation of a core-electron (located at low energy levels) leaving a vacancy. This vacancy will be filled with an electron located at higher energy levels emitting energy, precisely X-rays. The transition that occurs differ depending on the nature of the atom and the energy of these X-rays is characteristic of the element. Hence, the emitted X-rays will provide information on the nature and density of the constituent atoms of the analyzed sample.

SEM and EDS measurements were carried out by a Zeiss Merlin microscope, using 15 Kev of beam energy. Prior to the measurements, the as-cast and cycled samples were embedded in an epoxy resin, then polished and coated with 1.9 nm of Pd.

The main aim of the project is to study the hydrogen sorption properties of HEAs, the instruments and the different methods used to characterize these properties are covered in the next section.

2.3 Hydrogen sorption characterizations

A direct solid-gas reaction between metals and hydrogen results in the formation of metal hydrides. The hydrogenation reaction is exothermic and spontaneous. However, some samples need to be activated *via* different methods such as heat treatment under dynamic vacuum or hydrogenation at very high pressures. The reason for activation is to reduce the layer of oxides on the surface resulting in creating fresh surfaces. The studied AM/BM materials (mass: 300-400 mg) were loaded in a stainless steel cell and activated *via* a heat treatment of 350 °C for 3 hours under dynamic vacuum (3.10^{-3} mbar). The hydrogenation of the sample was carried out using a homemade volumetric device with thermostatically calibrated volumes at 25 °C based on the Sievert method [12], as illustrated in figure 2.11.

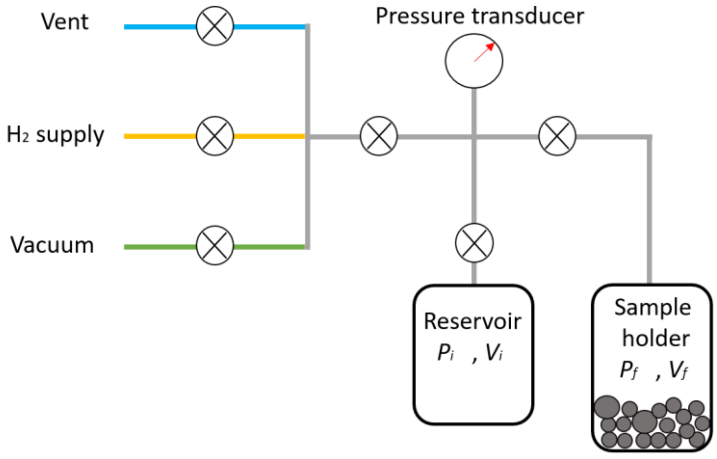

Figure 2.11. Schematic illustration of a Sievert type apparatus for manometric sorption measurements.

The hydrogenation of the sample is done following these steps: all the system is evacuated and then the isolation valve between the sample holder and the rest of the apparatus is closed leaving the sample holder under static vacuum. A precise amount of hydrogen pressure is introduced in the reservoir (P_i, V_i). The opening of the isolation valve results in the decrease of the initial pressure due to volume expansion of the gas. The change of the pressure can be evaluated and confirmed by Boyle's Law (equation 2.11).

$$P_i V_i = P_f V_f \qquad \text{Equation 2.11}$$

In some cases, there could be a period with no absorption after exposure of the sample to a hydrogen atmosphere, this period is known as the incubation time. Following the incubation time, the sample will absorb hydrogen and the pressure decreases until stabilizing at an equilibrium pressure (P_{eq}) (figure 2.12).

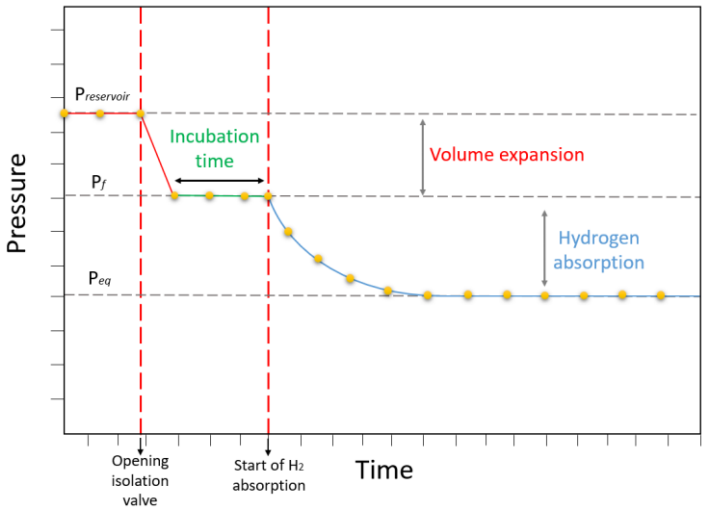

Figure 2.12. Pressure measurement in a Sievert device during hydrogen absorption.

A relation between the pressure variation and the absorbed amount of hydrogen by the sample is established using the real gas equation (equation 2.12).

$$\Delta PV = \Delta nRT \qquad \text{Equation 2.12}$$

Under isothermal and isochoric conditions, equation 2.12 can be applied. Where ΔP is the pressure variation, V is the volume of the system (reservoir and sample holder) and Δn is the number of moles absorbed by the sample. However, for this type of experiment the compressibility factor indicates that the ideal gas formula cannot be applied. Therefore, the real gas equation is used [12]. The experimental data base of real gases is provided from the National Institute of Standards and Technology (NIST) and is used to determine the hydrogen density depending on temperature and pressure.

The calculated hydrogen storage capacities in this thesis were obtained *via* a homemade Macro Excel file. The hydrogen storage capacity is described by two units:

1- The absorbed hydrogen atoms (H) per metal atom (M): H/M

2- Weight percent: $\text{wt.\%} = \left(\frac{m_{H_2}}{m_{H_2}+m_{metal}}\right).100$ Equation 2.13

Where m_{H_2} and m_{metal} are the mass of the hydrogen and metal, respectively.

2.3.1 Pressure-Composition-Isotherms

The reaction of metal-hydrogen is described by a pressure composition isotherm (PCI) curve. The PCI is the plot of the pressure versus composition or hydrogen absorption capacity at a constant temperature (isotherm). In a PCI, the material is exposed to hydrogen by small doses and after reaching stabilization of the pressure, another dose is added. A PCI curve is represented by three stages: at the first stage, the H_2 molecule is **ad**sorbed on the surface of the metal due to van der Waals interaction (physisorption), followed by a dissociation of the hydrogen molecule, then the atoms of hydrogen are **ab**sorbed into the metal lattice (chemisorption) occupying random positions inside the lattice forming a solid solution (α phase). The second stage is represented by a plateau, where the hydrogen atoms inside the lattice start forming an ordered array which is the hydride phase β, this results of a coexistence between α and β phases. The last stage is the slope at the right side of the plateau where the α phase is completely transformed, leaving only the β phase (figure 2.13).

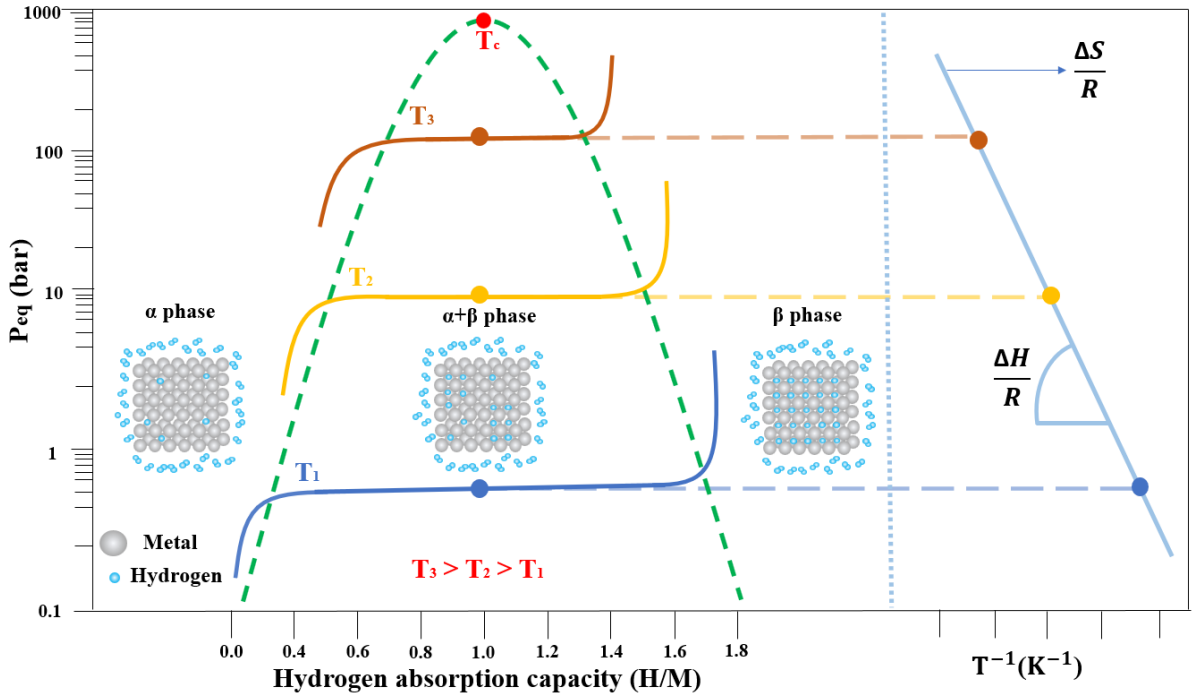

Figure 2.13. A typical Pressure Composition Isotherm of absorption at different temperatures (left) and the corresponding van't Hoff plot (right).

The increase of the temperature results in the increase of the plateau pressure as illustrated in figure 2.13. This variation is described by the van't Hoff law:

$$\ln(P_{eq}) = \frac{\Delta H}{RT} - \frac{\Delta S}{R} \qquad \text{Equation 2.14}$$

Where P_{eq} is the equilibrium plateau pressure, ΔH and ΔS are the enthalpy and entropy of hydride formation, respectively. R is the gas constant and T is the temperature of the

measured PCI. The thermodynamic properties are experimentally determined by measuring multiple PCIs at different temperatures as illustrated in figure 2.13. Following this, the van't Hoff plot could be constructed by knowing the P_{eq} of each PCI measurement with the corresponding temperature ($\ln(P_{eq})$ *vs* T^{-1}) as illustrated in figure 2.13 (right). For hydrogenation, the ΔH and ΔS are negative meaning the reaction is exothermic, whereas for the dehydrogenation, the reaction is endothermic [13].

2.3.2 Kinetics of hydrogen absorption - Cycling of hydrogen

Hydrogen absorption kinetic is also an interesting property that is studied in this project. The HEA sample is loaded in a stainless steel cell and connected to a Sievert apparatus. The sample is then exposed to 40-50 bar of hydrogen pressure at room temperature with recording of the pressure evolution with time. After reaching an equilibrium pressure, the analysis of the recorded data reveals many characteristics such as: the rate of absorption of hydrogen, presence of incubation time and the maximum of hydrogen absorption capacity.

The same procedure is used for cycling tests of hydrogen during absorption (50 bar of hydrogen pressure, at room temperature). After the absorption measurement, the hydride is desorbed by heat treatment at 400 °C for 5-12h under dynamic vacuum.

2.3.3 Thermo-Desorption-Spectroscopy

The desorption properties were studied by thermo-desorption spectroscopy (TDS). The TDS is a desorption characterization technique where a thermal energy is applied on hydrides with a constant heating rate under dynamic vacuum (10^{-6}mbar). The application of thermal energy on the hydrides results in the destabilization of the hydride phase at a certain temperature and the hydrogen is released from the sample (hydride). The partial pressure of the released hydrogen is measured and then plotted as a function of the temperature. The desorption profile provides the desorption characteristics of the studied hydrides such as the onset temperature (T_{onset}) (the first temperature at which the release of H_2 starts) and the temperature of the maximum desorption rate (T_{max}).

All the TDS measurements in this thesis were done by a homemade laboratory apparatus. The components of the used instrument are a quadruple mass spectrometer, Microvision Plus RGA from MKS instrument for the measurement of the desorbed hydrogen, a vacuum rig, and a turbopump reaching secondary vacuum. The hydride sample (mass: 10-15 mg) is placed in a silica tube that is inserted in an electric furnace. During all the measurement, the temperature is always monitored by a thermocouple that is in close contact with the sample. All the TDS measurements that are presented in this thesis are heated with a constant heating rate of T_{rate}= 1.0 °C/min from room temperature to ~ 450 °C (figure 2.14).

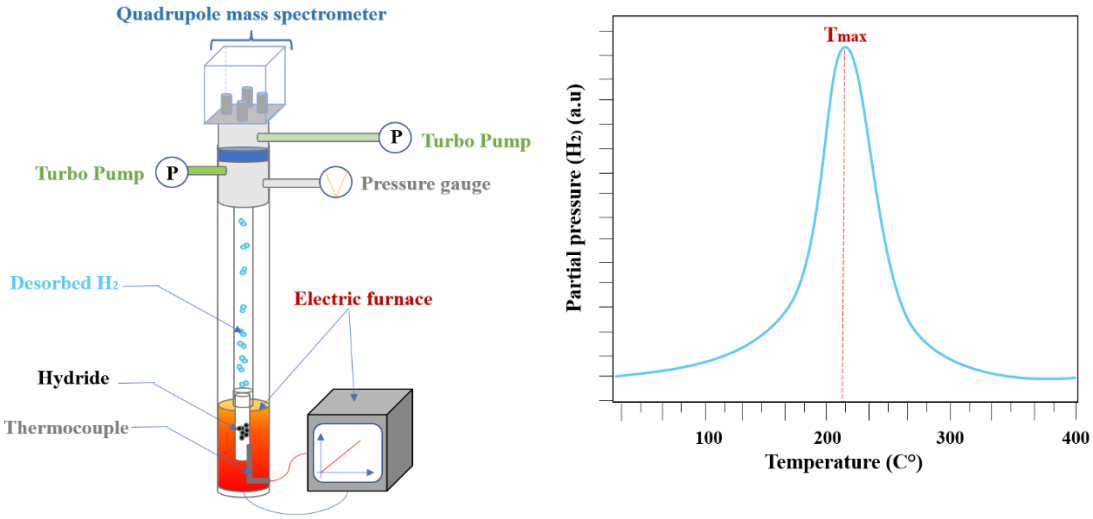

Figure 2.14. Schematic representation of the TDS laboratory instrument(left), typical TDS profile(right).

References

[1] J. Zhang, F. Cuevas, W. Zaïdi, J.-P. Bonnet, L. Aymard, J.-L. Bobet, M. Latroche, Highlighting of a Single Reaction Path during Reactive Ball Milling of Mg and TM by Quantitative H2 Gas Sorption Analysis To Form Ternary Complex Hydrides (TM = Fe, Co, Ni), J. Phys. Chem. C. 115 (2011) 4971–4979. https://doi.org/10.1021/jp2005293.

[2] A.S. Schlachter, F.J. Wuilleumier, eds., New Directions in Research with Third-Generation Soft X-Ray Synchrotron Radiation Sources, Springer Netherlands, Dordrecht, 1994. https://doi.org/10.1007/978-94-011-0868-3.

[3] V.K. Pecharsky, P.Y. Zavalij, Fundamentals of powder diffraction and structural characterization of materials, Springer, New York, NY, 2005.

[4] P. Thompson, D.E. Cox, J.B. Hastings, Rietveld refinement of Debye–Scherrer synchrotron X-ray data from Al2O3, J. Appl. Crystallogr. 20 (1987) 79–83. https://doi.org/10.1107/S0021889887087090.

[5] J. Rodríguez-Carvajal, AN INTRODUCTION TO THE PROGRAM, (n.d.).

[6] The rise of the X-ray atomic pair distribution function method: a series of fortunate events, (n.d.). https://doi.org/10.1098/rsta.2018.0413.

[7] X. Wang, S. Tan, X.-Q. Yang, E. Hu, Pair distribution function analysis: Fundamentals and application to battery materials, Chin. Phys. B. 29 (2020) 028802. https://doi.org/10.1088/1674-1056/ab6656.

[8] C.L. Farrow, P. Juhas, J.W. Liu, D. Bryndin, E.S. Božin, J. Bloch, T. Proffen, S.J.L. Billinge, PDFfit2 and PDFgui: computer programs for studying nanostructure in crystals, J. Phys. Condens. Matter. 19 (2007) 335219. https://doi.org/10.1088/0953-8984/19/33/335219.

[9] J. Kieffer, S. Petitdemange, T. Vincent, Real-time diffraction computed tomography data reduction, J. Synchrotron Radiat. 25 (2018) 612–617. https://doi.org/10.1107/S1600577518000607.

[10] G. Ashiotis, A. Deschildre, Z. Nawaz, J.P. Wright, D. Karkoulis, F.E. Picca, J. Kieffer, The fast azimuthal integration Python library: *pyFAI*, J. Appl. Crystallogr. 48 (2015) 510–519. https://doi.org/10.1107/S1600576715004306.

[11] P. Juhás, C.L. Farrow, X. Yang, K.R. Knox, S.J.L. Billinge, Complex modeling: a strategy and software program for combining multiple information sources to solve ill posed structure and nanostructure inverse problems, Acta Crystallogr. Sect. Found. Adv. 71 (2015) 562–568. https://doi.org/10.1107/S2053273315014473.

[12] T.P. Blach, E.MacA. Gray, Sieverts apparatus and methodology for accurate determination of hydrogen uptake by light-atom hosts, J. Alloys Compd. 446–447 (2007) 692–697. https://doi.org/10.1016/j.jallcom.2006.12.061.

[13] A. Züttel, Materials for hydrogen storage, Mater. Today. 6 (2003) 24–33. https://doi.org/10.1016/S1369-7021(03)00922-2.

CHAPTER III

Correlation of hydrogen sorption properties with empirical parameters in HEAs

Chapter 3. Correlation of hydrogen sorption properties with empirical parameters in HEAs

The design possibilities of HEAs are tremendously broad. Their multivariable space of possible combinations gives access to a wide range of variables for tracking down the optimal HEAs for hydrogen storage applications. Establishing correlations between well-known used empirical parameters (atomic size difference and valence electron concentration, as introduced in chapter 1) and hydrogen sorption properties could give rise to a guide for predicting and tuning compositions in order to obtain the optimal hydrogen sorption properties.

This chapter is dedicated to the study of a series of HEAs $Ti_{0.30}V_{0.25}Zr_{0.10}Nb_{0.25}M_{0.10}$ (*M*= Mg, Al, Cr, Mn, Fe, Co, Ni, Cu, Zn, Mo, and Ta) and the quaternary alloy $Ti_{0.325}V_{0.275}Zr_{0.125}Nb_{0.275}$. The data of the three quinary alloys $Ti_{0.30}V_{0.25}Zr_{0.10}Nb_{0.25}M_{0.10}$ (*M*= Mg, Al, and Ta) and the quaternary alloy $Ti_{0.325}V_{0.275}Zr_{0.125}Nb_{0.275}$ that were previously studied in the PhD thesis by J.Montero (already mentioned in chapter 1) will be included in this work. The purpose is to have a broader pool of samples and to increase the accuracy of the correlations. Here we report the synthesis and the characterization of the structure, microstructure, and chemical homogeneity of HEAs before and after hydrogenation at room temperature, along with the desorption properties of all the hydrides. Moreover, the obtained results will be discussed and correlated with various empirical parameters.

3.1 Synthesis of the HEA series

Various methods of synthesis were used to form the investigated HEAs, hence, table 3.1 provides a summary of all the results obtained from the synthesis by arc melting (AM) and ball milling under Ar atmosphere (BM) as a reference for the reader. The used radii of all the elements to calculate the lattice distortion parameter (δ) were all obtained from reference [1].

Thesis work	*M*	Synthesis	δ(%)	VEC	Initial phase	a_{bcc} (Å)
J.Montero[2]	∅	AM BM	6.0	4.55	*bcc* *bcc*	3.261 (1) 3.270 (1)
J.Montero[3]	Mg	BM	6.6	4.3	*bcc*	3.273 (1)
J.Montero[4]	Al	AM	5.5	4.4	*bcc*	3.247 (1)
Present[5]	Cr	AM	6.7	4.7	*bcc*	3.225 (1)
Present[6]	Mn	AM	5.7	4.8	*bcc*	3.239 (5)
Present	Fe	AM BM	6.8	4.9	*multiphase* *bcc*	- 3.277 (1)
Present	Co	AM BM	6.7	5.0	*multiphase* *bcc*	- 3.299 (8)
Present	Ni	AM BM	6.7	5.1	*multiphase* *bcc*	- 3.296 (4)
Present	Cu	AM BM	6.4	5.2	*multiphase* *bcc*	- 3.278 (4)
Present	Zn	BM	5.9	5.3	*bcc*	3.279 (3)
Present[7]	Mo	AM	5.7	4.7	*bcc*	3.240 (3)
J.Montero[8]	Ta	AM	5.5	4.6	*bcc*	3.263 (3)

Table 3.1. The method of synthesis (arc melting (AM), ball milling under Ar (BM)), the empirical parameters (δ and VEC), the initial formed phase structure with the corresponding lattice parameter of the HEA series $Ti_{0.30}V_{0.25}Zr_{0.10}Nb_{0.25}M_{0.10}$ (with *M*= Mg, Al, Cr, Mn, Fe, Co, Ni, Cu, Zn, Mo, and Ta) and the parent alloy $Ti_{0.325}V_{0.275}Zr_{0.125}Nb_{0.275}$ (∅).

3.1.1 HEA synthesis: Arc melting

Arc melting is used as the first technique for synthesizing the investigated HEAs, due to its effectiveness for forming alloys from refractory elements. XRD investigations allowed us to identify two classes of materials:

A. $Ti_{0.30}V_{0.25}Zr_{0.10}Nb_{0.25}M_{0.10}$ (with *M*= Al, Cr, Mn, Mo, and Ta)
B. $Ti_{0.30}V_{0.25}Zr_{0.10}Nb_{0.25}M_{0.10}$ (with *M*= Fe, Co, Ni, and Cu)

This section will be subdivided into two subsections dedicated to investigating both classes of the latter mentioned materials.

3.1.1.A HEA synthesis: $Ti_{0.30}V_{0.25}Zr_{0.10}Nb_{0.25}M_{0.10}$ (with *M*= Al, Cr, Mn, Mo, and Ta)

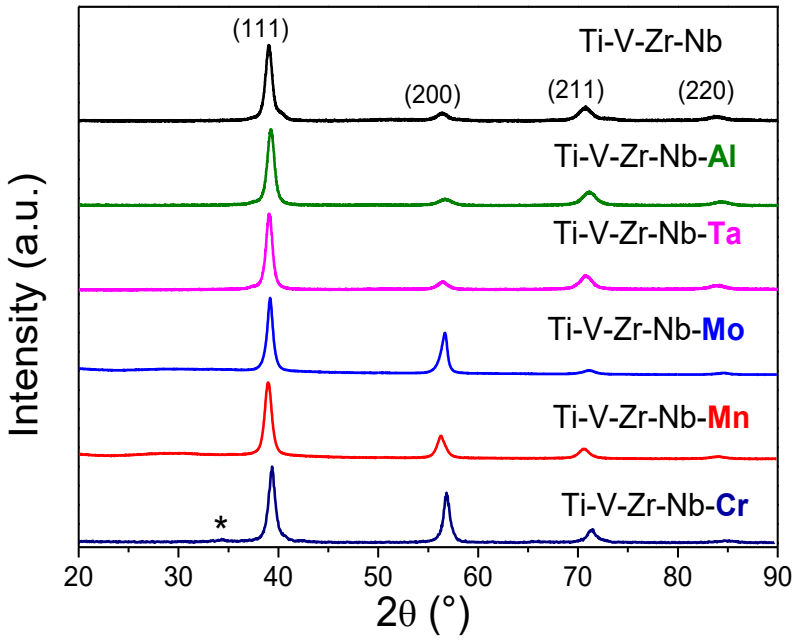

Figure 3.1. X-ray diffraction patterns (λ=1.5406 Å) of the as-cast alloys $Ti_{0.30}V_{0.25}Zr_{0.10}Nb_{0.25}M_{0.10}$ (*M*= Al, Cr, Mn, Mo, and Ta) and $Ti_{0.325}V_{0.275}Zr_{0.125}Nb_{0.275}$ synthesized by arc melting.

Figure 3.1 shows the XRD patterns of the following alloys series $Ti_{0.30}V_{0.25}Zr_{0.10}Nb_{0.25}M_{0.10}$ (*M*= Al, Cr, Mn, Mo, and Ta) and $Ti_{0.325}V_{0.275}Zr_{0.125}Nb_{0.275}$. All the HEAs adopt a single phase *bcc* structure ($Im\bar{3}m$). The $Ti_{0.30}V_{0.25}Cr_{0.10}Zr_{0.10}Nb_{0.25}$ alloy contained a small unidentified impurity (marked with *) (figure 3.1). All the lattice parameters of the *bcc* phase of each HEA are listed in table 3.1. The existence of the small impurity of the $Ti_{0.30}V_{0.25}Cr_{0.10}Zr_{0.10}Nb_{0.25}$ alloy could be explained by the high lattice distortion δ= 6.7% of this composition, which could lead to the formation of multiple phases including intermetallic structures [9].

Following AM synthesis, these samples were investigated regarding their microstructure and chemical composition *via* SEM and EDS as illustrated in table 3.2 and figure 3.2.(a)-(f).

$Ti_{0.325}V_{0.275}Zr_{0.125}Nb_{0.275}$

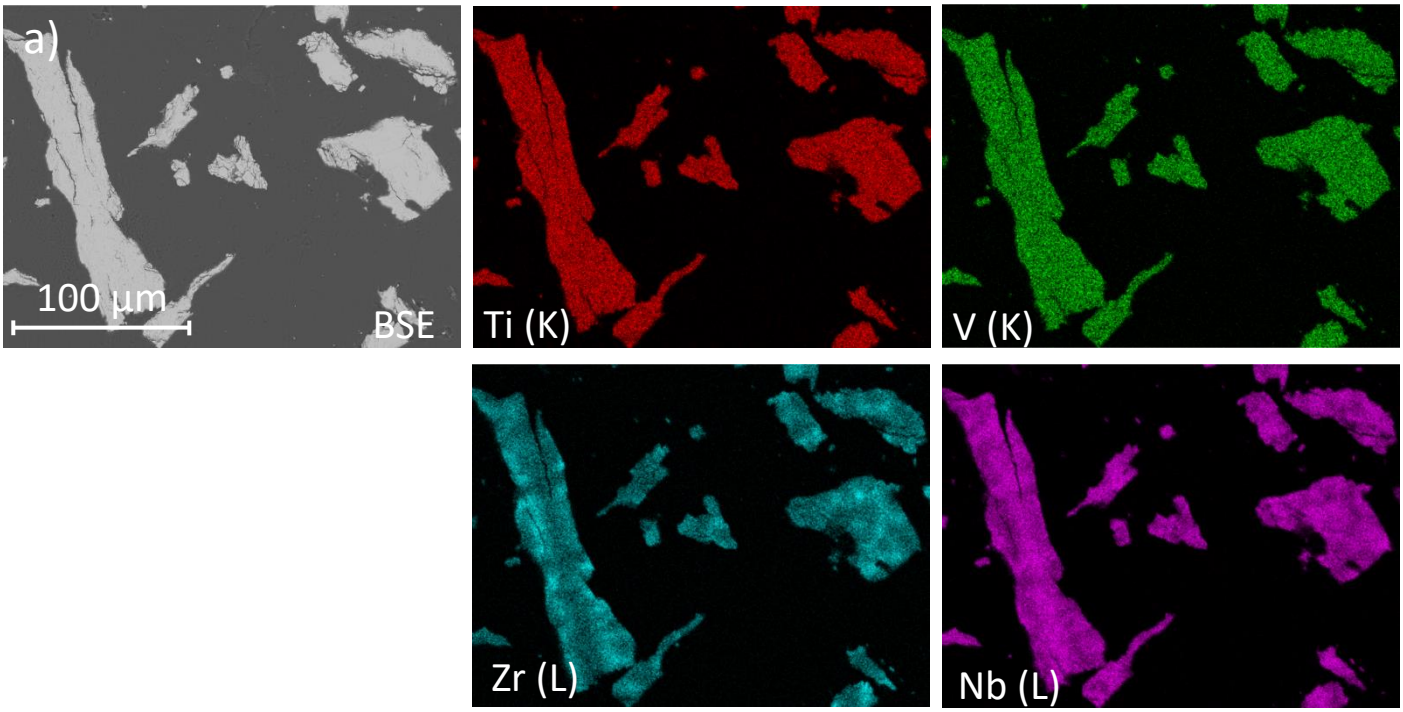

$Ti_{0.30}V_{0.25}Al_{0.10}Zr_{0.10}Nb_{0.25}$

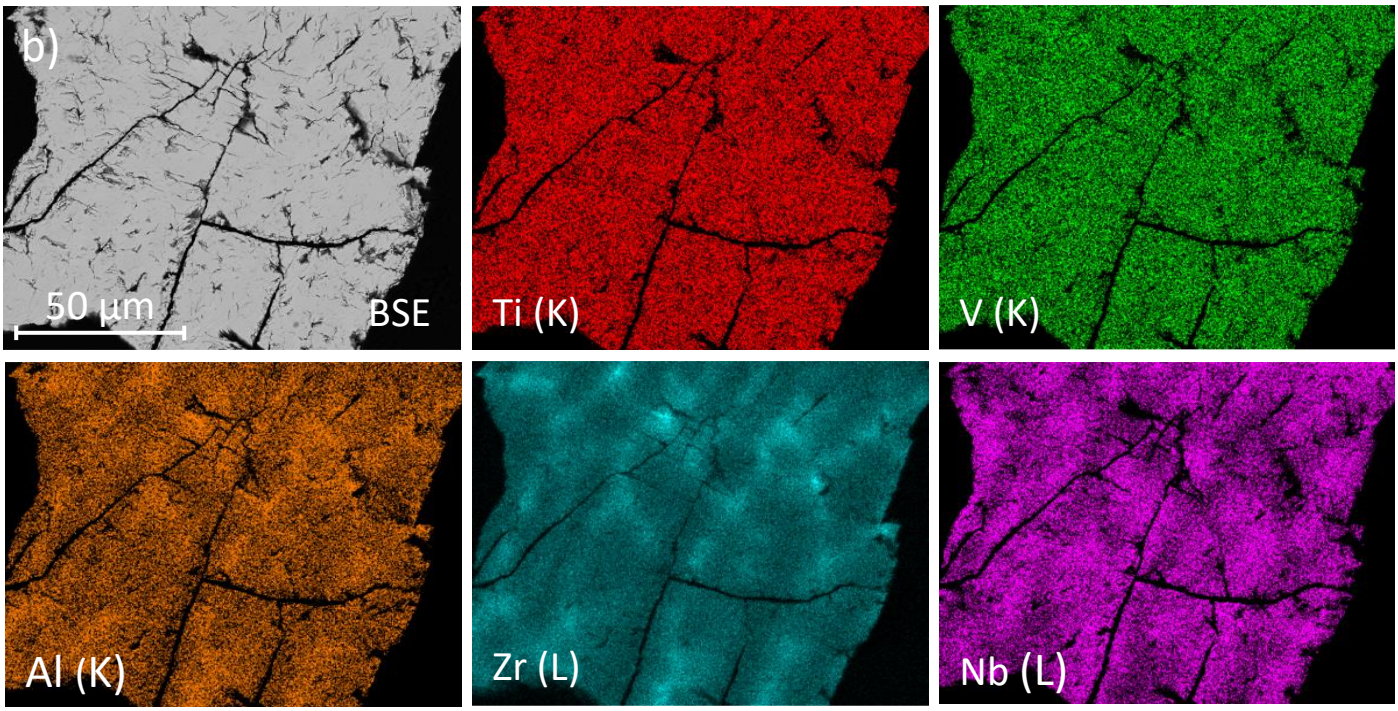

$Ti_{0.30}V_{0.25}Zr_{0.10}Nb_{0.25}Ta_{0.10}$

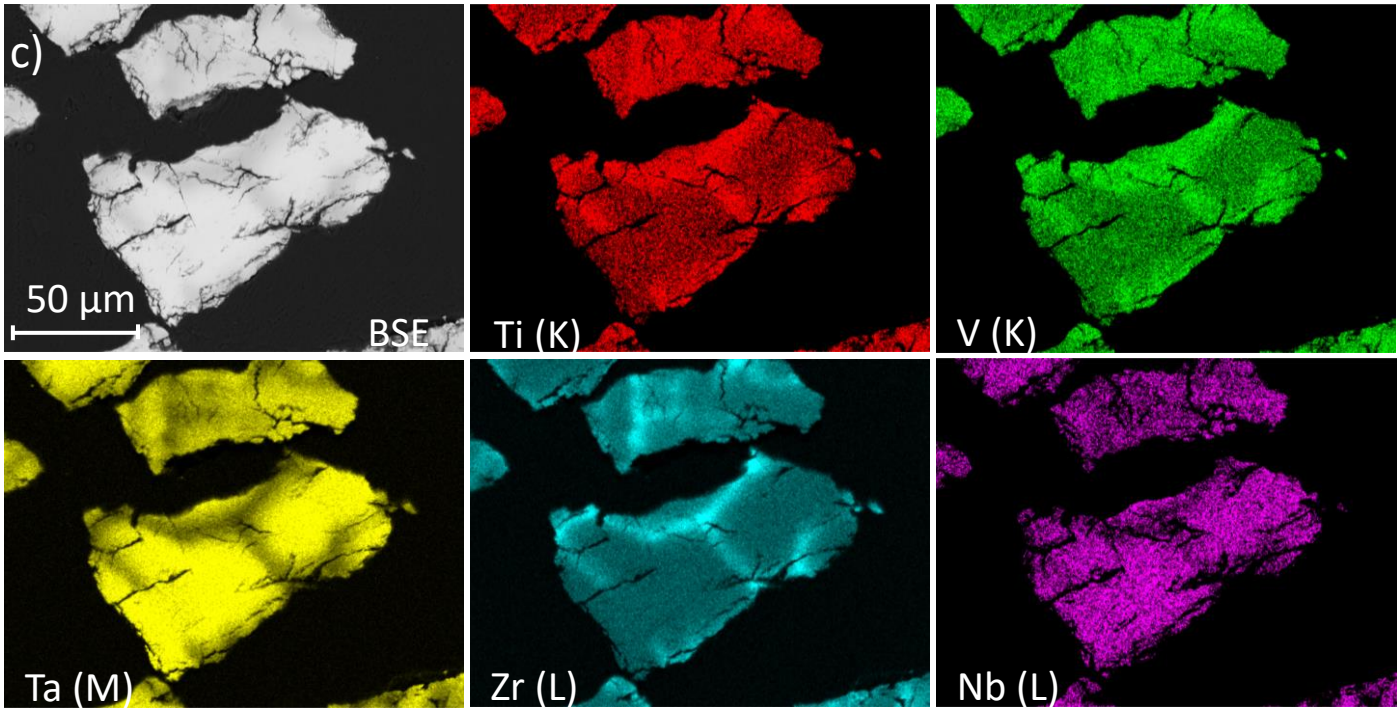

$Ti_{0.30}V_{0.25}Zr_{0.10}Nb_{0.25}Mo_{0.10}$

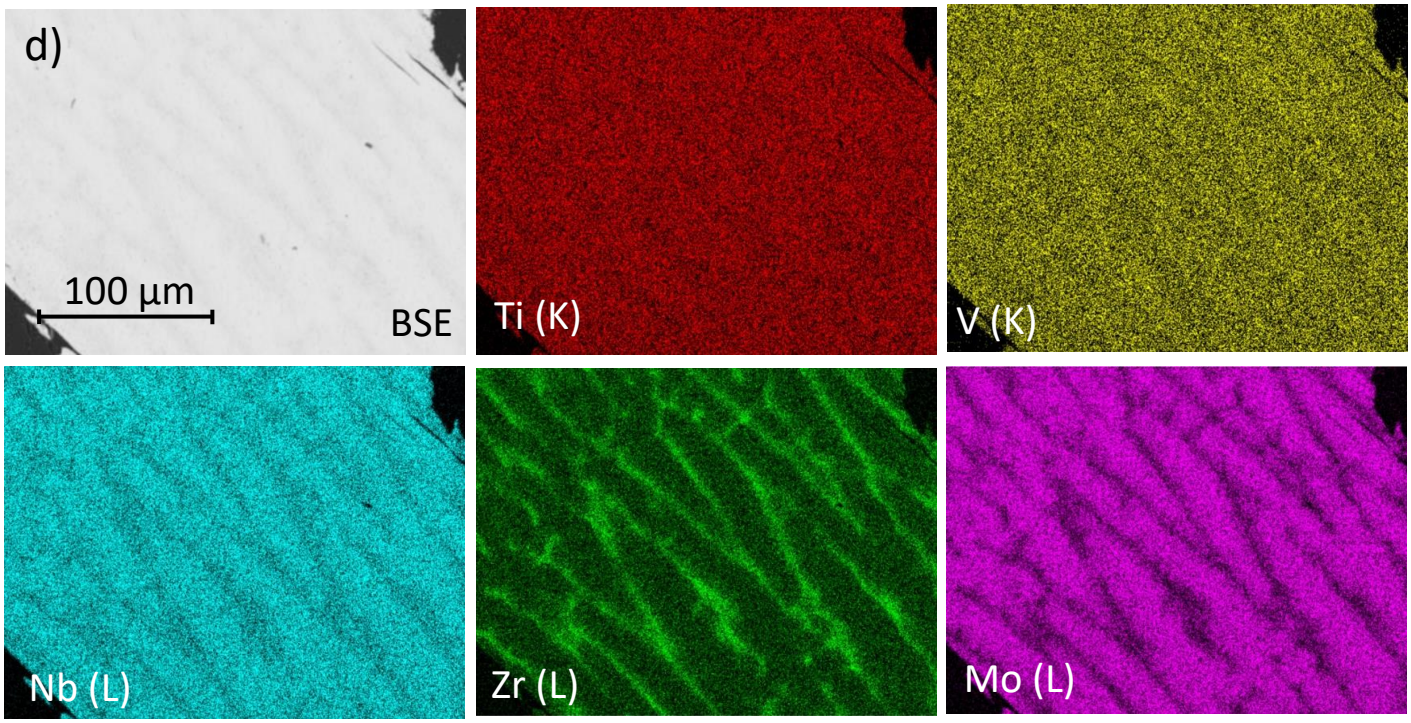

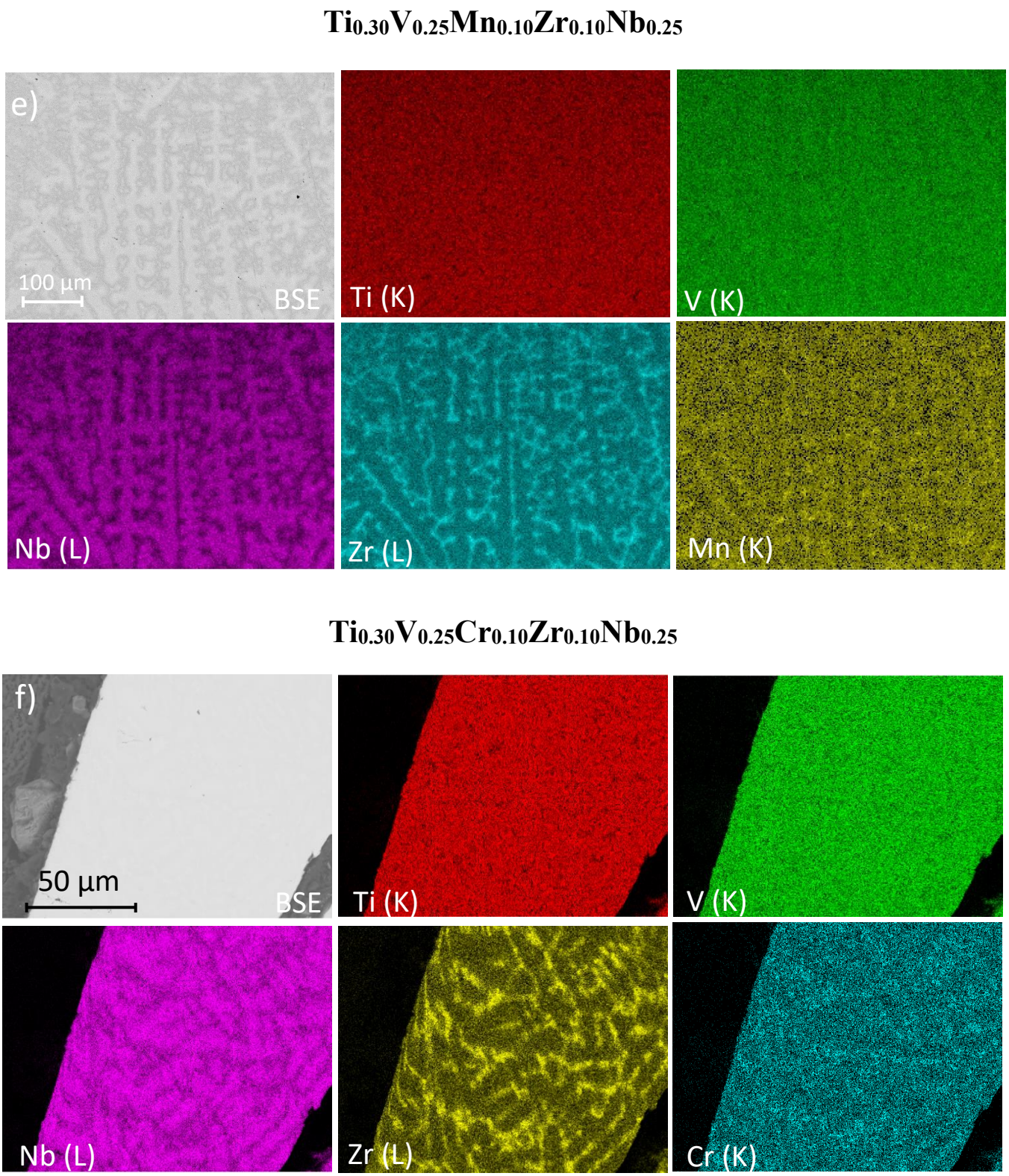

Figure 3.2. EDS chemical mapping of as-cast AM alloys: a) $Ti_{0.325}V_{0.275}Zr_{0.125}Nb_{0.275}$ and $Ti_{0.30}V_{0.25}Zr_{0.10}Nb_{0.25}M_{0.10}$ (*M*= Al (b), Ta (c), Mo(d), Mn(e), and Cr (f)).

Alloy	Region	Ti (at.%)	V (at.%)	Zr (at.%)	Nb (at.%)	Al (at.%)	Ta (at.%)	Mo (at.%)	Mn (at.%)	Cr (at.%)
$Ti_{0.325}V_{0.275}Zr_{0.125}Nb_{0.275}$	Dendritic	32.1 (0.3)	26.9 (0.4)	10.8 (0.8)	30.2 (1.1)					
	Interdendritic	32.2 (0.3)	25.5 (0.4)	21.8 (1.7)	20.5 (1.4)					
	Overall	32.4 (0.3)	27.1 (0.4)	13.2 (0.8)	27.3 (1.1)					
$Ti_{0.30}V_{0.25}Al_{0.10}Zr_{0.10}Nb_{0.25}$	Dendritic	29.8 (0.6)	24.7 (0.7)	8.3 (0.6)	28.0 (0.5)	9.2 (0.4)				
	Interdendritic	28.7 (0.9)	22.6 (1.2)	17.5 (2.5)	19.1 (1.6)	12.1 (0.6)				
	Overall	29.5 (0.6)	24.6 (0.7)	10.8 (0.6)	25.1 (0.5)	10.0 (0.4)				
$Ti_{0.30}V_{0.25}Zr_{0.10}Nb_{0.25}Ta_{0.10}$	Dendritic	25.91 (1.0)	20.33 (0.7)	5.56 (0.3)	32.16 (0.8)		16.05 (0.9)			
	Interdendritic	30.82 (0.6)	25.58 (1.1)	21.11 (2.9)	17.88 (1.3)		4.62 (0.8)			
	Overall	28.5 (1.0)	24.29 (0.7)	9.68 (0.3)	26 (0.8)		11.53 (0.9)			
$Ti_{0.30}V_{0.25}Zr_{0.10}Nb_{0.25}Mo_{0.10}$	Dendritic	28.2 (0.5)	22.9 (0.2)	6.2 (0.4)	29.8 (0.7)			12.9 (0.4)		
	Interdendritic	30.4 (0.3)	25.5 (0.4)	23.6 (1.7)	15.9 (2.4)			4.9 (1.2)		
	Overall	30.1 (0.7)	24.8 (0.5)	10.3 (1.4)	25.1 (1.4)			9.7 (0.8)		
$Ti_{0.30}V_{0.25}Mn_{0.10}Zr_{0.10}Nb_{0.25}$	Dendritic	29.4 (0.2)	24.4 (0.8)	6.5 (1.2)	28.2 (1.8)				11.5 (1.3)	
	Interdendritic	30.2 (0.6)	25.5 (0.9)	15.5 (1.8)	20.7 (1.5)				8.1 (1.2)	
	Overall	29.9 (0.5)	24.9 (0.6)	10.5 (1.2)	25.2 (1.1)				9.5 (1.0)	
$Ti_{0.30}V_{0.25}Cr_{0.10}Zr_{0.10}Nb_{0.25}$	Dendritic	28.2 (0.5)	22.9 (0.2)	6.2 (0.4)	29.8 (0.7)					12.9 (0.4)
	Interdendritic	30.4 (0.3)	25.5 (0.4)	23.6 (1.7)	15.9 (2.4)					4.9 (1.2)
	Overall	30.1 (0.7)	24.8 (0.5)	10.3 (1.4)	25.1 (1.4)					9.7 (0.8)

Table 3.2. Chemical composition of the dendritic and interdendritic regions, as well as the overall values for the as-cast $Ti_{0.325}V_{0.275}Zr_{0.125}Nb_{0.275}$ and alloys.

The chemical mapping shows the formation of dendritic microstructures for $Ti_{0.30}V_{0.25}Zr_{0.10}Nb_{0.25}M_{0.10}$ (*M*= Al, Ta, Mo, Mn, and Cr) and $Ti_{0.325}V_{0.275}Zr_{0.125}Nb_{0.275}$ alloys (figure 3.2 (a)-(f)). Interestingly, in all the analyzed samples, the EDS analysis of the chemical composition showed the same variation of elements in both dendritic and interdendritic regions (table 3.2). During the solidification process of the AM samples, the phase containing elements with high melting temperature (T_m) will begin to solidify, thus creating dendrites. As listed in table 3.2, Nb was found to be distributed more throughout the dendritic regions in all the alloys, this is because Nb has one of the highest melting temperatures (T_m= 2420 °C) when compared

to the other constituent elements of the alloys. Contrary to the latter case, Zr (T_m= 1852 °C) is more present in the interdendritic regions, whereas the Ti (T_m= 1660 °C) and V (T_m= 1910 °C) were homogeneously distributed throughout both regions and the overall values were close to those of the desired composition. Moreover, the fifth added elements followed the same distribution (elements with high T_m are more present in the dendritic regions), for example, Ta (T_m= 3000 °C), Mo (T_m= 2610 °C), and Cr (T_m= 1907 °C) are more present in the dendritic regions (table 3.2). Furthermore, due to the low melting temperature of Al (T_m= 660 °C), it is found to be more present in the interdendritic regions (table 3.2). The distribution of Mn was almost homogenous in both dendritic and interdendritic regions due to its relatively low melting temperature (T_m= 1244°C) which is close to the average temperature of the HEA. Similar distribution of elements during the solidification process has been seen in multiple studies on refractory HEAs [10–12].

3.1.1.B HEA synthesis: $Ti_{0.30}V_{0.25}Zr_{0.10}Nb_{0.25}M_{0.10}$ (with *M*= Fe, Co, Ni, and Cu)

The rest of the AM series $Ti_{0.30}V_{0.25}Zr_{0.10}Nb_{0.25}M_{0.10}$ (*M*= Fe, Co, Ni, and Cu) formed a *bcc* phase along with *C14* ($MgZn_2$) or *C15* ($MgCu_2$) Laves phase (figure 3.3). As seen in chapter 1, HEAs with high distortions (δ>6.6%) could lead to the formation of multiple phases including intermetallic precipitations. This is the case for the present studied HEAs containing Fe, Co, Ni, and Cu. Moreover, the combination of the fifth added element (Fe, Co, Ni, and Cu) with the other constituent elements (Ti, Zr, and Nb) could lead to the formation of stable binary and ternary Laves phases. This was confirmed in the binary phase diagrams of the combination of both groups of elements (Fe, Co, Ni, and Cu) with (Ti, Zr, and Nb) [13].

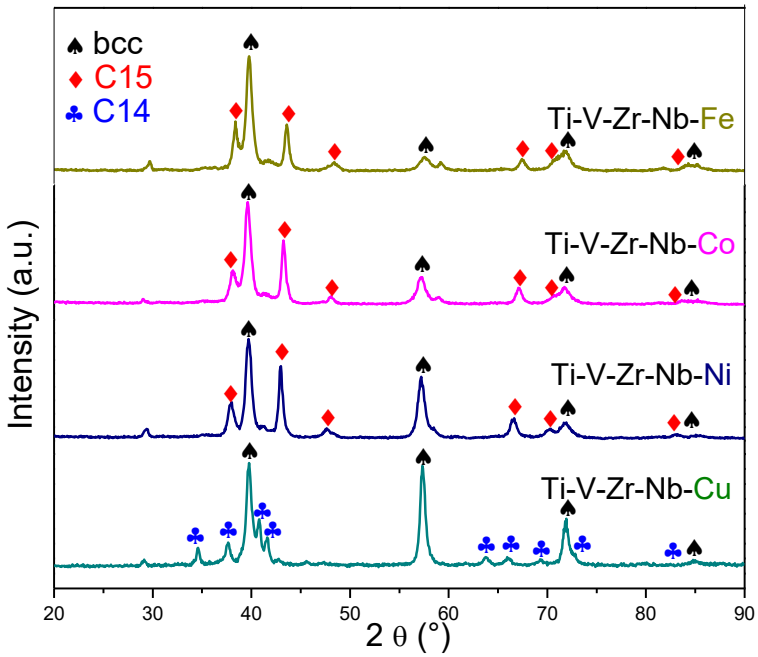

Figure 3.3. X-ray diffraction patterns (λ=1.5406 Å) of $Ti_{0.30}V_{0.25}Zr_{0.10}Nb_{0.25}M_{0.10}$ (*M*= Fe, Co, Ni, and Cu) as-cast alloys synthesized by arc melting. The *bcc*, *C15*, and *C14* phases are marked with black spades, red diamonds, and blue clubs, respectively.

In conclusion, the use of the AM method resulted in the formation of multiphase materials instead of single *bcc* phases. Hence, ball milling (BM) is known to form metastable phases, which can be an alternative method of synthesis to avoid the formation of too stable Laves phases.

The BM method is used to synthesize HEAs forming intermetallic phases when synthesized by AM, but also HEAs containing elements with low melting point such as Zn (T_m= 419 °C). Moreover, J.Montero used BM to synthesize $Ti_{0.30}V_{0.25}Zr_{0.10}Nb_{0.25}Mg_{0.10}$ alloy because of the low melting temperature and high vapor pressure of Mg [3].

In order to obtain the precise milling conditions of $Ti_{0.30}V_{0.25}Zr_{0.10}Nb_{0.25}M_{0.10}$ (*M*= Fe, Co, Ni, Cu, and Zn) to form a single phase materials, we investigated BM of $Ti_{0.30}V_{0.25}Zr_{0.10}Nb_{0.25}Zn_{0.10}$ following these steps: cycles of continuous BM for 15 min, with a pause of 15 min between each cycle. During the 15 min pause, a portion of the sample was extracted from the vial to be analyzed by XRD for the purpose of following the phase formation during the milling (figure 3.4).

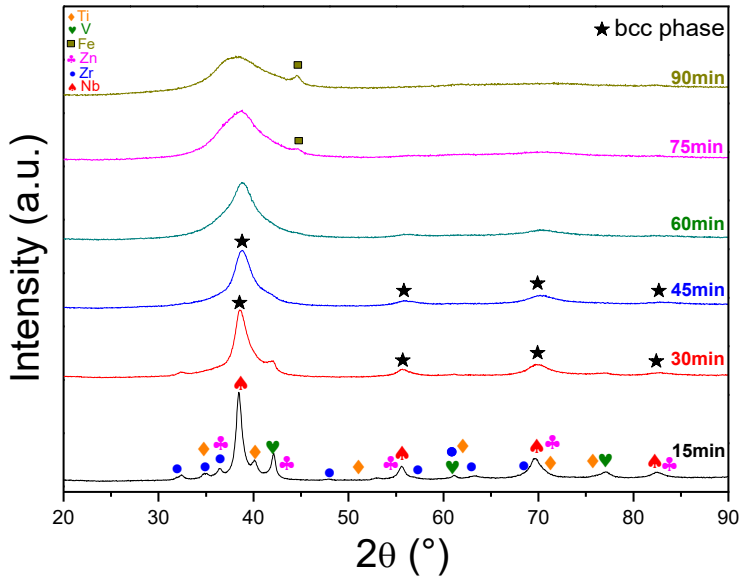

Figure 3.4. X-ray diffraction patterns (λ=1.5406 Å) of $Ti_{0.30}V_{0.25}Zr_{0.10}Nb_{0.25}Zn_{0.10}$ alloy at different times (from 15 min to 90 min) after BM. Individual elements Ti, V, Fe, Zn, Zr, and Nb are marked with orange diamonds, green heart, dark yellow square, pink clubs, blue circle, and red spades, respectively.

Figure 3.4 illustrates the phase evolution during BM of the $Ti_{0.30}V_{0.25}Zr_{0.10}Nb_{0.25}Zn_{0.10}$ alloy. XRD after 15 min of BM showed the co-existence of multiple phases that were identified as those of the constituent elements of the HEA (figure 3.4). After 30 min of milling, a main *bcc* phase was gradually formed on the expense of other phases. The sample after 45 min BM showed an almost single *bcc* phase. Further milling (60 min - 90 min) introduced amorphization which was observed in the XRD patterns by the broadening of the diffraction peaks. The severe grinding of the material leads to multiple structural defects resulting in the formation of an amorphous phase [14].

As a conclusion, the $Ti_{0.30}V_{0.25}Zr_{0.10}Nb_{0.25}Zn_{0.10}$ alloy synthesis by BM showed that alloys can form single phase materials within 45 to 60 min. Hence, the HEAs containing Fe, Co, Ni, and Cu will be synthesized by BM with the latter discovered conditions.

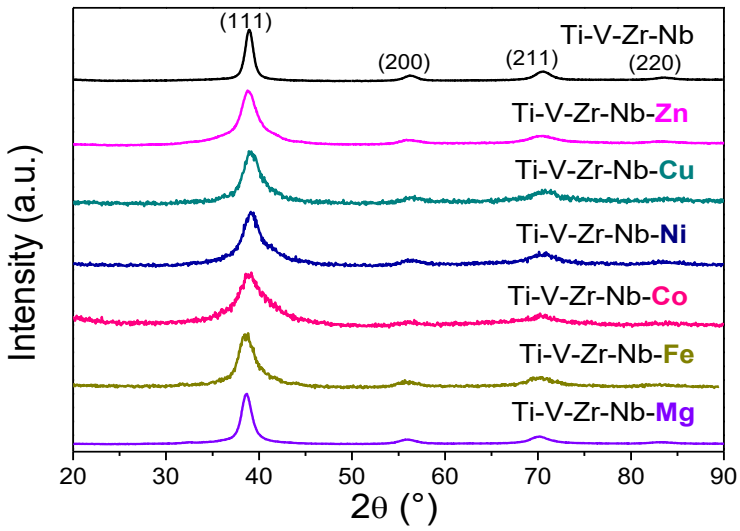

Figure 3.5. X-ray diffraction patterns (λ=1.5406 Å) of the as-cast alloys $Ti_{0.30}V_{0.25}Zr_{0.10}Nb_{0.25}M_{0.10}$ (*M*= Zn, Cu, Ni, Co, Fe, and Mg) and $Ti_{0.325}V_{0.275}Zr_{0.125}Nb_{0.275}$ synthesized by ball milling under Ar atmosphere (after 45 min – 60 min).

Figure 3.5 illustrated the XRD patterns of $Ti_{0.30}V_{0.25}Zr_{0.10}Nb_{0.25}M_{0.10}$ (*M*= Zn, Cu, Ni, Co, Fe, and Mg) and $Ti_{0.325}V_{0.275}Zr_{0.125}Nb_{0.275}$. All HEAs were successfully synthesized by BM forming a single phase *bcc* after 45 min – 60 min. The lattice parameters of the formed phase of each HEA are listed in table 3.1.

3.1.2 Correlation with empirical parameters

HEAs contain at least 5 elements, for each element the concentration can vary from 5 at.% to 35 at.%. Hence, it is crucial to draw trends to clarify the compositional effects on the phase formation. Thus, this work is based on limiting the variations of the chemical composition of HEAs by just altering one element without varying its concentration (10 at.%) and to obtain single phase materials. Consequently, the novel strategy will enable us to predict the effects of the chemical composition on HEA properties. The series of HEAs $Ti_{0.30}V_{0.25}Zr_{0.10}Nb_{0.25}M_{0.10}$ (with *M*= Mg, Al, Cr, Mn, Fe, Co, Ni, Cu, Zn, Mo, and Ta) and the parent alloy $Ti_{0.325}V_{0.275}Zr_{0.125}Nb_{0.275}$ were successfully synthesized by AM and BM and crystallizes in a single phase *bcc* lattice. This result enables the collection of sufficient data to correlate it with empirical parameters and to explore the resulting trends.

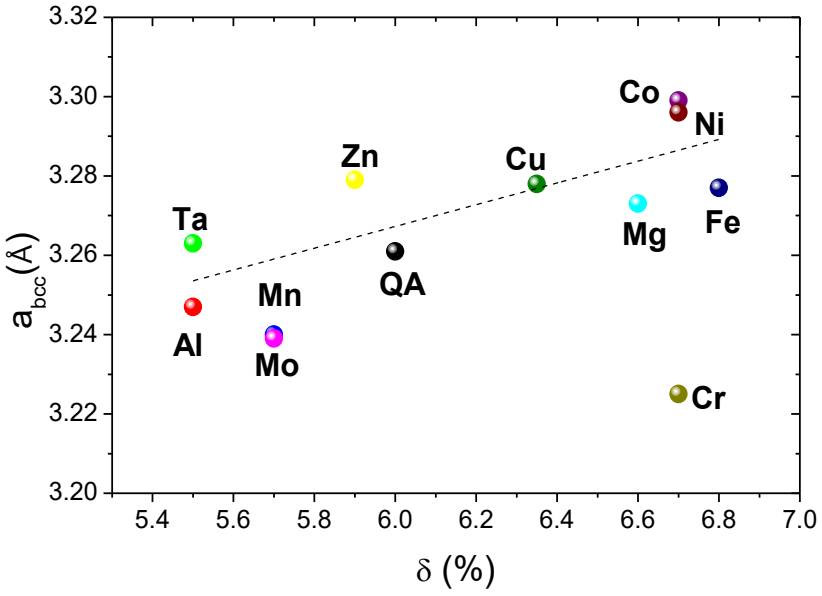

Figure 3.6. *bcc* lattice parameters *vs.* the lattice distortion of the series $Ti_{0.30}V_{0.25}Zr_{0.10}Nb_{0.25}M_{0.10}$ (with *M*= Mg, Al, Cr, Mn, Fe, Co, Ni, Cu, Zn, Mo, and Ta) and the parent alloy $Ti_{0.325}V_{0.275}Zr_{0.125}Nb_{0.275}$ (symbol: QA).

In figure 3.6, the *bcc* lattice parameters of both AM and BM alloys present an interesting increasing trend when plotted against the lattice distortion (δ). However, this trend is weak, especially when the $Ti_{0.30}V_{0.25}Zr_{0.10}Nb_{0.25}Cr_{0.10}$ alloy is involved which further weakens the correlation. The reason for this is due to the presence of an impurity in this alloy, that could affect the value of the *bcc* lattice parameter. Moreover, it is important to highlight the effect of the method of synthesis used either AM or BM. The samples that are synthesized by BM form metastable phases [15], with broad diffraction peaks affecting the accuracy of the refined lattice parameters.

3.2 Direct synthesis of HEA hydrides

The RBM synthesis method is used to directly form hydrides of HEAs. Only alloys that were synthesized by BM will also be synthesized by RBM. For the purpose of clarity for the reader, table 3.3 shows all the different methods of synthesis (AM, BM, and RBM) and their corresponding results.

In the RBM process, there are sensors in the vial that provides data about the pressure and temperature evolution during the milling, which enables the recording of the hydrogen absorption kinetics. Figure 3.7 illustrates the profiles of hydrogen absorption kinetics of the

HEA series $Ti_{0.30}V_{0.25}Zr_{0.10}Nb_{0.25}M_{0.10}$ (with *M*= Co, Ni, Cu, and Zn) and the quaternary alloy $Ti_{0.325}V_{0.275}Zr_{0.125}Nb_{0.275}$.

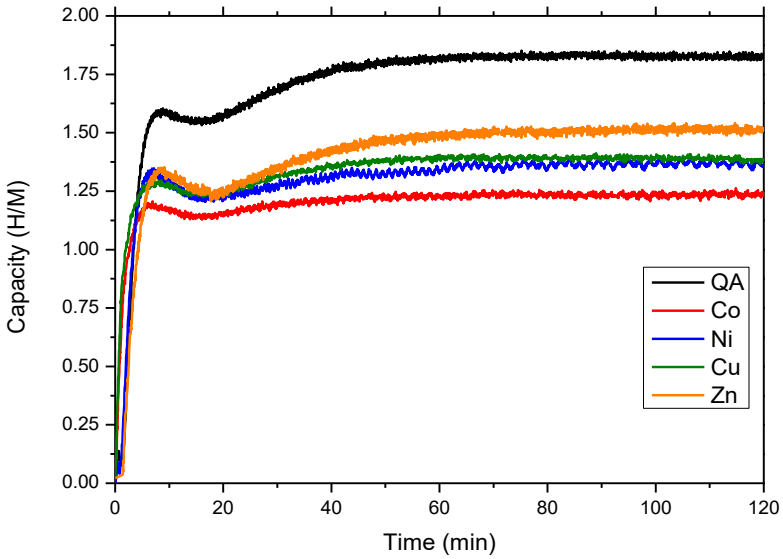

Figure 3.7. Profiles of kinetics of absorption of $Ti_{0.30}V_{0.25}Zr_{0.10}Nb_{0.25}M_{0.10}$ (with *M*= Co, Ni, Cu, and Zn) and the parent alloy $Ti_{0.325}V_{0.275}Zr_{0.125}Nb_{0.275}$ (symbol: QA).

J.Montero reported the phase evolution during the RBM synthesis of the quaternary alloy $Ti_{0.325}V_{0.275}Zr_{0.125}Nb_{0.275}$[2]. In the present work, only the profiles of the $Ti_{0.30}V_{0.25}Zr_{0.10}Nb_{0.25}M_{0.10}$ (with *M*= Co, Ni, Cu, and Zn) alloys were recorded. Figure 3.7 illustrates the different events occurring during the RBM synthesis. The first 5 min, a solid-gas reaction of the elemental powders and hydrogen gas occurred leading to a high hydrogen uptake reaching 1.5 H/M, 1.2 H/M, 1.35 H/M, 1.29 H/M, and 1.35 H/M for the quaternary, $Ti_{0.30}V_{0.25}Co_{0.10}Zr_{0.10}Nb_{0.25}$, $Ti_{0.30}V_{0.25}Ni_{0.10}Zr_{0.10}Nb_{0.25}$, $Ti_{0.30}V_{0.25}Cu_{0.10}Zr_{0.10}Nb_{0.25}$, and $Ti_{0.30}V_{0.25}Zn_{0.10}Zr_{0.10}Nb_{0.25}$ alloys, respectively. Simultaneously, a solid-solid reaction was taking place leading to the formation of unknown phases (see reference [2]). After the first event, a drop of capacity followed by a plateau is observed (5 to 20 min). The small decrease of capacity of absorption is due to the temperature increase which influences the pressure of hydrogen inside the vial. The increase of temperature is induced by the solid-gas reaction taking place. Following this, both solid-solid and solid-gas reactions are occurring simultaneously, and the capacity of hydrogen uptake continues to slightly increase, forming a single phase *fcc* ($Fm\bar{3}m$) hydride. The capacity of hydrogen uptake from RBM synthesis and the hydride phase together with the corresponding lattice parameter are listed in table 3.3.

Thesis work	*M*	Synthesis	δ(%)	VEC	Initial phase	a_{bcc} (Å)	Hydride phase	a_{fcc} (Å)	RBM Capacity (H/M)
J.Montero[2]	∅	AM			*bcc*	3.261 (1)	-	-	-
		BM	6.0	4.55	*bcc*	3.270 (1)	-	-	-
		RBM			-	-	*fcc*	4.474 (1)	1.8
J.Montero[3]	Mg	BM	6.6	4.3	*bcc*	3.273 (1)	-	-	-
		RBM				-	*fcc*	4.492 (1)	1.65
J.Montero[4]	Al	AM	5.5	4.4	*bcc*	3.247 (1)	-	-	-
Present[5]	Cr	AM	6.7	4.7	*bcc*	3.225 (1)	-	-	-
Present[6]	Mn	AM	5.7	4.8	*bcc*	3.239 (5)	-	-	-
Present	Fe	AM			*C14/C15/bcc*	-	-	-	-
		BM	6.8	4.9	*bcc*	3.277 (1)	-	-	-
		RBM			-	-	*fcc*	4.505 (3)	1.34
Present	Co	AM			*C14/C15/bcc*	-	-	-	-
		BM	6.7	5.0	*bcc*	3.299 (8)	-	-	-
		RBM			-	-	*fcc*	4.508 (3)	1.23
Present	Ni	AM			*C14/C15/bcc*	-	-	-	-
		BM	6.7	5.1	*bcc*	3.296 (4)	-	-	-
		RBM			-	-	*fcc*	4.500 (3)	1.4
Present	Cu	AM			*C14/bcc*	-	-	-	-
		BM	6.4	5.2	*bcc*	3.278 (4)	-	-	-
		RBM			-	-	*fcc*	4.499 (1)	1.38
Present	Zn	BM	5.9	5.3	*bcc*	3.279 (3)	-	-	-
		RBM			-	-	*fcc*	4.506 (4)	1.51
Present[7]	Mo	AM	5.7	4.7	*bcc*	3.240 (3)	-	-	-
J.Montero[8]	Ta	AM	5.5	4.6	*bcc*	3.263 (3)	-	-	-

Table 3.3. The method of synthesis (arc melting (AM), ball milling under Ar (BM), and reactive ball milling (RBM)), the empirical parameters (δ and VEC), the initial formed phase structure and hydride RBM phase with the corresponding lattice parameter and the capacity of absorption of the HEA series $Ti_{0.30}V_{0.25}Zr_{0.10}Nb_{0.25}M_{0.10}$ (with *M*= Mg, Al, Cr, Mn, Fe, Co, Ni, Cu, Zn, Mo, and Ta) and the parent alloy $Ti_{0.325}V_{0.275}Zr_{0.125}Nb_{0.275}$.

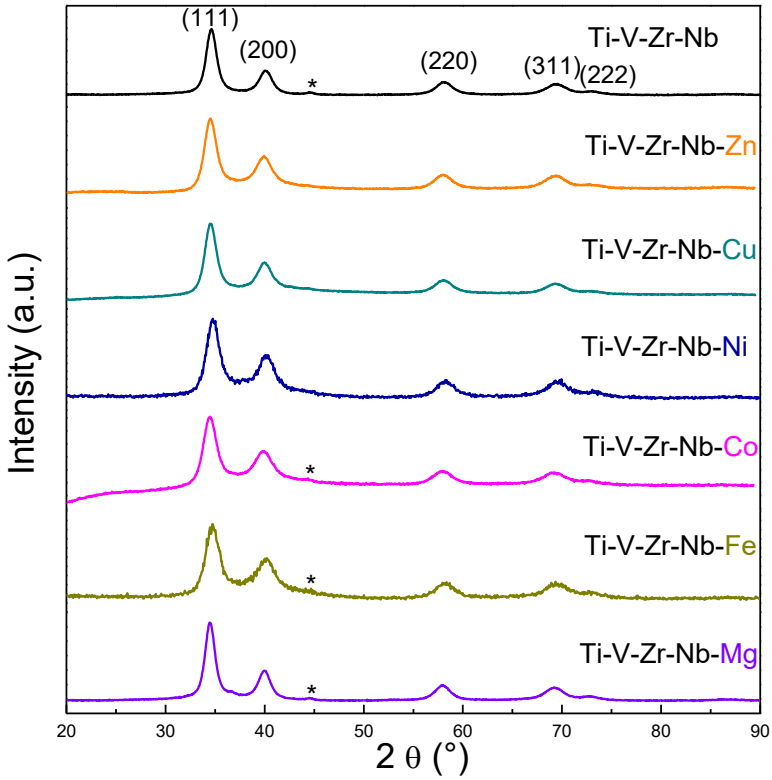

Figure 3.8. X-ray diffraction patterns (λ=1.5406 Å) of hydrides prepared by RBM of $Ti_{0.30}V_{0.25}Zr_{0.10}Nb_{0.25}M_{0.10}$ (with *M*= Co, Ni, Cu, and Zn) and the parent alloy $Ti_{0.325}V_{0.275}Zr_{0.125}Nb_{0.275}$.

Figure 3.8 shows the XRD of the synthesized hydrides following RBM synthesis for $Ti_{0.30}V_{0.25}Zr_{0.10}Nb_{0.25}M_{0.10}$ (with *M*= Mg, Fe, Co, Ni, Cu, and Zn) and the $Ti_{0.325}V_{0.275}Zr_{0.125}Nb_{0.275}$ alloy. All the samples crystallize in a single phase *fcc* lattice ($Fm\bar{3}m$). A small impurity (marked with *) is observed in the XRD patterns of the hydrides of $Ti_{0.30}V_{0.25}Zr_{0.10}Nb_{0.25}M_{0.10}$ (with *M*= Mg, Fe, and Co) and $Ti_{0.325}V_{0.275}Zr_{0.125}Nb_{0.275}$ at around 44°. This contamination was identified as pure Fe, which is obtained from the milling balls. The lattice parameter of the *fcc* phase for each hydride is listed in table 3.3.

Following the RBM synthesis, the microstructure and chemical composition of all the samples were analyzed by SEM and EDS (figure 3.9 (a-g)) (table 3.4).

$Ti_{0.325}V_{0.275}Zr_{0.125}Nb_{0.275}$

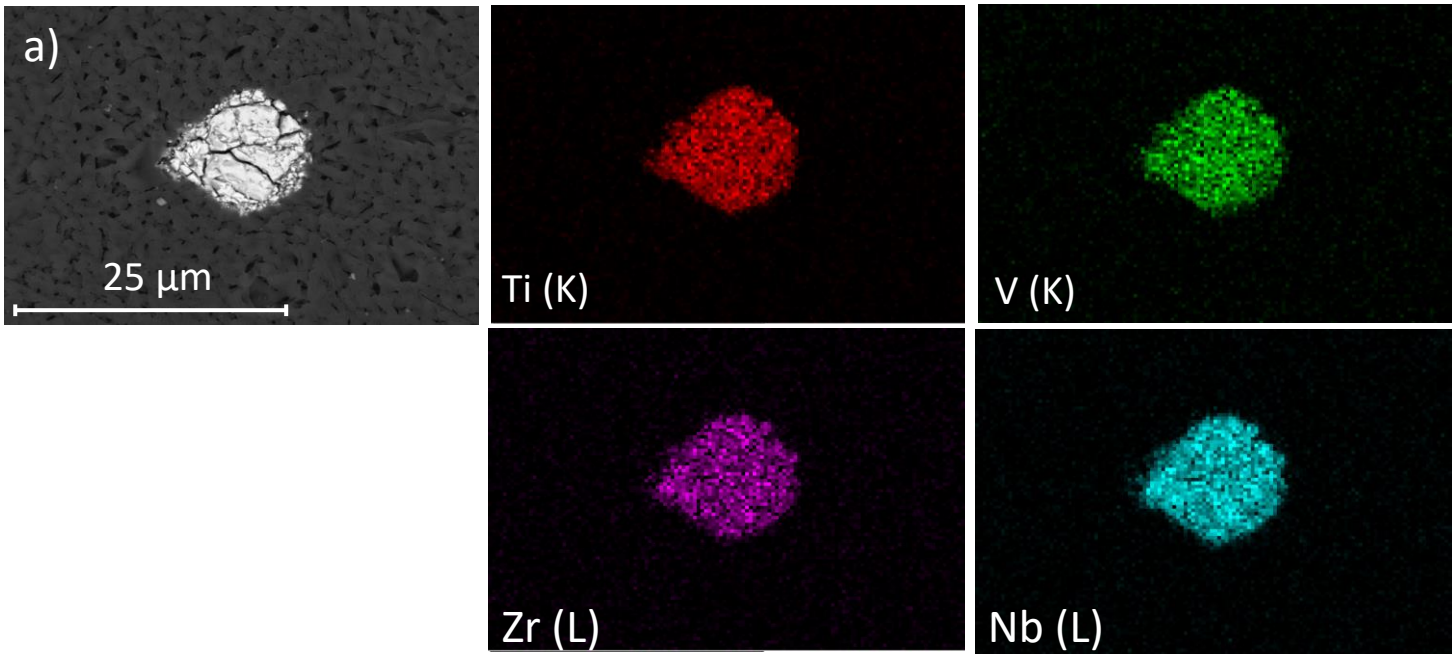

$Ti_{0.30}V_{0.25}Zn_{0.10}Zr_{0.10}Nb_{0.25}$

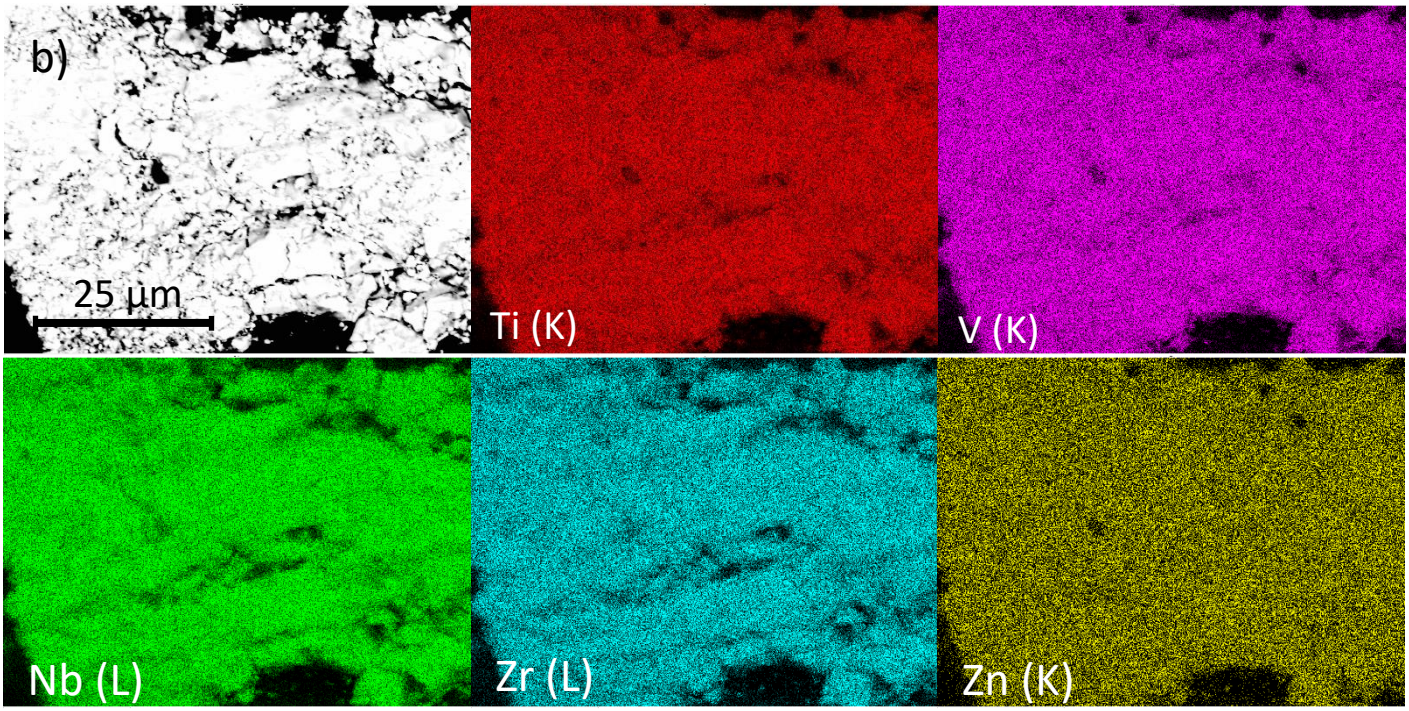

$Ti_{0.30}V_{0.25}Cu_{0.10}Zr_{0.10}Nb_{0.25}$

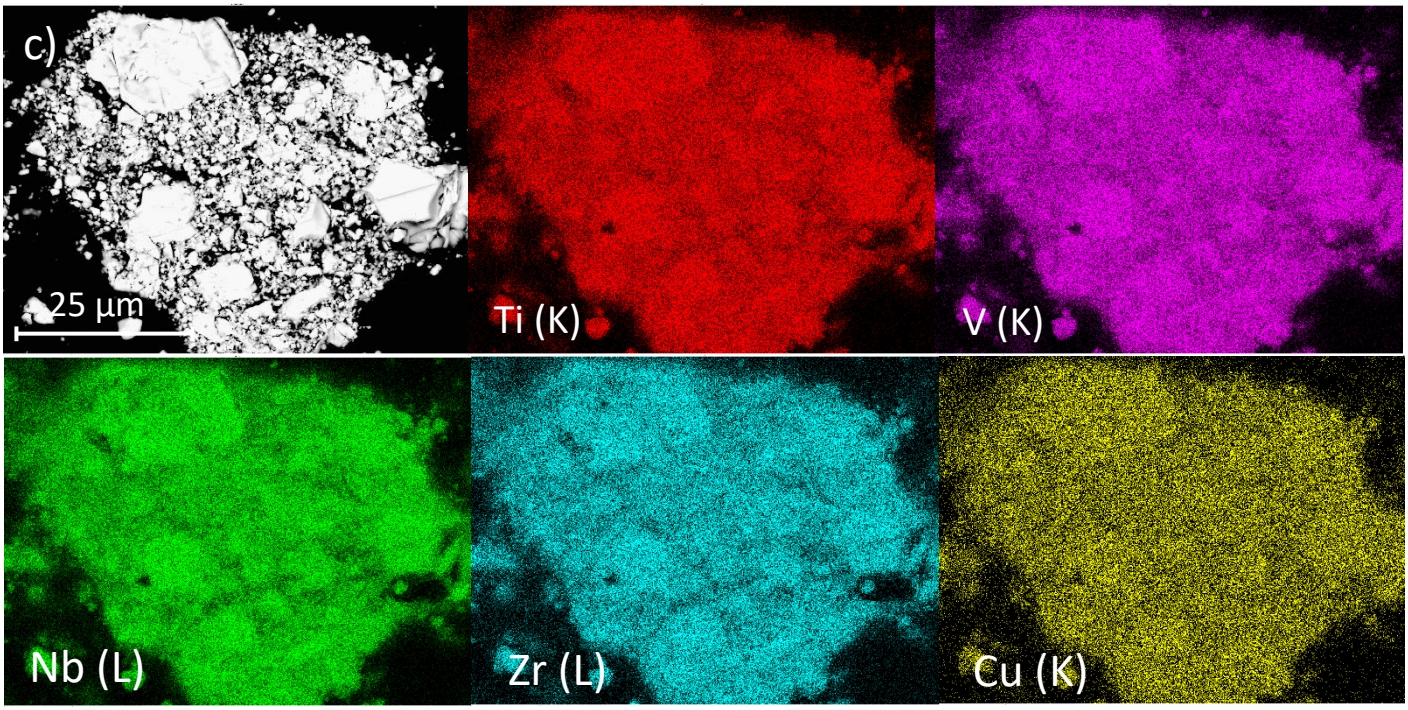

$Ti_{0.30}V_{0.25}Ni_{0.10}Zr_{0.10}Nb_{0.25}$

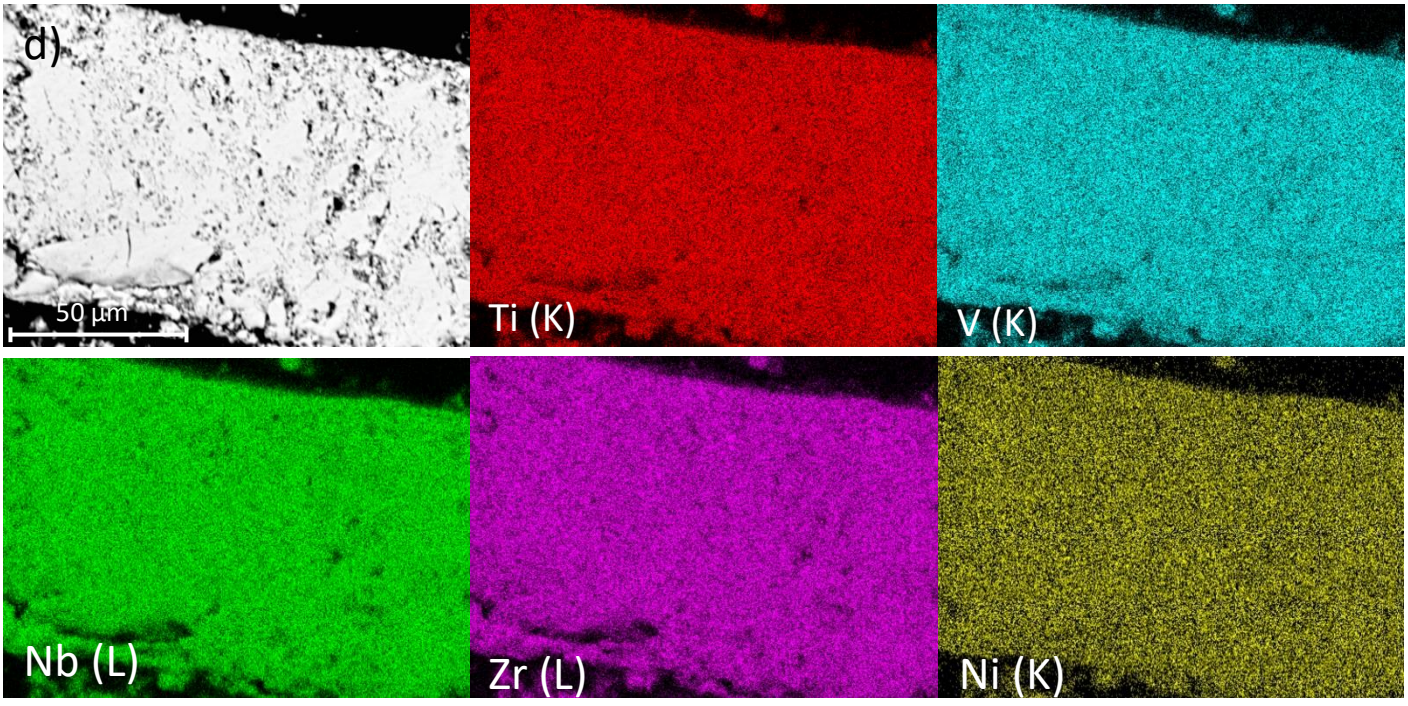

$Ti_{0.30}V_{0.25}Co_{0.10}Zr_{0.10}Nb_{0.25}$

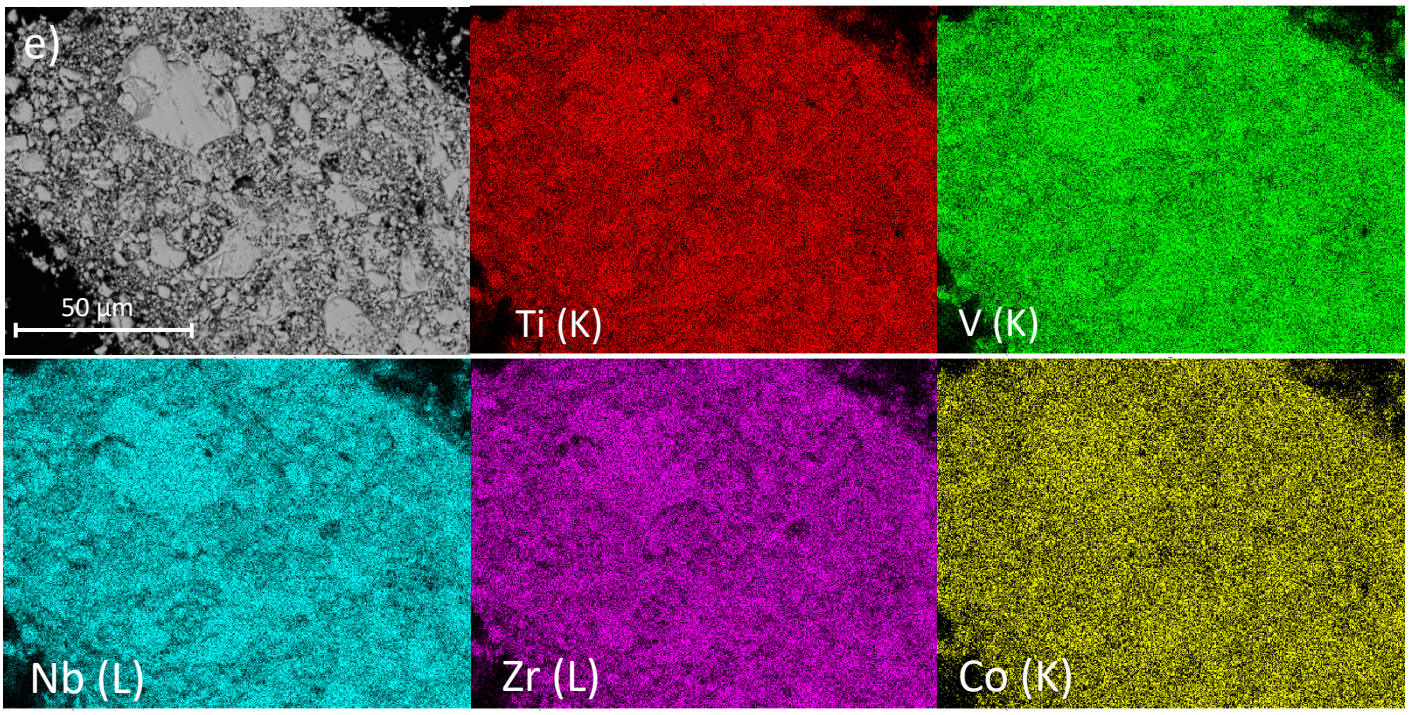

$Ti_{0.30}V_{0.25}Fe_{0.10}Zr_{0.10}Nb_{0.25}$

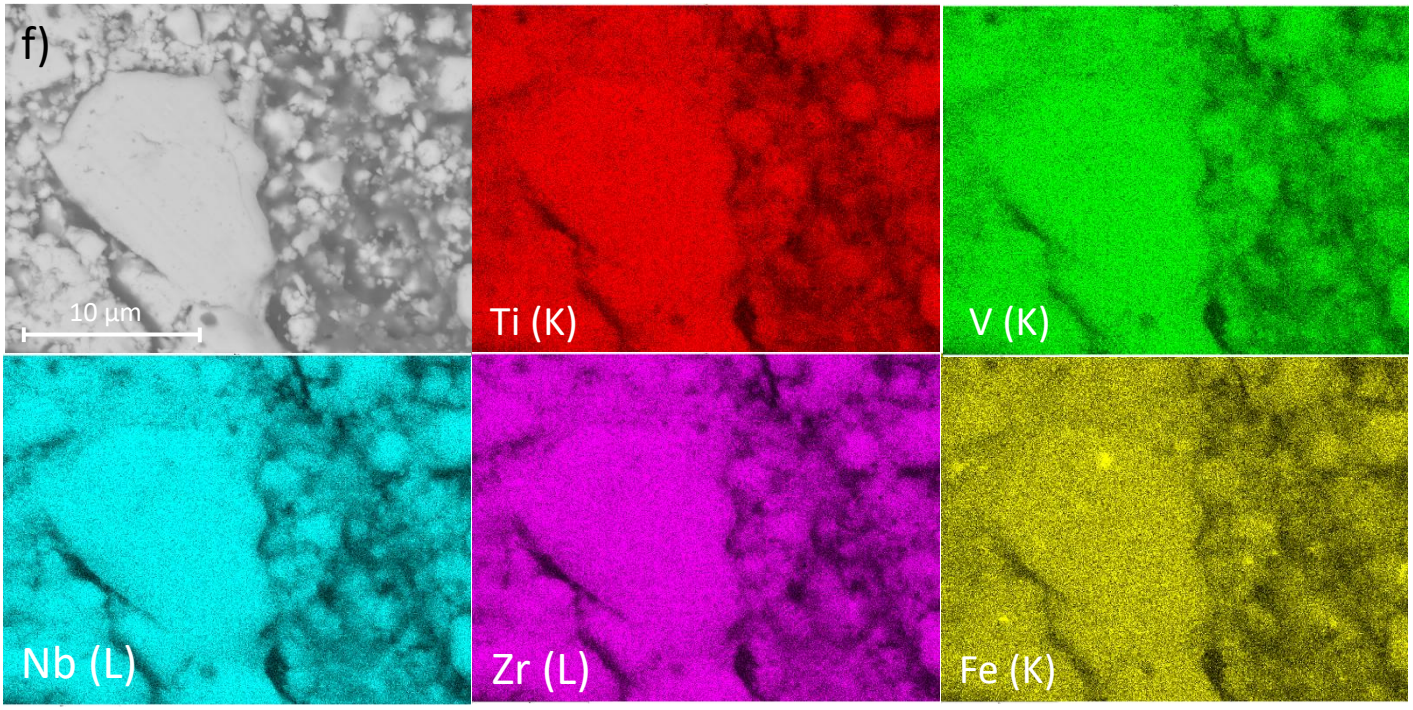

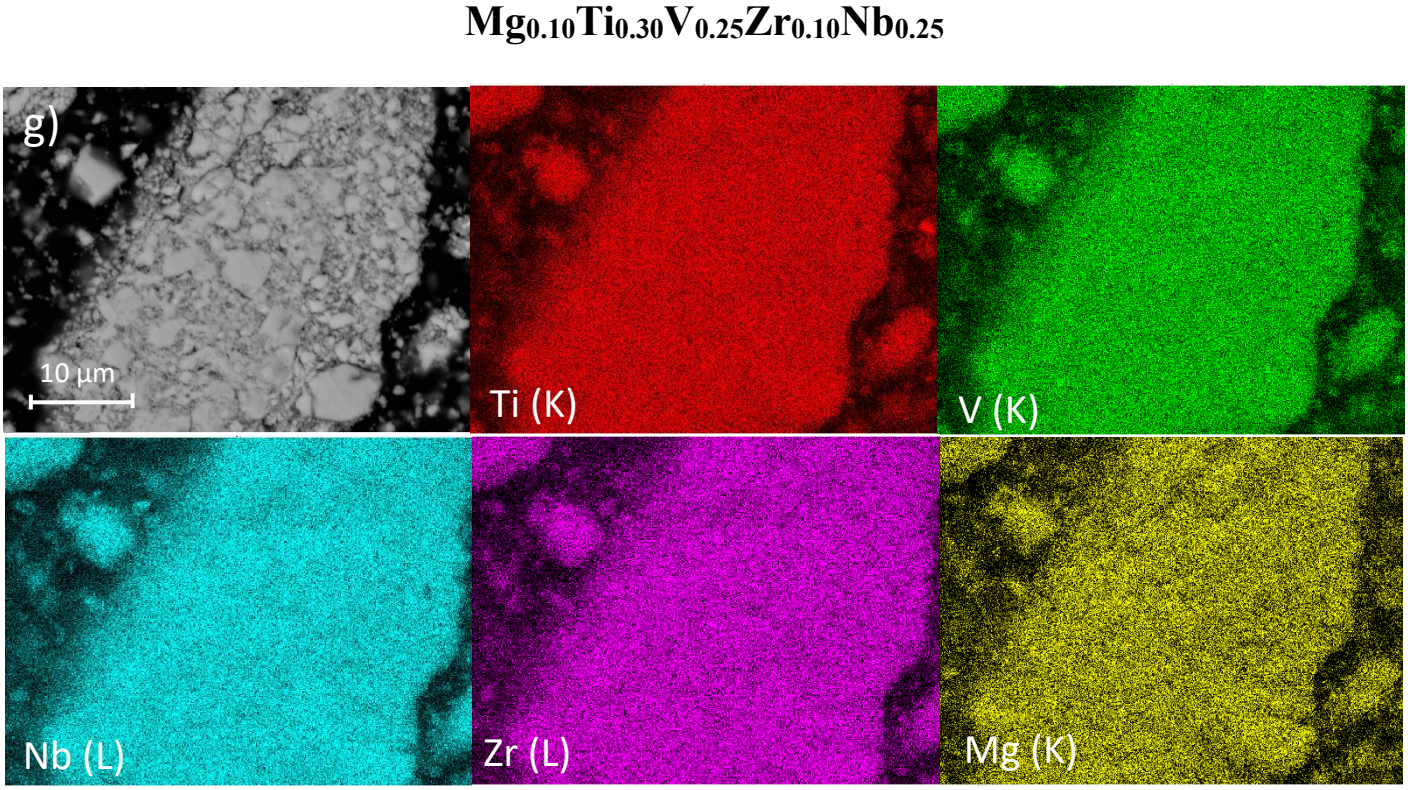

Figure 3.9. EDS chemical mapping of RBM hydrides samples: a) $Ti_{0.325}V_{0.275}Zr_{0.125}Nb_{0.275}$ and $Ti_{0.30}V_{0.25}Zr_{0.10}Nb_{0.25}M_{0.10}$ (*M*= Zn (b), Cu (c), Ni (d), Co (e), Fe (f) and Mg (g)).

Alloy *M*	**Ti (at.%)**	**V (at.%)**	**Zr (at.%)**	**Nb (at.%)**	**Zn (at.%)**	**Cu (at.%)**	**Ni (at.%)**	**Co (at.%)**	**Fe (at.%)**	**Mg (at.%)**
∅	32.04(0.2)	27.79(0.4)	12.01(0.2)	28.15(0.8)						
Zn	30.1(0.3)	24.7(0.6)	9.8(0.3)	25.5(0.6)	9.9(0.3)					
Cu	30.6(0.7)	25(0.6)	9.7(0.4)	25.3(0.6)		9.4(0.2)				
Ni	29.2(0.4)	24.1(0.7)	10.6(0.4)	26.8(1.2)			9.3(1.0)			
Co	29.9(0.7)	25.7(0.7)	9.6(0.5)	25.2(0.7)				9.6(0.4)		
Fe	30.1(1.0)	24.2(1.3)	9.4(0.4)	24.4(1.0)					11.9(1.0)	
Mg	29.9(0.5)	24.3(0.8)	9.8(0.4)	23.9(0.5)						12.1(0.5)

Table 3.4. Overall chemical composition of the overall values of the RBM hydrides $Ti_{0.325}V_{0.275}Zr_{0.125}Nb_{0.275}$ and $Ti_{0.30}V_{0.25}Zr_{0.10}Nb_{0.25}M_{0.10}$ (*M*= Zn, Cu, Ni, Co, Fe, and Mg).

The BSE images reveals a homogeneous microstructure for all the hydride samples and no secondary phase was observed. All the samples presented a good chemical homogeneity, and the atomic concentrations were near the nominal ones with low variations (<1.5 at.%). Nonetheless, a Fe contamination between 3 to 5% was detected in all the samples. The EDS chemical mapping of the RBM $Ti_{0.30}V_{0.25}Fe_{0.10}Zr_{0.10}Nb_{0.25}$ sample clearly shows the Fe contamination, as bright spots which were identified as pure Fe.

3.3 Hydrogenation properties

In this section PCI measurements are performed on one alloy synthesized *via* different methods. The purpose is to test if the capacity of hydrogen absorption of one composition is the same. At RT, PCI measurements were conducted on both BM and desorbed RBM samples of $Ti_{0.30}V_{0.25}Co_{0.10}Zr_{0.10}Nb_{0.25}$ (figure 3.10).

Prior to the PCI measurement, the RBM sample was loaded under Ar atmosphere into a stainless steel cell and desorbed at 400°C for 12h under dynamic vacuum and then cooled down to RT. Whereas the BM sample was loaded into a stainless steel cell and sealed under Ar atmosphere, to be activated at 350 °C for 3h which was followed by a cooling down to RT.

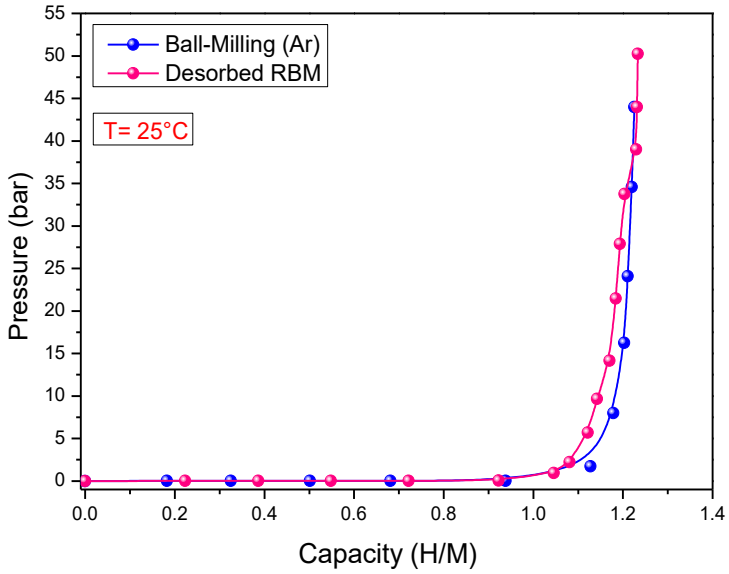

Figure 3.10. PCIs measurement at 25°C for both desorbed RBM and BM samples.

The PCIs measurements show the same results despite the use of samples synthesized by different methods (RBM and BM). Both samples rapidly absorbed hydrogen at room temperature and the PCIs of both samples show a plateau of absorption at low pressure (the equilibrium pressure is below the pressure transducer reading limit) followed by an ascendant branch at high pressure. The maximum capacity of hydrogen absorption was 1.23 H/M (1.8 wt.%), irrespective of the synthesis method.

The two PCI measurements prove that there is no difference between the use of BM or RBM samples, hence for the following sections, only the RBM samples will be desorbed and tested regarding their hydrogen sorption properties.

3.3.1 Pressure composition isotherms of the HEA series

In this section PCI measurements are conducted on both AM and RBM samples. Prior to the measurement, the AM samples were cut and loaded into a stainless steel cell under air and connected to a Sievert device for activation by heat treatment at 350°C for 3h under dynamic vacuum, followed by a cooling down to reach RT. The RBM samples were all loaded under Ar atmosphere into a stainless steel cell and desorbed by heat treatment at 400°C for 12h under dynamic vacuum and then cooled down to RT.

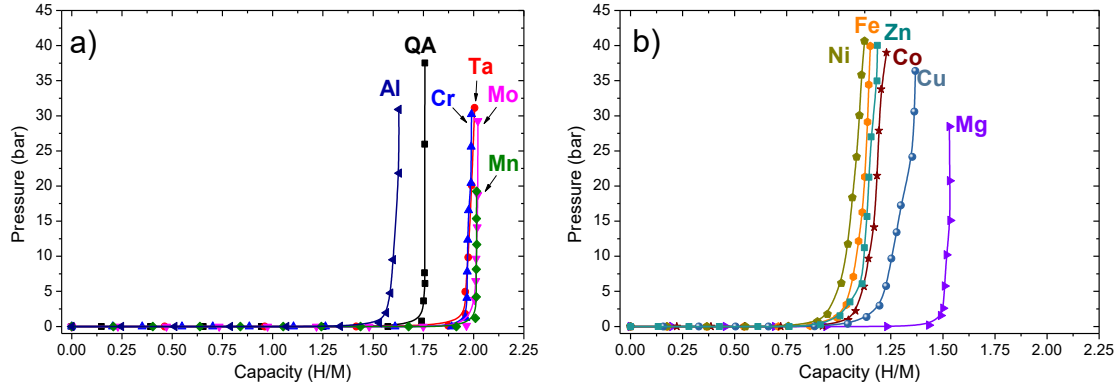

Figure 3.11. PCIs measurements at 25°C for arc melting (a) and desorbed RBM samples (b), (symbol for $Ti_{0.325}V_{0.275}Zr_{0.125}Nb_{0.275}$: QA).

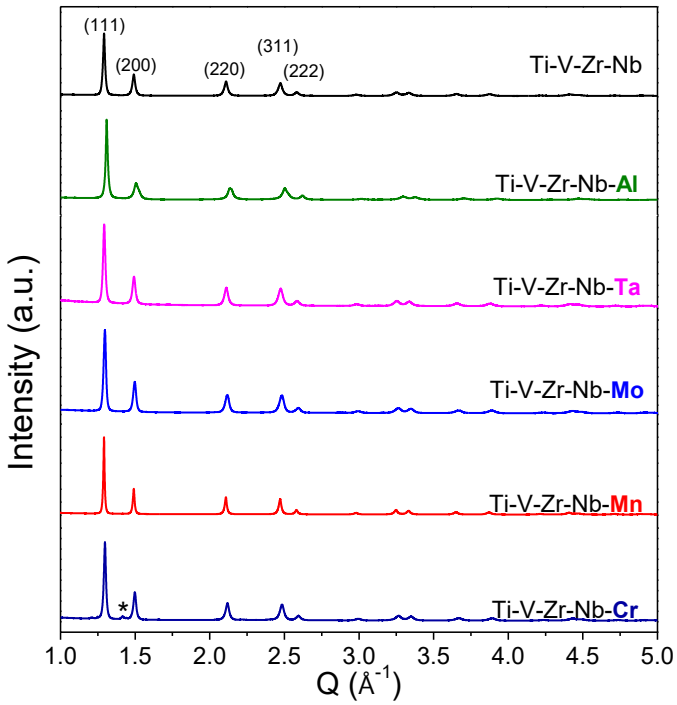

Figure 3.12. SR-XRD patterns of the hydrides of compositions prepared by arc melting.

All the PCIs of the $Ti_{0.30}V_{0.25}Zr_{0.10}Nb_{0.25}M_{0.10}$ (*M*= Mg, Al, Cr, Mn, Fe, Co, Ni, Cu, Zn, Mo, and Ta) and the quaternary alloy $Ti_{0.325}V_{0.275}Zr_{0.125}Nb_{0.275}$ are plotted in figure 3.11 a-b.

The AM and RBM samples rapidly absorbed hydrogen at 25°C. Furthermore, all the alloys showed similar PCI profiles (figure 3.11). A plateau of hydrogen absorption at low equilibrium pressure (pressure below the pressure transducer reading limit), followed by an ascendant branch at high pressure. The capacities of $Ti_{0.30}V_{0.25}Zr_{0.10}Nb_{0.25}M_{0.10}$ (*M*= Cr, Mn, Mo, and Ta) were equal to 2.0 H/M which is higher than the capacity of the parent alloy $Ti_{0.325}V_{0.275}Zr_{0.125}Nb_{0.275}$ (1.75 H/M). Alloys containing Mg, Al, Fe, Co, Ni, Cu, and Zn showed a decrease in the capacity ranging from 1.1 to 1.6 H/M (table 3.5). In terms of gravimetric capacities, the studied alloys containing Cr (3.0 wt.%)[5], Mn (2.98 wt.%)[6], Mo (2.8 wt.%)[7], Mg (2.7 wt.%)[3], Al (2.6 wt.%)[4], and Ta (2.5 wt.%)[8] presented higher capacities than classical intermetallics such as TiFe (1.89 wt.%)[16] and $LaNi_5$ (1.4 wt.%)[16], and HEAs like TiVNbTa (2 wt.%)[10] and TiZrNbHfTa (1.7 wt.%)[17].

Thesis work	*M*	Synthesis	δ(%)	VEC	Initial phase	a_{bcc} (Å)	Hydride phase	Hydride lattice parameter (Å)	Capacity (H/M)
J.Montero[2]	∅	AM			*bcc*	3.261 (1)	-	4.497 (1)	1.75
		BM	6.0	4.55	*bcc*	3.270 (1)	-	4.548 (1)	1.70
		RBM			-	-	*fcc*	4.474 (1)	1.80
J.Montero[3]	Mg	BM	6.6	4.3	*bcc*	3.273 (1)	-	-	-
		RBM				-	*fcc*	4.492 (1)	1.53
J.Montero[4]	Al	AM	5.5	4.4	*bcc*	3.247 (1)	*bct*	a_{bct}=3.137 (1) c_{bct}=4.374 (1)	1.60
Present[5]	Cr	AM	6.7	4.7	*bcc*	3.225 (1)	*fcc*	4.459 (1)	2.0
Present[6]	Mn	AM	5.7	4.8	*bcc*	3.239 (5)	*fcc*	4.482 (1)	2.0
Present	Fe	AM			*multiphase*	-	-	-	-
		BM	6.8	4.9	*bcc*	3.277 (1)	-	-	-
		RBM			-	-	*fcc*	4.505 (3)	1.16
Present	Co	AM			*multiphase*	-	-	-	-
		BM	6.7	5.0	*bcc*	3.299 (8)	-	-	-
		RBM			-	-	*fcc*	4.508 (3)	1.23
Present	Ni	AM			*multiphase*	-	-	-	-
		BM	6.7	5.1	*bcc*	3.296 (4)	-	-	-
		RBM			-	-	*fcc*	4.500 (3)	1.1
Present	Cu	AM			*multiphase*	-	-	-	-
		BM	6.4	5.2	*bcc*	3.278 (4)	-	-	-
		RBM			-	-	*fcc*	4.499 (1)	1.35
Present	Zn	BM	5.9	5.3	*bcc*	3.279 (3)	-	-	-
		RBM			-	-	*fcc*	4.506 (4)	1.18
Present[7]	Mo	AM	5.7	4.7	*bcc*	3.240 (3)	*fcc*	4.459 (1)	2.0
J.Montero[8]	Ta	AM	5.5	4.6	*bcc*	3.263 (3)	*fcc*	4.474 (1)	2.0

Table 3.5. The method of synthesis (arc melting (AM), ball milling under Ar (BM), and reactive ball milling (RBM)), the empirical parameters (δ and VEC), the initial formed phase structure and hydride phase with the corresponding lattice parameter and the capacity of absorption of the HEA series $Ti_{0.30}V_{0.25}Zr_{0.10}Nb_{0.25}M_{0.10}$ (with *M*= Mg, Al, Cr, Mn, Fe, Co, Ni, Cu, Zn, Mo, and Ta) and the parent alloy $Ti_{0.325}V_{0.275}Zr_{0.125}Nb_{0.275}$.

The XRD patterns of all the hydride samples obtained after PCI measurements are plotted in figure 3.12. A phase transition occurs following the hydrogen absorption from the initial *bcc* to a *fcc* hydride phase for most of the compositions. The Al-alloy experiences a phase transition from an initial *bcc* phase structure to a *bct* (I4/mmm) hydride phase (similar to the *fcc* structure but with a slight distorted lattice on the c axis). The Cr-hydride crystallizes in a *fcc* lattice with a small unidentified impurity which is in agreement with XRD of the as-cast alloy (figure 3.12 and figure 3.1). All the lattice parameters of the hydride phase are listed in table 3.5. Recently, an investigation by first principles calculations was conducted on the hydrogen storage properties of $Ti_{0.30}V_{0.25}Zr_{0.10}Nb_{0.25}Mg_{0.10}$ HEA [18]. In this study it was confirmed that during the hydrogenation process a phase transformation will occur from a *bcc* to a *fcc* dihydride phase. Moreover, the radial distribution function (RDF) is used to compare between the hydrogen-hydrogen pairs (H-H) in the *bcc* and *fcc* structures at high hydrogen content. The RDF showed that a *bcc* hydride with a hydrogen content of 1.25 H/M cannot physically form. This is due to the existence of an RDF peak of H-H bond at a short distance around 1.5 Å which results in violating the Switendick rule [19]. On the other hand, the *fcc* hydride phase is more stable energetically and allow the hydrogen to be accommodated at a distance satisfying the Switendick rule.

Furthermore, a comparison study of the effect of different methods of synthesis (AM, BM, and RBM) on the quaternary alloy $Ti_{0.325}V_{0.275}Zr_{0.125}Nb_{0.275}$ showed that the capacity of hydrogen absorption is independent of the method of synthesis [2]. Hence, the only influence on the hydrogen uptake is the composition of the alloy. Consequently, the measured capacities of hydrogen uptake of both AM and RBM samples can be compared and linked to the nature of the fifth added element *M* as the only variable affecting the hydrogen storage performances.

3.3.2 Correlation with empirical parameters

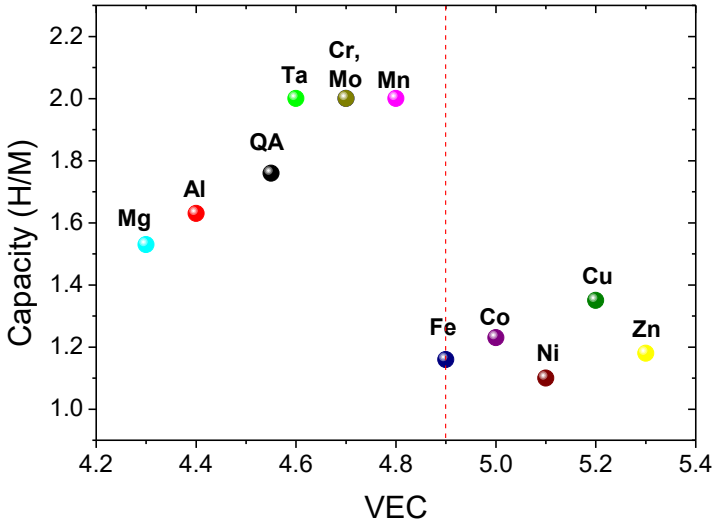

Figure 3.13. The storage capacity *vs.* VEC for the series $Ti_{0.30}V_{0.25}Zr_{0.10}Nb_{0.25}M_{0.10}$ (with *M*= Mg, Al, Cr, Mn, Fe, Co, Ni, Cu, Zn, Mo, and Ta) alloys and the parent alloy $Ti_{0.325}V_{0.275}Zr_{0.125}Nb_{0.275}$ alloy (QA).

Figure 3.13 illustrates the correlation between the hydrogen uptake which is expressed in H/M and the VEC. The effect of the added element *M* is highlighted in this figure, suggesting the existence of two regions. The first region (left) contains the first group with the highest absorption capacities. If VEC<4.9, the capacity ranges between 1.5 and 2.0 H/M. Whereas, the second region (where VEC ≥ 4.9), the hydrogen uptake decreased drastically from 2.0 H/M to capacities between 1.1 and 1.35 H/M.

The plot against the VEC expresses the importance of the added element. In this case, a hypothesis can be made:

The capacity decreases when the added element is a late *3d* transition metal as illustrated in the following electronic configurations of Fe, Co, Ni, Cu, and Zn:

Fe: [Ar] $3d^6\ 4s^2$

Co: [Ar] $3d^7\ 4s^2$

Ni: [Ar] $3d^8\ 4s^2$

Cu: [Ar] $3d^{10}\ 4s^1$

Zn: [Ar] $3d^{10}\ 4s^2$

The more the valence shell is filled, the more the possibility of hydrogen bonding with the alloy decreases, resulting in a loss of the storage capacity. The relationship between the added element and its effect on the hydrogen storage capacity could be explained as follows:

The addition of *3d* late transition elements increases the value of VEC and simultaneously fills the unoccupied valence states. In the counterpart, in the simplest rigid band model, the hydrogen atom donates its only electron to the vacant electronic state in the conduction band. However, in the present case, alloying with *3d* elements will decrease the available vacant electronic states leaving no possible donation of the hydrogen's electron. The result of the addition of *3d* transition metals will increase the electronic repulsion between hydrogen atoms and the HEA. Consequently, the hydrogen absorption capacity of the alloy will be decreased if the VEC is increased higher than 4.9. Moreover, Lynch et al. confirmed the latter statement experimentally by investigating the effect of substituting Cr for V regarding hydrogen sorption properties [20]. Furthermore, Lynch et al. and Kagawa et al. stated if the electron per atom ratio (e/a) of both V-Cr and V-Ti alloys increases higher than 5.0, a drastic decrease of the hydrogen absorption capacity will occur [20,21].

A similar trend was reported by Nygård et al. when investigating a different HEA series [10], suggesting another trend relating the relative volume expansion against the VEC:

$$\alpha = \left[\left(\left({}^{V}/_{Z}\right)_{fcc} - \left({}^{V}/_{Z}\right)_{bcc}\right)\right] / \left({}^{V}/_{Z}\right)_{bcc}$$

Where $\left({}^{V}/_{Z}\right)_{fcc}$ and $\left({}^{V}/_{Z}\right)_{bcc}$ are the volumes per metal atom of the *fcc* and *bcc* lattices, respectively. In studies reported by Nygård et al. and Ek et al. [10,22], a correlation was drawn between the relative volume expansion (α) and VEC by showing a linear increasing trend with the VEC. This suggests that hydrogen is causing a constant volume expansion.

In the present work (figure 3.14), the hydrides present a relative volume expansion scattered between 0.25 and 0.32 with an average of 0.29. However, no clear trend can be drawn between α and VEC. Nevertheless, if only the AM materials are considered (data within the blue dotted square (figure 3.14)) a clear trend arises, which is close to the trends that are reported by Nygård et al. and Ek et al. [10,22]. Moreover, the volume expansion following the hydride formation is in the same range irrespective of the method of synthesis, the hydrogen absorption capacity, and the chemical composition of the alloys.

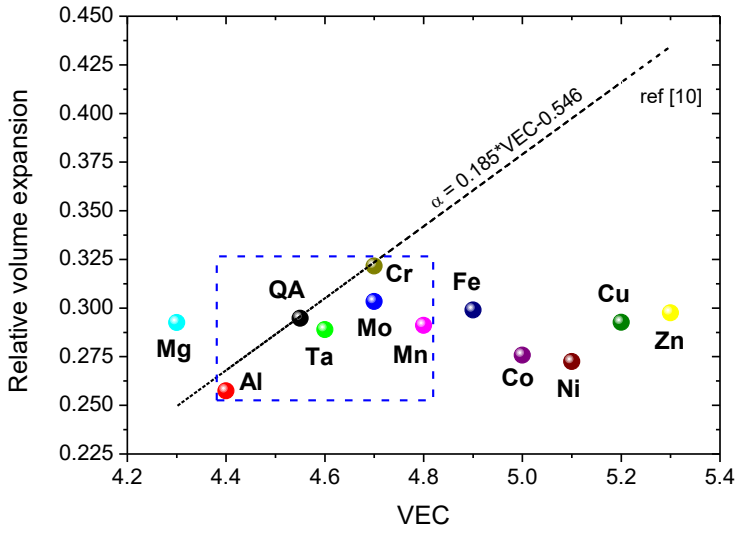

Figure 3.14. The relative volume expansion *vs.* VEC for the series $Ti_{0.30}V_{0.25}Zr_{0.10}Nb_{0.25}M_{0.10}$ (with *M*= Mg, Al, Cr, Mn, Fe, Co, Ni, Cu, Zn, Mo, and Ta) alloys and the parent alloy $Ti_{0.325}V_{0.275}Zr_{0.125}Nb_{0.275}$ alloy (QA), blue dotted square indicating the AM materials, a dotted black line is shown representing the linear correlation proposed by Nygård et al. [10].

Following the volume expansion resulting from the hydrogenation process, it is also interesting to study the volume of the interstitial hydrogen atoms within the lattices of the hydrides. The volume of interstitial hydrogen atoms is obtained by dividing the cell volume expansion per metal atom by the hydrogen absorption capacity (H/M).

Figure 3.15 illustrates an attempt for a correlation between the volume of intestinal hydrogen atoms within the lattices of the materials against the VEC. The plotted data could be divided into two regions depending on the value of the VEC (as seen in figure 3.13): for VEC<4.9, the volume of interstitial hydrogen is in the range of 2.5 to 3.2 $Å^3$ and the average volume is 2.7 (2) $Å^3$. Interestingly, Peisl et al. proposed that the volume of interstitial hydrogen in several metals and alloys is 2.9 $Å^3$ which is close to the average calculated value of the present work [23]. The second region, when VEC≥4.9 presents higher values ranging from 3.8 to 4.7 $Å^3$, suggesting that the hydrogen atoms are occupying larger average volumes when hydrides contain late *3d* transition elements Fe, Co, Ni, Cu, and Zn, this results in a less attractive interaction between hydrogen and metal atoms, contrary to early *3d* metals.

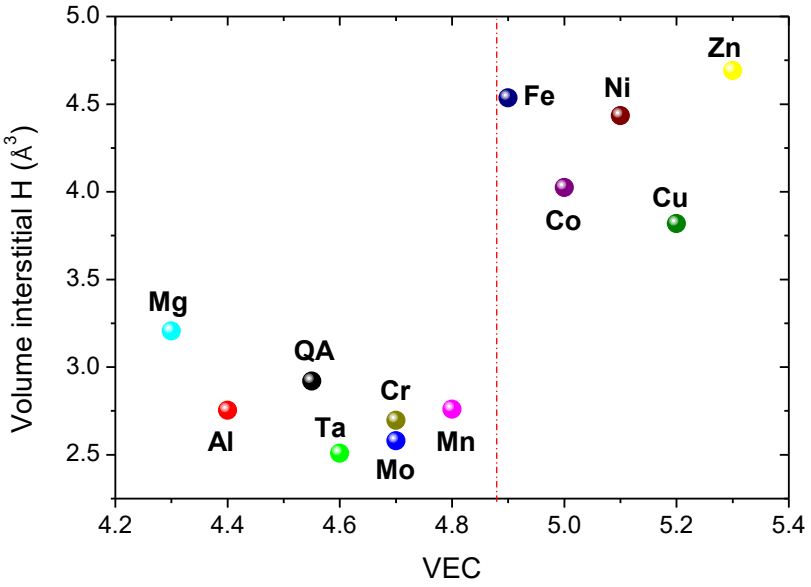

Figure 3.15. The volume of interstitial hydrogen *vs.* VEC for the series $Ti_{0.30}V_{0.25}Zr_{0.10}Nb_{0.25}M_{0.10}$ (with *M*= Mg, Al, Cr, Mn, Fe, Co, Ni, Cu, Zn, Mo, and Ta) alloys and the parent alloy $Ti_{0.325}V_{0.275}Zr_{0.125}Nb_{0.275}$ alloy (QA).

3.3.3 Hydride characterization: Pair distribution function

HEAs have a lattice that is distorted on the local level because of the random occupation of crystallographic sites by different types of atoms which have different sizes. An investigation of the local structure was conducted in the series $Ti_{0.30}V_{0.25}Zr_{0.10}Nb_{0.25}M_{0.10}$ (with *M*= Mo, Mn, Cr, Al, and Mg) and $Ti_{0.325}V_{0.275}Zr_{0.125}Nb_{0.275}$ hydrides at short and medium range orders. The analysis was carried out using SR-X-ray total scattering and related PDF analysis using the G(R) formalism.

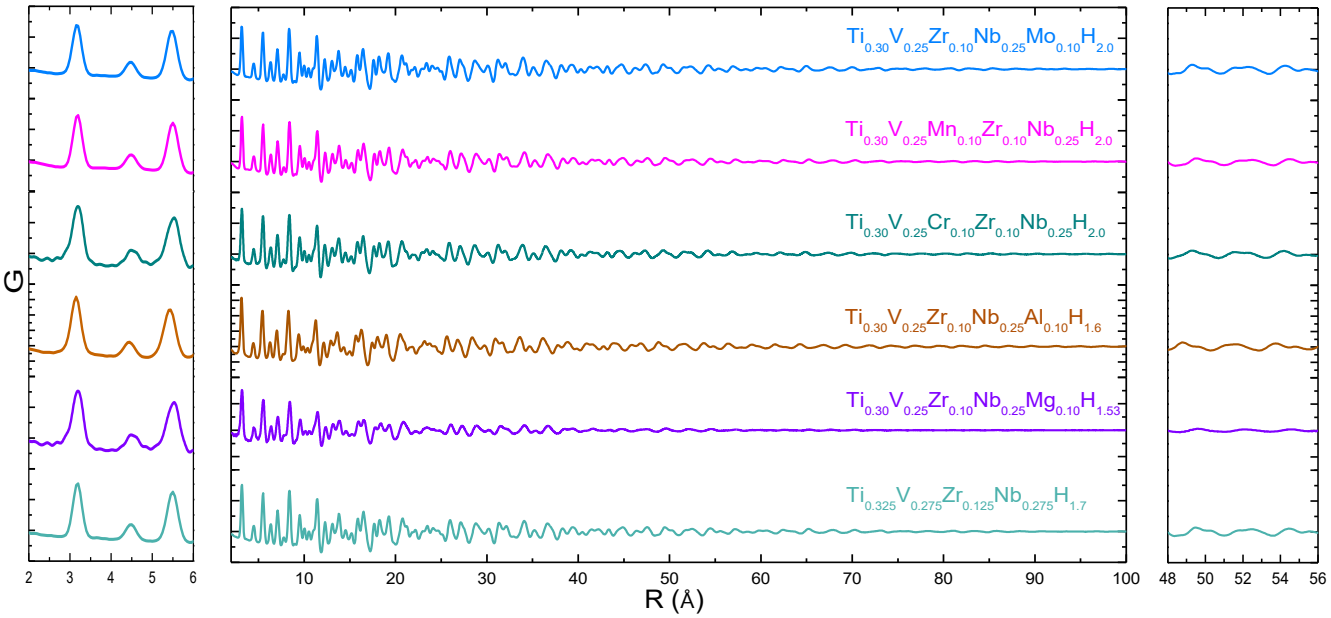

Figure 3.16. The PDF patterns at short-range (left), the whole R range (middle), and the long-range (right) regions of the series $Ti_{0.30}V_{0.25}Zr_{0.10}Nb_{0.25}M_{0.10}$ (with *M*= Mo, Mn, Cr, Al, and Mg) and $Ti_{0.325}V_{0.275}Zr_{0.125}Nb_{0.275}$ hydrides at ambient conditions obtained by high-energy X-ray diffraction.

In figure 3.16, the PDF profiles are compared over a wide-R range to illustrate how the profile evolves for the series of $Ti_{0.30}V_{0.25}Zr_{0.10}Nb_{0.25}M_{0.10}$ (with *M*= Mo, Mn, Cr, Al, and Mg) and $Ti_{0.325}V_{0.275}Zr_{0.125}Nb_{0.275}$ hydrides. All the profiles are similar suggesting a close local order despite the different chemical compositions. Interestingly, at low R-range (figure 3.16 (right)), all the profiles are similar. However, at high R-range (48-56 Å), a broadening of the profile peaks of Mg containing hydride was observed displaying a loss of structural correlation because of the ball milling synthesis.

To further analyze these profiles, a refinement was applied using an average *fcc* or *bct* lattice depending on the hydride phase, with a random distribution of metallic atoms (figure 3.17 and table 3.6).

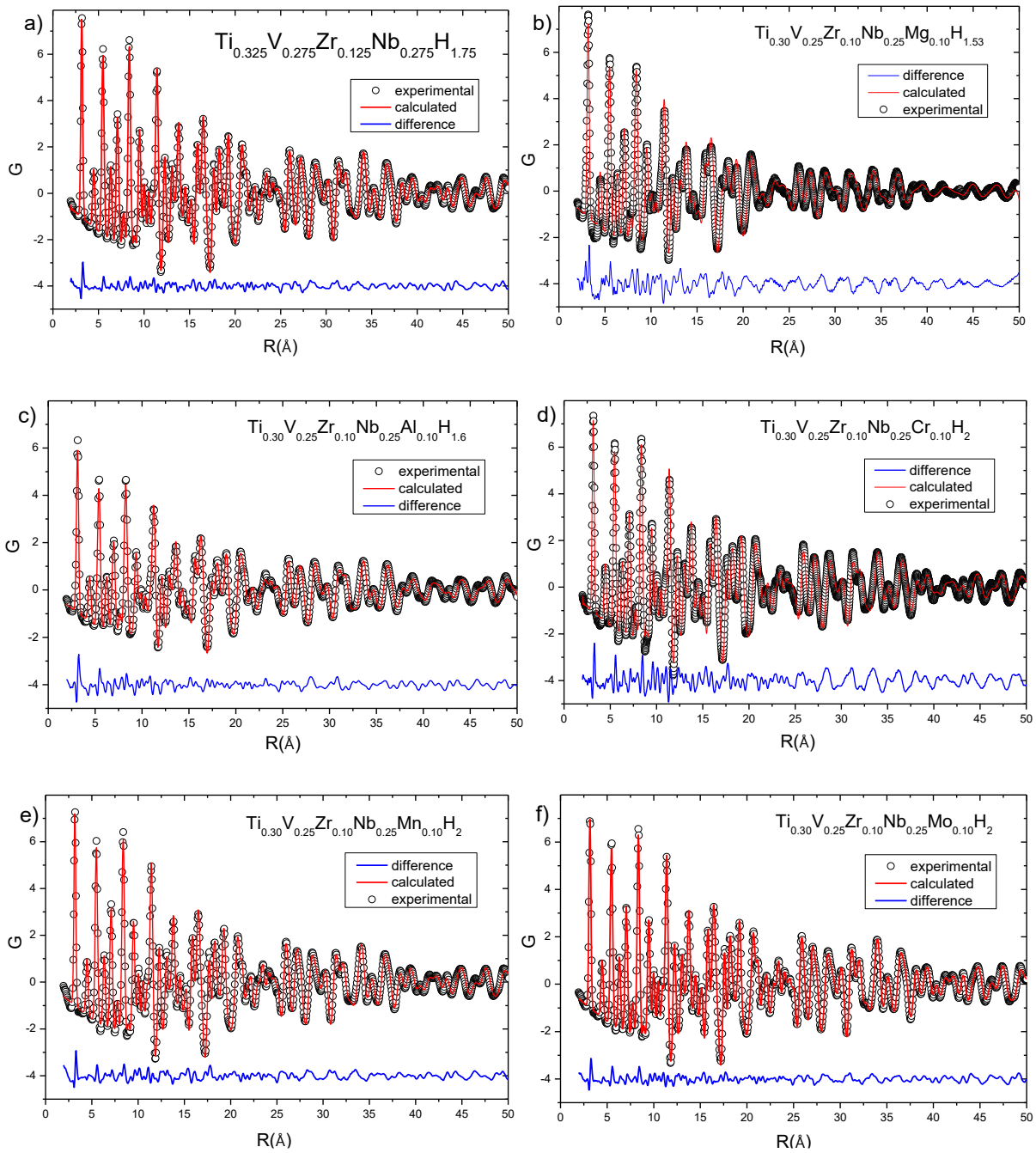

Figure 3.17. PDF refinements for the series $Ti_{0.30}V_{0.25}Zr_{0.10}Nb_{0.25}M_{0.10}$ (with *M*= (f) Mo, (e) Mn, (d) Cr, (c) Al, and (b) Mg) and (a) $Ti_{0.325}V_{0.275}Zr_{0.125}Nb_{0.275}$ hydrides and the corresponding refinement based on *fcc* and *bct* random structures.

Hydride	structure	Lattice parameter a/c (Å)		U_{iso} (Å^2)	Q_{broad}	χ^2	R_w
$Ti_{0.325}V_{0.275}Zr_{0.125}Nb_{0.275}H_{1.70}$	*fcc*	4.482 (1)		0.009 (1)	0.056 (5)	0.017	0.098
$Mg_{0.10}Ti_{0.30}V_{0.25}Zr_{0.10}Nb_{0.25}H_{1.53}$	*fcc*	4.492 (1)		0.011 (1)	0.085 (4)	0.065	0.23
$Al_{0.10}Ti_{0.30}V_{0.25}Zr_{0.10}Nb_{0.25}H_{1.60}$	*bct*	3.140 (3)	4.369 (8)	0.013 (2)	0.046 (7)	0.028	0.167
$Ti_{0.30}V_{0.25}Cr_{0.10}Zr_{0.10}Nb_{0.25}H_{2.0}$	*fcc*	4.465 (1)		0.009 (1)	0.064 (2)	0.079	0.22
$Ti_{0.30}V_{0.25}Mn_{0.10}Zr_{0.10}Nb_{0.25}H_{2.0}$	*fcc*	4.485 (1)		0.009 (1)	0.060 (5)	0.012	0.126
$Ti_{0.30}V_{0.25}Zr_{0.10}Nb_{0.25}$ $Mo_{0.10}H_{2.0}$	*fcc*	4.467 (1)		0.009 (1)	0.051 (4)	0.017	0.10

Table 3.6. The structure, lattice parameters, isotropic atomic displacement parameter (U_{iso}), Q_{broad}, χ^2, and R_w obtained from the PDF refinement of $Ti_{0.30}V_{0.25}Zr_{0.10}Nb_{0.25}M_{0.10}$ (with *M*= Mo, Mn, Cr, Al, and Mg) and $Ti_{0.325}V_{0.275}Zr_{0.125}Nb_{0.275}$ hydrides.

For the series $Ti_{0.30}V_{0.25}Zr_{0.10}Nb_{0.25}M_{0.10}$ (with *M*= Mo, Mn, Cr, and Mg) and $Ti_{0.325}V_{0.275}Zr_{0.125}Nb_{0.275}$ hydrides, the modelling of the hydride phase was carried out using a *fcc* lattice with random distribution of all atoms on the crystallographic sites. Whereas, for $Al_{0.10}Ti_{0.30}V_{0.25}Zr_{0.10}Nb_{0.25}H_{1.60}$ hydride, the modelling was based on a *bct* lattice with random distribution of all atoms on the crystallographic sites. For the sake of comparison, the PDF refinement and the related structural fit are compared to the quaternary hydride (figure 3.17 and table 3.6). The difference curves (figure 3.17) between experimental and refined PDF suggest that the undistorted random *fcc* and *bct* models can well describe the local structure in the low and high R regions. Previous reports revealed that the presence of large elements such as Zr and Hf can often increase deviations from average structure at short range for R<4 Å [24,25]. However, the studied series of HEAs contain a small content of Zr with a concentration of 10 at.% or 12.5 at.% for quinary and quaternary parent alloy, respectively.

The refined lattice parameters are close to the ones found from previous refinements of SR-XRD (table 3.6 and table 3.5). Interestingly, the parameter Q_{broad} is linked to the broadening due to instrument resolution but also defects and dislocations present in the alloy [26].

In table 3.6, the Q_{broad} parameter indicated a high value for $Mg_{0.10}Ti_{0.30}V_{0.25}Zr_{0.10}Nb_{0.25}H_{1.53}$ hydride sample, this suggests that the sample that is synthesized *via* RBM suffers from structural defects. Consequently, when comparing the R_w of all the refinements, the R_w of the $Mg_{0.10}Ti_{0.30}V_{0.25}Zr_{0.10}Nb_{0.25}H_{1.53}$ hydride is higher than the rest of the other hydrides. This is due to the influence of the Q_{broad} parameter on the refinement [26]. Nevertheless, the PDF investigation showed that the HEA hydrides have very similar profiles suggesting the same local order.

3.4 Desorption properties: Thermo-desorption-spectroscopy

The desorption properties of all the hydrides have been investigated by thermo-desorption-spectroscopy. All the hydride samples were subjected to a heating from 25°C to 450°C with a constant heating rate of 1°/min, where the evolved gas was measured.

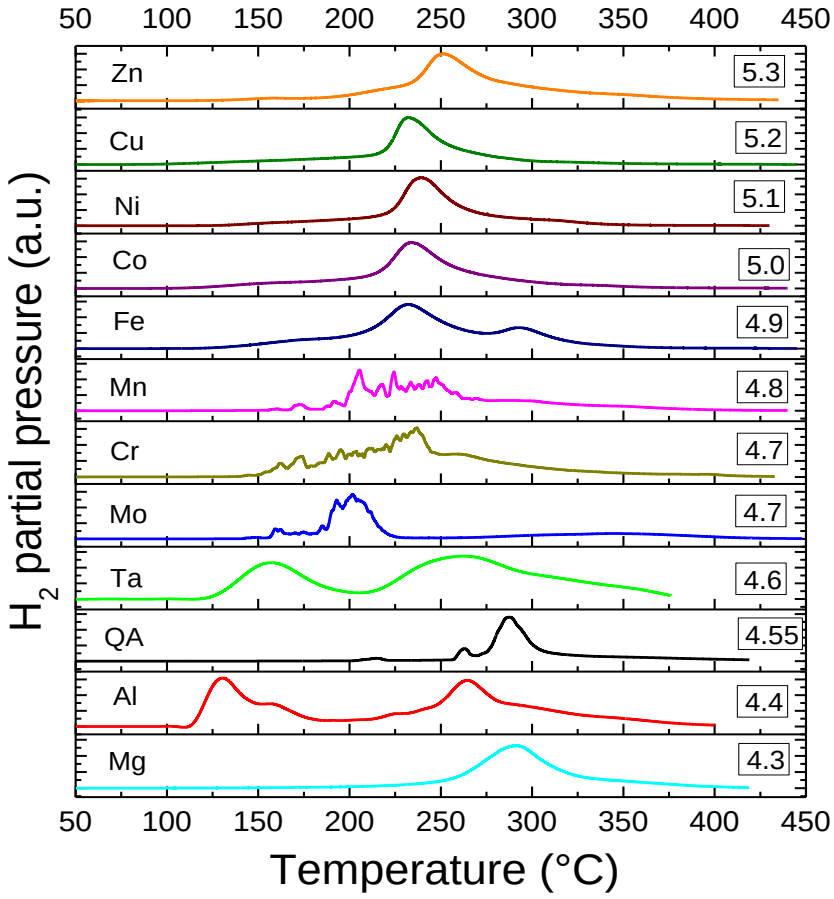

Figure 3.18. The thermo-desorption spectroscopy profiles of the series $Ti_{0.30}V_{0.25}Zr_{0.10}Nb_{0.25}M_{0.10}$ (with *M*= Mg, Al, Cr, Mn, Fe, Co, Ni, Cu, Zn, Mo, and Ta) alloys and the parent alloy $Ti_{0.325}V_{0.275}Zr_{0.125}Nb_{0.275}$ alloy (QA). The profiles are plotted as a function of increasing VEC.

Figure 3.18 illustrates the TDS profiles of all the studied hydrides. A difference between each plot is observed, which strongly depends on the nature of the fifth added element *M*. The influence of the added element is regarding the number of events, the value of the T_{onset}, and the value of T_{max} of the main peak. The profiles of the desorption are composed essentially of one main event, with only two exceptions of the Al and Ta containing hydrides which have two main events of desorption [4,8]. Moreover, the latter hydrides presented the lowest T_{onset} from all the measured desorption profiles. In addition, the T_{max} of most of the hydrides was inferior

than the T_{max} of the parent alloy, especially for Al and Ta containing hydrides. Whereas for the Mg containing hydride, the T_{max} increased.

Thesis work	*M*	Synthesis	δ(%)	VEC	T_{onset} (°C)
J.Montero[2]	Ø	AM			271
		BM	6.0	4.55	-
		RBM			-
J.Montero[3]	Mg	BM	6.6	4.3	251
		RBM			-
J.Montero[4]	Al	AM	5.5	4.4	114
Present[5]	Cr	AM	6.7	4.7	145
Present[6]	Mn	AM	5.7	4.8	195
Present	Fe	AM			-
		BM	6.8	4.9	-
		RBM			199
Present	Co	AM			-
		BM	6.7	5.0	-
		RBM			209
Present	Ni	AM			-
		BM	6.7	5.1	-
		RBM			218
Present	Cu	AM			-
		BM	6.4	5.2	-
		RBM			217
Present	Zn	BM	5.9	5.3	-
		RBM			228
Present[7]	Mo	AM	5.7	4.7	188
J.Montero[8]	Ta	AM	5.5	4.6	125

Table 3.7. The method of synthesis (arc melting (AM), ball milling under Ar (BM), and reactive ball milling (RBM)), the empirical parameters (δ and VEC), and the onset temperature of desorption of the HEA series $Ti_{0.30}V_{0.25}Zr_{0.10}Nb_{0.25}M_{0.10}$ (with *M*= Mg, Al, Cr, Mn, Fe, Co, Ni, Cu, Zn, Mo, and Ta) and the parent alloy $Ti_{0.325}V_{0.275}Zr_{0.125}Nb_{0.275}$.

3.4.1 Correlation with empirical parameters

Following the addition of all the elements *M* to the quaternary alloy $Ti_{0.325}V_{0.275}Zr_{0.125}Nb_{0.275}$ the value of the T_{onset} decreased, as demonstrated in table 3.7 and figure 3.19. A correlation is drawn between the onset temperature of the main peak of desorption and the VEC as illustrated in figure 3.19. With the exception of the T_{onset} of the parent alloy $Ti_{0.325}V_{0.275}Zr_{0.125}Nb_{0.275}$ and the Mg containing alloy, the T_{onset} values of the alloys are increasing linearly with the VEC.

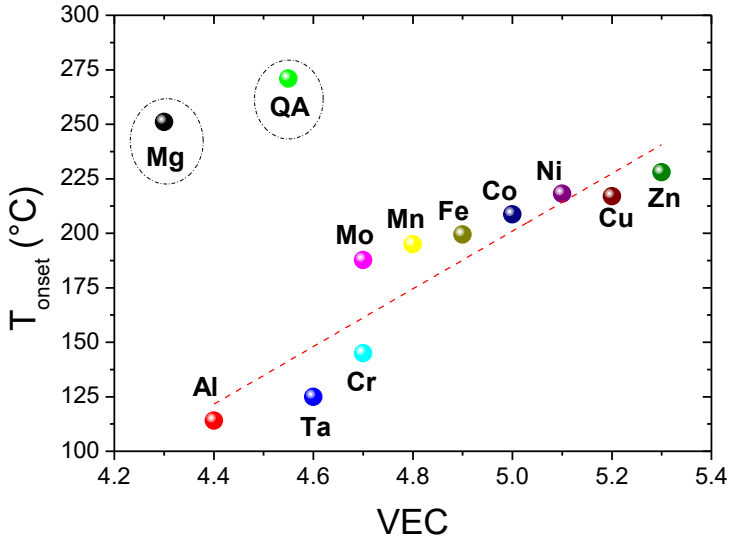

Figure 3.19. The onset temperature of desorption *vs.* VEC of the HEA series $Ti_{0.30}V_{0.25}Zr_{0.10}Nb_{0.25}M_{0.10}$ (with *M*= Mg, Al, Cr, Mn, Fe, Co, Ni, Cu, Zn, Mo, and Ta) and the parent alloy $Ti_{0.325}V_{0.275}Zr_{0.125}Nb_{0.275}$.

The lowest desorption temperature is obtained for Al and Ta containing alloys. Hence, having a low VEC is beneficial for low onset temperature. This is in a good agreement with the previous drawn correlation in figure 3.13 (capacity of absorption *vs.* VEC). The best candidate to have the highest capacity of absorption and the lowest desorption temperature should have a VEC<4.9.

Nevertheless, Nygård et al. and Ek et al. have also drawn a correlation between the T_{onset} and the VEC [10,22]. However, the trend was decreasing linearly with increasing of the VEC. The various reasons for the incompatibility of the two trends are:

-The difference in the thermal analysis experiment conditions and the measurement techniques:

the TDS under high vacuum for the present case against the DSC under atmospheric pressure for the literature report.

-The difference in the studied series, which is for the present work a variation only by 10 at.% of a quaternary alloy, whereas for the other reports it is a mix of ternary, quaternary, and quinary alloys containing essentially refractory elements (Ti, V, Cr, Zr, Nb, Mo, Hf, and Ta).

Therefore, a comparison could not be accurate enough to develop a scientific criticism regarding the correlation that is based on the same parameters.

In this chapter, it has been confirmed that for a precise construction of correlations, one should limit the variations of the chemical composition such as the number of elements and the concentration of the constituent elements of the composition.

3.5 Conclusions

In the present chapter, we proposed a novel methodology to elucidate the compositional effect on the hydrogen sorption properties of a series of HEAs. The investigated series of HEAs is based on adding a fifth element *M* (with *M*= Mg, Al, Cr, Mn, Fe, Co, Ni, Cu, Zn, Mo, and Ta) with a fixed concentration of 10 at.% to a quaternary alloy $Ti_{0.325}V_{0.275}Zr_{0.125}Nb_{0.275}$.

The HEA series $Ti_{0.30}V_{0.25}Zr_{0.10}Nb_{0.25}M_{0.10}$ was synthesized *via* different methods for the purpose of obtaining the same initial single phase *bcc*. Following this, a weak correlation was drawn between the *bcc* lattice parameter with the lattice distortion (δ). The SEM-EDS analysis suggests the formation of homogenous chemical distribution for BM alloys, whereas AM method gave rise to dendritic/interdendritic regions in the samples.

Succeeding the synthesis, the hydrogen absorption properties were studied by PCI measurements at room temperature. The PCI curves presented the same profile with one unique absorption plateau at low pressure. A phase transition from the initial *bcc* phase to a hydride phase which was *fcc* for most of the hydrides with one exception of the Al-containing hydride adopting a *bct* type structure. The hydrogenation process resulted in the emergence of many correlations such as the hydrogen absorption capacity *vs.* VEC, the relative volume expansion *vs.* VEC, and the volume interstitial of H *vs.* VEC. It is shown that the hydrogen storage capacity is strongly depending on the value of VEC.

The local structure of the full hydride phases was studied *via* pair distribution function for the purpose of investigating the difference between the different compositions and to compare them to the parent alloy $Ti_{0.325}V_{0.275}Zr_{0.125}Nb_{0.275}$. The investigation showed that the hydrides containing Mg, Al, Cr, Mn, Mo, and Ta have almost the same profile when compared to the quaternary parent hydride. Both the undistorted random *fcc* and *bct* models described well the local and medium structures.

Finally, the desorption properties were studied by performing a TDS measurement on all the hydrides. The obtained profiles showed a strong dependence on the added *M* element. The addition of a fifth element to the parent alloy resulted in the decrease of the onset temperature of desorption, when compared to the pristine alloy.

The conducted investigation in this chapter gave rise to interesting HEAs and properties. The following chapters (4 and 5) will be dedicated to the in depth study of the HEAs with the highest hydrogen uptake regarding their thermodynamics, the phase transition during absorption/desorption of hydrogen, and the cycling properties.

References

[1] SI Chemical Data, Third Edition (Aylward, Gordon; Findlay, Tristan) | Journal of Chemical Education, (n.d.). https://pubs.acs.org/doi/abs/10.1021/ed072pA109.1 (accessed June 23, 2021).

[2] J. Montero, C. Zlotea, G. Ek, J.-C. Crivello, L. Laversenne, M. Sahlberg, TiVZrNb Multi-Principal-Element Alloy: Synthesis Optimization, Structural, and Hydrogen Sorption Properties, Molecules. 24 (2019) 2799. https://doi.org/10.3390/molecules24152799.

[3] J. Montero, G. Ek, M. Sahlberg, C. Zlotea, Improving the hydrogen cycling properties by Mg addition in Ti-V-Zr-Nb refractory high entropy alloy, Scripta Materialia. 194 (2021) 113699. https://doi.org/10.1016/j.scriptamat.2020.113699.

[4] J. Montero, G. Ek, L. Laversenne, V. Nassif, M. Sahlberg, C. Zlotea, How 10 at% Al Addition in the Ti-V-Zr-Nb High-Entropy Alloy Changes Hydrogen Sorption Properties, Molecules (Basel, Switzerland). 26 (2021). https://doi.org/10.3390/molecules26092470.

[5] A. Bouzidi, L. Laversenne, V. Nassif, E. Elkaim, C. Zlotea, Hydrogen Storage Properties of a New Ti-V-Cr-Zr-Nb High Entropy Alloy, Hydrogen. 3 (2022) 270–284. https://doi.org/10.3390/hydrogen3020016.

[6] A. Bouzidi, L. Perrière, E. Elkaim, L. Laversenne, V. Nassif, G. Vaughan, C. Zlotea, Exploring the Hydrogen Sorption Capabilities of a Novel Ti-V-Mn-Zr-Nb High-Entropy Alloy, Inorganics. 11 (2023) 186. https://doi.org/10.3390/inorganics11050186.

[7] A. Bouzidi, L. Laversenne, G. Zepon, G. Vaughan, V. Nassif, C. Zlotea, Hydrogen Sorption Properties of a Novel Refractory Ti-V-Zr-Nb-Mo High Entropy Alloy, Hydrogen. 2 (2021) 399–413. https://doi.org/10.3390/hydrogen2040022.

[8] J. Montero, G. Ek, L. Laversenne, V. Nassif, G. Zepon, M. Sahlberg, C. Zlotea, Hydrogen storage properties of the refractory Ti–V–Zr–Nb–Ta multi-principal element alloy, Journal of Alloys and Compounds. 835 (2020) 155376. https://doi.org/10.1016/j.jallcom.2020.155376.

[9] X. Yang, Y. Zhang, Prediction of high-entropy stabilized solid-solution in multi-component alloys, Materials Chemistry and Physics. 132 (2012) 233–238. https://doi.org/10.1016/j.matchemphys.2011.11.021.

[10] M.M. Nygård, G. Ek, D. Karlsson, M.H. Sørby, M. Sahlberg, B.C. Hauback, Counting electrons - A new approach to tailor the hydrogen sorption properties of high-entropy alloys, Acta Materialia. 175 (2019) 121–129. https://doi.org/10.1016/j.actamat.2019.06.002.

[11] B.H. Silva, C. Zlotea, Y. Champion, W.J. Botta, G. Zepon, Design of TiVNb-(Cr, Ni or Co) multicomponent alloys with the same valence electron concentration for hydrogen storage, Journal of Alloys and Compounds. 865 (2021) 158767. https://doi.org/10.1016/j.jallcom.2021.158767.

[12] J.P. Couzinié, G. Dirras, L. Perrière, T. Chauveau, E. Leroy, Y. Champion, I. Guillot, Microstructure of a near-equimolar refractory high-entropy alloy, Materials Letters. 126 (2014) 285–287. https://doi.org/10.1016/j.matlet.2014.04.062.

[13] ASM Handbook Volume 3: Alloy Phase Diagrams, ASM International. (n.d.). https://www.asminternational.org/asm-handbook-volume-3-alloy-phase-diagrams/results/-/journal_content/56/25871543/PUBLICATION/ (accessed June 8, 2023).

[14] C. Suryanarayana, Mechanical alloying and milling, Progress in Materials Science. 46 (2001) 1–184. https://doi.org/10.1016/S0079-6425(99)00010-9.

[15] T.B. Massalski, Phase Diagrams, in: K.H.J. Buschow, R.W. Cahn, M.C. Flemings, B. Ilschner, E.J. Kramer, S. Mahajan, P. Veyssière (Eds.), Encyclopedia of Materials:

Science and Technology, Elsevier, Oxford, 2001: pp. 6842–6851. https://doi.org/10.1016/B0-08-043152-6/01214-6.
[16] J.O. Abe, A.P.I. Popoola, E. Ajenifuja, O.M. Popoola, Hydrogen energy, economy and storage: Review and recommendation, International Journal of Hydrogen Energy. 44 (2019) 15072–15086. https://doi.org/10.1016/j.ijhydene.2019.04.068.
[17] C. Zlotea, M.A. Sow, G. Ek, J.P. Couzinié, L. Perrière, I. Guillot, J. Bourgon, K.T. Møller, T.R. Jensen, E. Akiba, M. Sahlberg, Hydrogen sorption in TiZrNbHfTa high entropy alloy, J Less Common Met. 775 (2019) 667–674. https://doi.org/10.1016/j.jallcom.2018.10.108.
[18] Y. Deng, J. Hu, S. Zhao, W. Wang, L. Xie, G. Sun, H. Shen, X. Zu, H. Xiao, Hydrogen storage properties of Mg0.10Ti0.30V0.25Zr0.10Nb0.25 lightweight high entropy alloy: A theoretical study, International Journal of Hydrogen Energy. (2023). https://doi.org/10.1016/j.ijhydene.2023.07.075.
[19] A.C. Switendick, Band Structure Calculations for Metal Hydrogen Systems*, Zeitschrift Für Physikalische Chemie. 117 (1979) 89–112. https://doi.org/10.1524/zpch.1979.117.117.089.
[20] J.F. Lynch, J.J. Reilly, F. Millot, The absorption of hydrogen by binary vanadium-chromium alloys, Journal of Physics and Chemistry of Solids. 39 (1978) 883–890. https://doi.org/10.1016/0022-3697(78)90150-6.
[21] A. Kagawa, E. Ono, T. Kusakabe, Y. Sakamoto, Absorption of hydrogen by vanadium-rich V□Ti-based alloys, Journal of the Less Common Metals. 172–174 (1991) 64–70. https://doi.org/10.1016/0022-5088(91)90433-5.
[22] G. Ek, M.M. Nygård, A.F. Pavan, J. Montero, P.F. Henry, M.H. Sørby, M. Witman, V. Stavila, C. Zlotea, B.C. Hauback, M. Sahlberg, Elucidating the Effects of the Composition on Hydrogen Sorption in TiVZrNbHf-Based High-Entropy Alloys, Inorg. Chem. 60 (2021) 1124–1132. https://doi.org/10.1021/acs.inorgchem.0c03270.
[23] H. Peisl, Lattice strains due to hydrogen in metals, in: G. Alefeld, J. Völkl (Eds.), Hydrogen in Metals I, Springer Berlin Heidelberg, Berlin, Heidelberg, 1978: pp. 53–74. https://doi.org/10.1007/3540087052_42.
[24] M.M. Nygård, W.A. Sławiński, G. Ek, M.H. Sørby, M. Sahlberg, D.A. Keen, B.C. Hauback, Local order in high-entropy alloys and associated deuterides – a total scattering and Reverse Monte Carlo study, Acta Materialia. 199 (2020) 504–513. https://doi.org/10.1016/j.actamat.2020.08.045.
[25] Y. Tong, S. Zhao, H. Bei, T. Egami, Y. Zhang, F. Zhang, Severe local lattice distortion in Zr- and/or Hf-containing refractory multi-principal element alloys, Acta Materialia. 183 (2020) 172–181. https://doi.org/10.1016/j.actamat.2019.11.026.
[26] H. Kim, K. Sakaki, H. Ogawa, Y. Nakamura, J. Nakamura, E. Akiba, A. Machida, T. Watanuki, T. Proffen, Origin of Degradation in the Reversible Hydrogen Storage Capacity of V1–xTix Alloys from the Atomic Pair Distribution Function Analysis, J. Phys. Chem. C. 117 (2013) 26543–26550. https://doi.org/10.1021/jp408766r.

CHAPTER IV

Hydrogen sorption properties of HEAs containing Cr and Mn

Chapter 4. Hydrogen sorption properties of HEAs containing Cr and Mn

In the previous chapter, it was discovered that HEAs containing Cr, Mn, Mo, and Ta presented the highest hydrogen uptake from all the series of the studied HEAs. Since the HEA containing Ta is already studied and published, in the next two chapters the focus will only be on $Ti_{0.30}V_{0.25}Zr_{0.10}Nb_{0.25}M_{0.10}$ (*M* = Cr, Mn, and Mo) HEAs. In the present chapter, the investigation will be carried out on HEAs containing *3d M* elements (Cr and Mn), whereas the fifth chapter will only deal with the quaternary alloy $Ti_{0.325}V_{0.275}Zr_{0.125}Nb_{0.275}$ alloyed with *4d M* element ,i.e., Mo.

Therefore, a focus on large scale investigations, thermodynamic properties, phase transitions, and cycling properties of the $Ti_{0.30}V_{0.25}Cr_{0.10}Zr_{0.10}Nb_{0.25}$ and $Ti_{0.30}V_{0.25}Mn_{0.10}Zr_{0.10}Nb_{0.25}$ alloys will be reported in the present chapter. The findings will also be compared to the parent quaternary alloy $Ti_{0.325}V_{0.275}Zr_{0.125}Nb_{0.275}$ for the purpose of emphasizing the effect of addition of a fifth element on the hydrogen sorption properties.

4.1 Structural properties of dihydrides containing Cr and Mn

After the hydrogenation (described in chapter 3), the structure of $Ti_{0.30}V_{0.25}Zr_{0.10}Nb_{0.25}Cr_{0.10}H_2$ and $Ti_{0.30}V_{0.25}Zr_{0.10}Nb_{0.25}Mn_{0.10}H_2$ dihydrides were confirmed by SR-XRD and PDF as a *fcc* phase ($Fm\bar{3}m$). Furthermore, the interest will be to determine the hydrogen/deuterium occupation position in the lattice of the dihydride phase by neutron powder diffraction. As mentioned in chapter 2, here, neutron diffraction is used to locate the position of deuterium atoms within the deuterated samples (figure 4.1.a-b). Data obtained from SR-XRD and PDF refinements (chapter 3) will be also used for comparison purposes with results from *ex-situ* neutron diffraction.

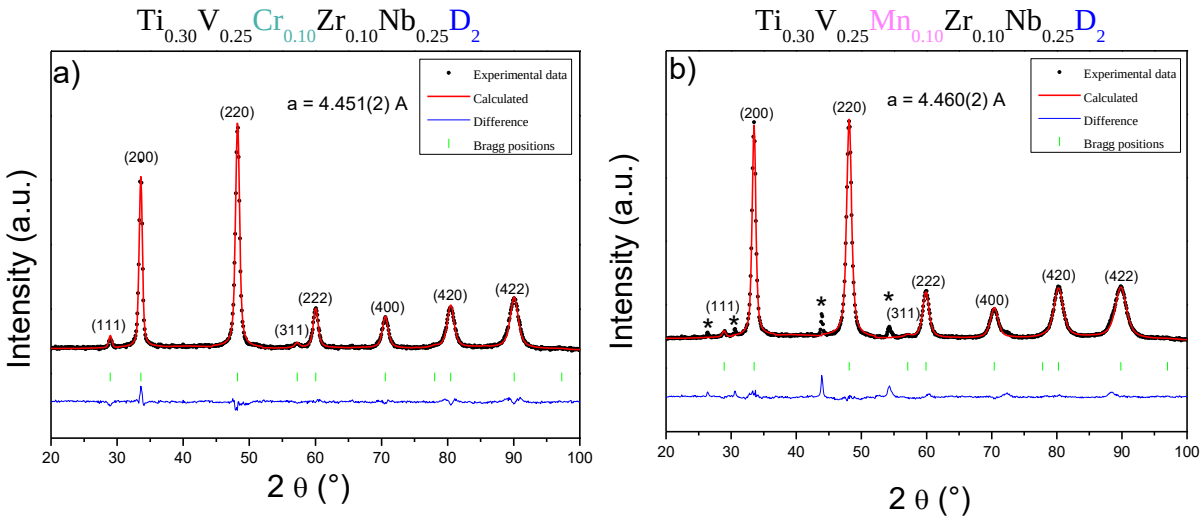

Figure 4.1. Neutron diffraction patterns (λ= 1.2858 Å) of $Ti_{0.30}V_{0.25}Cr_{0.10}Zr_{0.10}Nb_{0.25}D_2$ (a) and $Ti_{0.30}V_{0.25}Mn_{0.10}Zr_{0.10}Nb_{0.25}D_2$ (b) and their corresponding Rietveld analysis. Impurities are indicated by a star symbol (*).

Sample	*fcc* lattice parameter a_{fcc} (Å)			Deuterium position in the unit cell
	SR-XRD	Neutron diffraction	PDF	
$Ti_{0.30}V_{0.25}Cr_{0.10}Zr_{0.10}Nb_{0.25}\mathbf{H_2}$	4.459 (1)	-	4.465 (1)	-
$Ti_{0.30}V_{0.25}Cr_{0.10}Zr_{0.10}Nb_{0.25}\mathbf{D_2}$	-	4.451 (2)	-	$\frac{1}{4},\frac{1}{4},\frac{1}{4}$
$Ti_{0.30}V_{0.25}Mn_{0.10}Zr_{0.10}Nb_{0.25}\mathbf{H_2}$	4.482 (1)	-	4.485 (1)	-
$Ti_{0.30}V_{0.25}Mn_{0.10}Zr_{0.10}Nb_{0.25}\mathbf{D_2}$	-	4.460 (2)	-	$\frac{1}{4},\frac{1}{4},\frac{1}{4}$

Table 4.1. The *fcc* lattice parameter of $Ti_{0.30}V_{0.25}Cr_{0.10}Zr_{0.10}Nb_{0.25}H(D)_2$ and $Ti_{0.30}V_{0.25}Mn_{0.10}Zr_{0.10}Nb_{0.25}H(D)_2$ from SR-XRD (Cristal soleil), neutron diffraction (D1B ILL), and PDF analysis (1D15 ESRF). The deuterium position as obtained from neutron diffraction Rietveld analysis.

The Rietveld refinement of the *ex-situ* neutron diffraction of both Cr and Mn containing HEAs showed that both samples crystallize in a *fcc* ($Fm\bar{3}m$) type structure (figure 4.1.a-b). However, the $Ti_{0.30}V_{0.25}Mn_{0.10}Zr_{0.10}Nb_{0.25}D_2$ sample contained a small amount of a secondary phase, which could possibly be a *bcc* ($Im\bar{3}m$) monohydride phase (marked with *) (figure 4.1.b). The refinement of the *ex-situ* neutron diffraction patterns showed that the *fcc* lattice parameter of both deuterated samples were in a good agreement with previous analysis of SR-XRD and PDF (table 4.1). Furthermore, the deuterium was confirmed to occupy the tetrahedral sites of the *fcc* structure ($^1/_4$, $^1/_4$, $^1/_4$) in both dideuteride samples (Cr and Mn) (figure 4.2). Interestingly, previous reports on similar HEAs confirmed the same result regarding the hydrogen/deuterium occupation in the lattice [1,2].

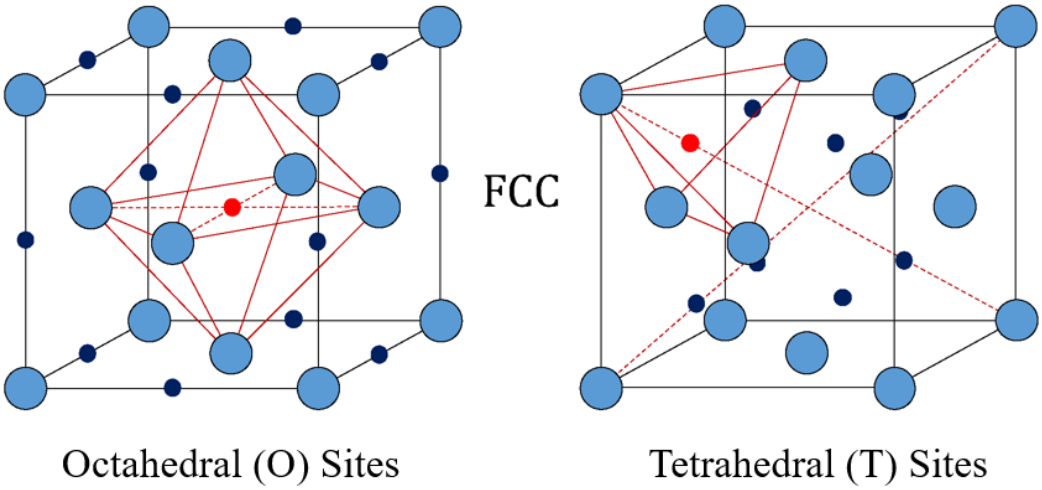

Figure 4.2. Hydrogen/deuterium localization in the tetrahedral and octahedral sites of the *fcc* structure [3].

4.2 Thermodynamic properties of HEAs containing Cr and Mn

As it was previously shown, the HEAs $Ti_{0.30}V_{0.25}Zr_{0.10}Nb_{0.25}M_{0.10}$ (*M* = Cr and Mn) were synthesized by AM and both crystallize in a *bcc* lattice ($Im\bar{3}m$). At room temperature, a PCI measurement (figure 3.11) was conducted on both samples which showed a one plateau of hydrogen absorption at very low equilibrium pressure (within the limit of the pressure 10^{-2} bar). In order to determine the enthalpy and entropy of hydride formation, PCIs were measured at higher temperatures on $Ti_{0.30}V_{0.25}Zr_{0.10}Nb_{0.25}M_{0.10}$ (*M* = Cr and Mn) alloys, as illustrated in figure 4.3.a-b, respectively.

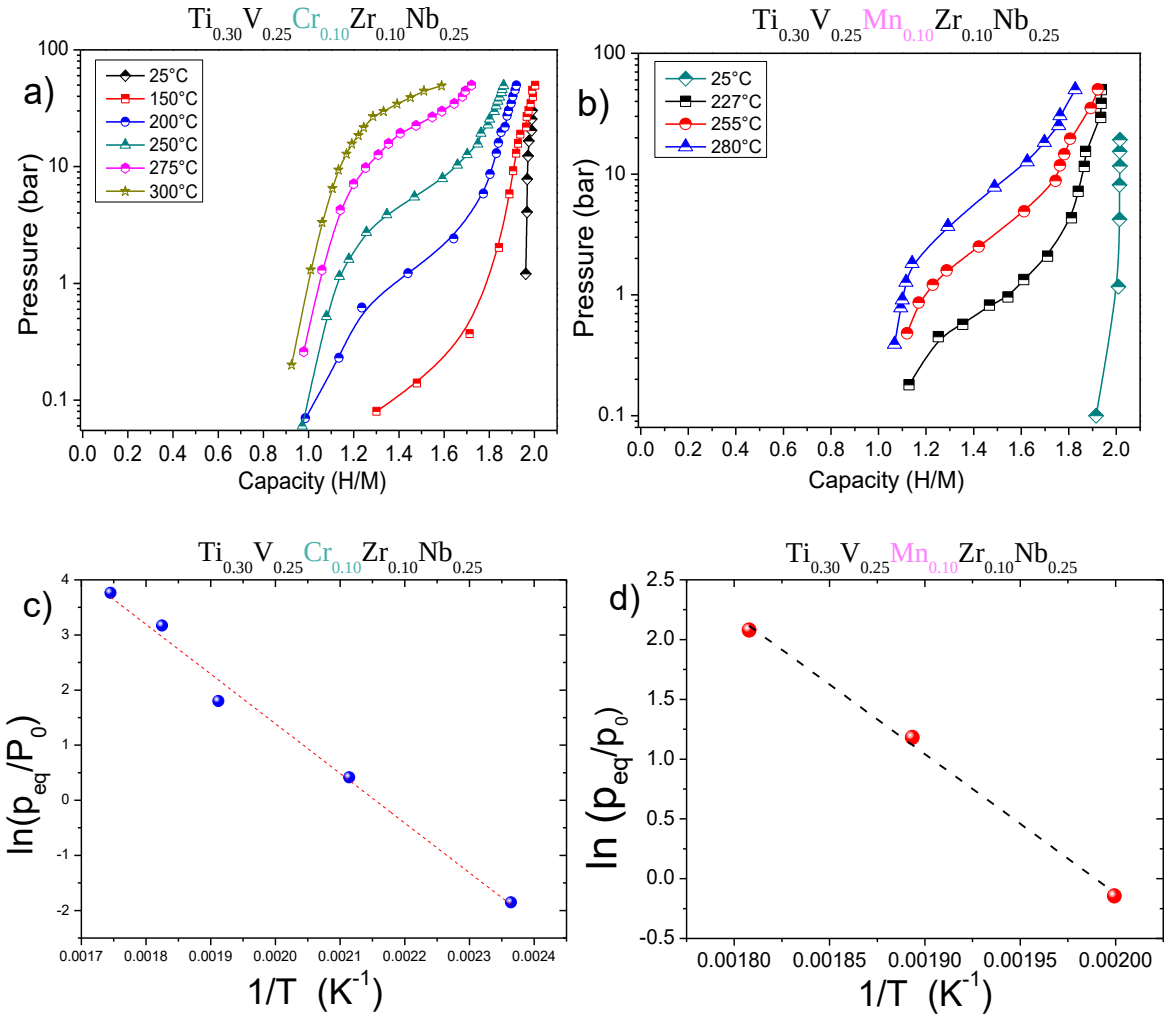

Figure 4.3. Pressure-composition isotherms at 25, 150, 200, 250, 275, and 300°C for $Ti_{0.30}V_{0.25}Cr_{0.10}Zr_{0.10}Nb_{0.25}$ (a) and at 25, 227, 255, and 280°C for $Ti_{0.30}V_{0.25}Mn_{0.10}Zr_{0.10}Nb_{0.25}$ (b), Van't Hoff plot applied on data obtained at high temperature for Cr (c) and Mn (d) containing alloys.

Depending on the temperature, the PCI profiles of $Ti_{0.30}V_{0.25}Cr_{0.10}Zr_{0.10}Nb_{0.25}$ alloy are different (figure 4.3-a). With the increase of the temperature from 25°C to 150°C, no sign of a plateau was observed. However, from 200 to 300 °C, a plateau was observed, and the equilibrium pressure increased with the temperature. Moreover, the capacity of hydrogen uptake was inversely proportional to the temperature increase, by dropping from 2 H/M at 150 °C to 1.59 H/M at 300 °C. A similar behavior was also observed with $Ti_{0.30}V_{0.25}Mn_{0.10}Zr_{0.10}Nb_{0.25}$ alloy. The measured PCIs showed a clear plateau in the range of 227-280 °C (figure 4.3-b). The capacity decreased with the increase of the temperature from 2 H/M to 1.38 H/M, at 25°C to 280 °C , respectively. Both PCI curves at high temperatures for $Ti_{0.30}V_{0.25}Zr_{0.10}Nb_{0.25}M_{0.10}$ (M = Cr and Mn) alloys suggest a two-step reaction with hydrogen

which are the following: one transition at very low equilibrium pressure forming a monohydride (1 H/M), followed by another reaction at higher pressure forming a dihydride (2 H/M).

The equilibrium pressure of the second transition (monohydride to dihydride) allows the calculation of both the enthalpy (ΔH_{abs}) and the entropy (ΔS_{abs}) variations of the absorption reaction using Van't Hoff equation (Eq. 2.14) (figure 4.2 c-d).

Composition	ΔH_{abs}(KJ/mol H_2)	ΔS_{abs}(J/Kmol H_2)	Reference
$Ti_{0.30}V_{0.25}Cr_{0.10}Zr_{0.10}Nb_{0.25}$	-75 (±4)	-161 (±8)	[4]
$Ti_{0.30}V_{0.25}Mn_{0.10}Zr_{0.10}Nb_{0.25}$	-97 (±5)	-193 (±9)	[5]
TiVZrNb	-67.6 (±5)	-90.3	[6]
$(TiVNb)_{0.85}Cr_{0.15}$	-67 (±2)	-172 (±4)	[7]
TiVZrNbHf	-61.8	-88	[6]
$TiV_{0.5}ZrNbHf$	-59.1	-87.4	[6]

Table 4.2. Thermodynamic properties for dihydride formation in $Ti_{0.30}V_{0.25}Cr_{0.10}Zr_{0.10}Nb_{0.25}$ and $Ti_{0.30}V_{0.25}Mn_{0.10}Zr_{0.10}Nb_{0.25}$, as determined by Van't Hoff analysis. $\Delta H_{abs}$and ΔS_{abs} of other similar alloys are also listed.

Table 4.2 illustrates the determined results of ΔH_{abs} and ΔS_{abs} of both Cr and Mn containing HEAs together with thermodynamic values from previously reported studies for other related alloys [6,7]. When comparing the addition of 10 at.% of Cr and Mn to the quaternary alloy, the addition of Mn results in the formation of a very stable dihydride phase, which is more stable than the $Ti_{0.30}V_{0.25}Cr_{0.10}Zr_{0.10}Nb_{0.25}$ alloy or other studied compositions (table 4.2). The entropy values of Cr and Mn containing alloys are larger than the value of H_2 gas entropy (-130 J/K molH_2). The calculation of these values could be influenced by the slopping nature of the PCI measurements which makes the determination of the mid-plateau pressures difficult. Moreover, the short range of temperatures of the measured PCIs could also influence the linear regression of the Van't Hoff plot. Hence, the latter mentioned reasons may introduce errors to the thermodynamic evaluations of both Cr and Mn containing alloys [8].

4.3 Phase transition studies by ex-situ diffraction

The previous PCI measurements suggested the existence of two phase transitions during the hydrogenation process. To clarify and confirm these phase transition, *ex-situ* SR-XRD was used to characterize the $Ti_{0.30}V_{0.25}Cr_{0.10}Zr_{0.10}Nb_{0.25}$ and $Ti_{0.30}V_{0.25}Mn_{0.10}Zr_{0.10}Nb_{0.25}$ alloys at different stages of hydrogenation process.

The Cr containing alloy was characterized at the following stages: fully desorbed (0 H/M) and three intermediate stages (0.3 H/M, 0.8 H.M, and 1.3 H/M). The SR-XRD full dihydride phase will also be used to have the complete series of hydrogenation (figure 4.3).

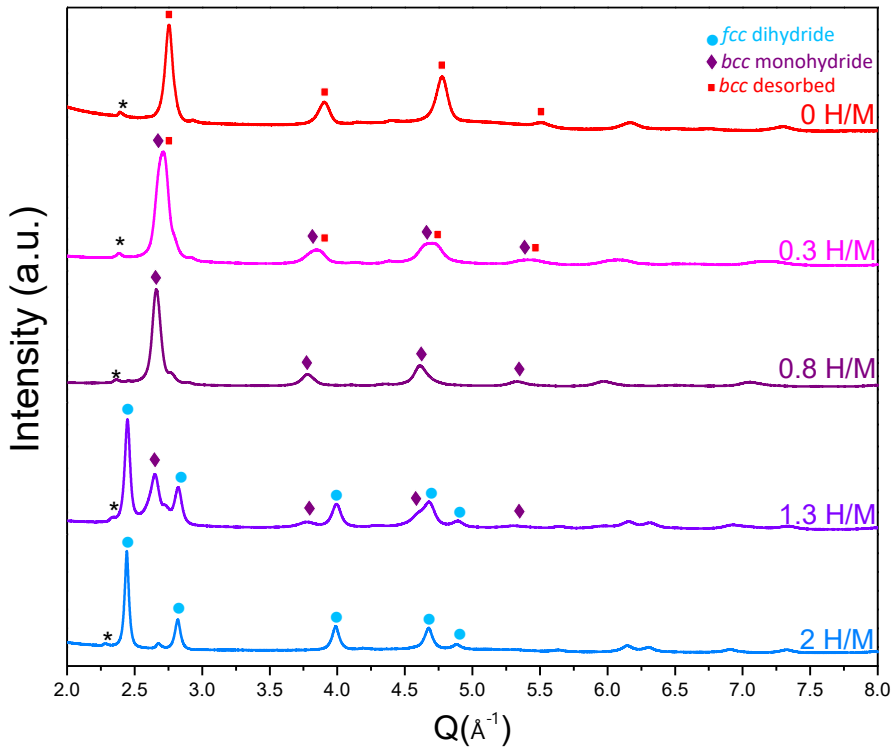

Figure 4.3. *Ex-situ* SR-XRD patterns of $Ti_{0.30}V_{0.25}Cr_{0.10}Zr_{0.10}Nb_{0.25}$ at different stages of the hydrogenation process with the following capacities: 2.0 H/M, 1.3 H/M, 0.8 H/M, 0.3 H/M, and 0 H/M. Dihydride *fcc*, *bcc* monohydride, and *bcc* desorbed phases are marked with blue circles, purple diamonds, and red squares, respectively. Minor impurity is marked with a star symbol (*).

Hydrogen capacity (H/M)	***fcc* dihydride lattice parameter (Å)**	***fcc* phase fraction (%)**	***bcc* monohydride lattice parameter (Å)**	***bcc* phase fraction (%)**	***bcc* (desorbed) lattice parameter (Å)**	***bcc* phase fraction (%)**
2.0	4.459 (1)	100	-	-	-	-
1.3	4.399 (1)	54	3.305 (1)	46	-	-
0.8	-	-	3.322 (1)	100	-	-
0.3	-	-	3.245 (5)	56	3.194 (5)	44
0.0	-	-	-	-	3.222 (2)	100

Table 4.3. The phase structure, phase fraction, and lattice parameters at different stages of the dehydrogenation process of the $Ti_{0.30}V_{0.25}Cr_{0.10}Zr_{0.10}Nb_{0.25}$ alloy.

The XRD patterns shown in figure 4.3 were analyzed by Rietveld analysis method. The results of the Rietveld refinement are listed in table 4.3. The dihydride phase (2 H/M) is a *fcc* phase structure with a lattice parameter a_{fcc}= 4.459 (1) Å. By decreasing the hydrogen capacity, the sample containing 1.3 H/M showed a coexistence of two different phases: a dihydride *fcc* phase with a lattice parameter a_{fcc}= 4.399 (1) Å (phase fraction 54%) and a second monohydride

bcc phase with a lattice parameter a_{bcc}= 3.305 (1) Å (phase fraction of 46%). The coexistence of both phases (*fcc* dihydride and *bcc* monohydride) indicates the presence of a plateau in the hydrogen absorption PCI. At 0.8 H/M, only the *bcc* monohydride phase is present with a lattice parameter a_{bcc}= 3.322 (1) Å. At 0.3 H/M, the sample contains a mixture of two phases: a *bcc* monohydride phase with a lattice parameter a_{bcc}= 3.245 (5) Å (phase fraction of 56%) and a *bcc* desorbed phase with a lattice parameter a_{bcc}=3.194 (5) Å (phase fraction of 44%). The lattice parameter of the desorbed *bcc* phase is slightly smaller than the lattice parameter of the as-cast *bcc* phase (a_{bcc}= 3.225 (1) Å) (as seen in chapter 3). The reason behind this discrepancy might be due to the use of different diffractometers: the as-cast material was characterized by the laboratory instrument, whereas the 0.3 H/M material was characterized by Synchrotron radiation. Furthermore, the full width half maximum (FWHM) of the first peak (110) of the *bcc* phase of both materials (0.3 H/M and 0.8 H/M) show different values: the FWHM of the first peak (110) was 0.535° for the *bcc* monohydride, whereas the FWHM of the 0.3 H/M material was 0.723° for the first peak of the *bcc* phase. The higher FWHM proves the coexistence of two convoluted *bcc* phases which are the monohydride and the desorbed material with very close lattice parameters. Hence, a two-step reaction with hydrogen is confirmed for the $Ti_{0.30}V_{0.25}Cr_{0.10}Zr_{0.10}Nb_{0.25}$ alloy. Lastly, the desorbed material presented a *bcc* single phase with a lattice parameter a_{bcc}= 3.222 (2) Å, which is very close to the as-cast lattice parameter a_{bcc}= 3.225 (1) Å. The result of the desorption of the hydride material confirmed the reversibility of the alloy during the hydrogenation process.

The same hydrogenation process was studied on the $Ti_{0.30}V_{0.25}Mn_{0.10}Zr_{0.10}Nb_{0.25}$ alloy, as illustrated in figure 4.4. Several samples were prepared with different hydrogen absorption capacities: 2 H/M (already shown in chapter 3), 0.8 H/M, 0.5 H/M, and a fully desorbed material.

The structural properties of each material with different capacity of hydrogen are listed in table 4.4. At 2 H/M, the dihydride phase is a *fcc* with a lattice parameter a_{fcc}= 4.482 (1) Å. The intermediate material with 0.8 H/M of hydrogen capacity crystallizes in a monohydride *bcc* single phase with a lattice parameter a_{bcc}= 3.340 (1) Å. The variation of the capacity from 2 H/M to 0.8 H/M confirms the transition from *fcc* dihydride to a *bcc* monohydride phase. Next, by decreasing the capacity from 0.8 H/M to 0.5 H/M, the material crystallizes in two *bcc* phases: a monohydride phase with a lattice parameter a_{bcc}= 3.261 (5) Å (54% phase fraction) and a *bcc* solid solution phase with a lattice parameter a_{bcc}= 3.243 (5) Å (46% phase fraction). Finally, the phase present in the desorbed material is the same *bcc* phase as the as-cast material but with

slightly higher lattice parameter a_{bcc}= 3.251 (2) Å than the as-cast material a_{bcc}= 3.239 (5) Å. The reason behind the slightly higher lattice parameter could probably be caused by the uncomplete hydrogen desorption.

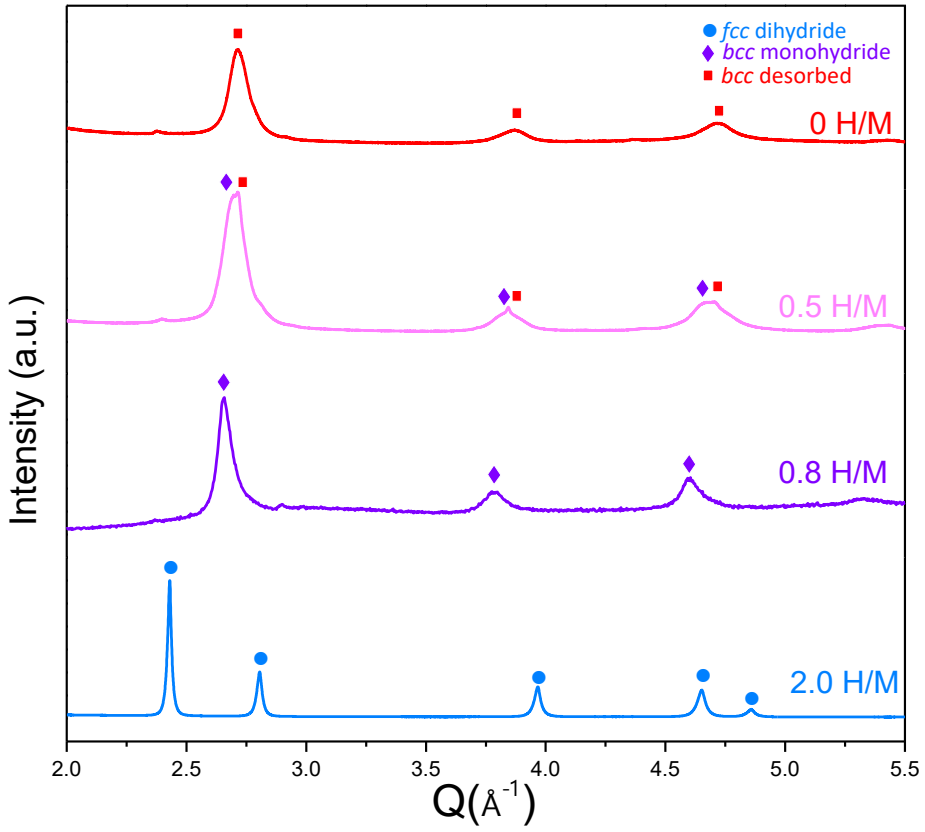

Figure 4.4. XRD patterns at different stages of the dehydrogenation process (2H/M, 0.8 H/M, 0.5 H/M, and 0 H/M (fully desorbed)) of the $Ti_{0.30}V_{0.25}Mn_{0.10}Zr_{0.10}Nb_{0.25}$ alloy. Dihydride *fcc*, *bcc* monohydride, and *bcc* desorbed phases are marked with blue circles, purple diamonds, and red squares, respectively.

Hydrogen capacity (H/M)	***fcc* dihydride lattice parameter (Å)**	***fcc* phase fraction (%)**	***bcc* monohydride lattice parameter (Å)**	***bcc* phase fraction (%)**	***bcc* (desorbed) lattice parameter (Å)**	***bcc* phase fraction (%)**
2.0	4.482 (1)	100	-	-	-	-
0.8	-	-	3.340 (1)	100	-	-
0.5	-	-	3.261 (5)	54	3.243 (5)	46
0.0	-	-	-	-	3.251 (2)	100

Table 4.4. The phase structure, phase fraction, and lattice parameters at different stages of the dehydrogenation process of the $Ti_{0.30}V_{0.25}Mn_{0.10}Zr_{0.10}Nb_{0.25}$ alloy.

The analysis of materials with different hydrogen capacities showed the presence of two phase transitions for both $Ti_{0.30}V_{0.25}Cr_{0.10}Zr_{0.10}Nb_{0.25}$ and $Ti_{0.30}V_{0.25}Mn_{0.10}Zr_{0.10}Nb_{0.25}$ alloys. Hence, the PCIs and the structural analysis are in agreement showing a two step reaction with hydrogen for both HEAs.

4.4 Phase transition studies by *in-situ* diffraction

For an in depth comprehension of the phase transition during deuterium desorption, *in-situ* neutron diffraction was carried out on deuterated material $Ti_{0.30}V_{0.25}Cr_{0.10}Zr_{0.10}Nb_{0.25}$ as illustrated in figure 4.5.

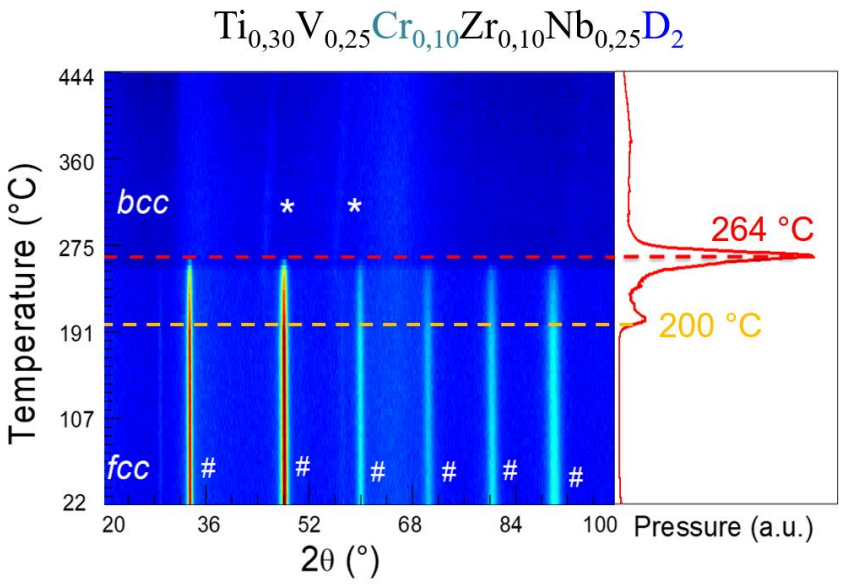

Figure 4.5. *In-situ* neutron diffraction during deuterium desorption from $Ti_{0.30}V_{0.25}Cr_{0.10}Zr_{0.10}Nb_{0.25}D_2$ (λ=1.28 Å), with a heating rate of 1°C/min from 22°C to 450°C under dynamic vacuum (left) and the corresponding gas desorption profile (right).

The recorded *in-situ* neutron diffraction was carried out by heating to 450°C with a rate of 1°C/min under dynamic vacuum. In figure 4.5 (right) is plotted the desorption profile of the evolved gas.

Starting from the bottom to the top of figure 4.5 (left), the deuteride *fcc* phase of $Ti_{0.30}V_{0.25}Cr_{0.10}Zr_{0.10}Nb_{0.25}D_2$ (marked with #) is stable until reaching the temperature 200°C where the diffraction signals of the *fcc* deuteride phase starts to smoothly decrease. The fading of the intensity of the diffraction peaks is associated to the starting of the deuterium desorption from the sample as shown by the first peak in the recorded desorption profile (figure 4.5-right). At 264°C, a sharp transition occurs with a complete vanishing of the *fcc* diffraction peaks. This is also confirmed by the desorption profile (figure 4.5 a-right), where an intense peak is observed at 264°C. Succeeding the phase transition of the *fcc* phase to the desorbed phase, two very weak diffraction peaks can be noticed (marked with *).

Following the transition, the deuterium content in the alloy becomes very low resulting in a very weak diffraction peaks of the desorbed phase, hence, the exploitation of the structural transition cannot be possible.

Thus, for an in depth description of the phase transition, an *in-situ* SR-XRD measurement was performed on $Ti_{0.30}V_{0.25}Cr_{0.10}Zr_{0.10}Nb_{0.25}H_2$ hydride. The experiment consisted of applying a constant heating rate from 25°C to 450°C with 2°C/min under secondary dynamic vacuum on the hydride material.

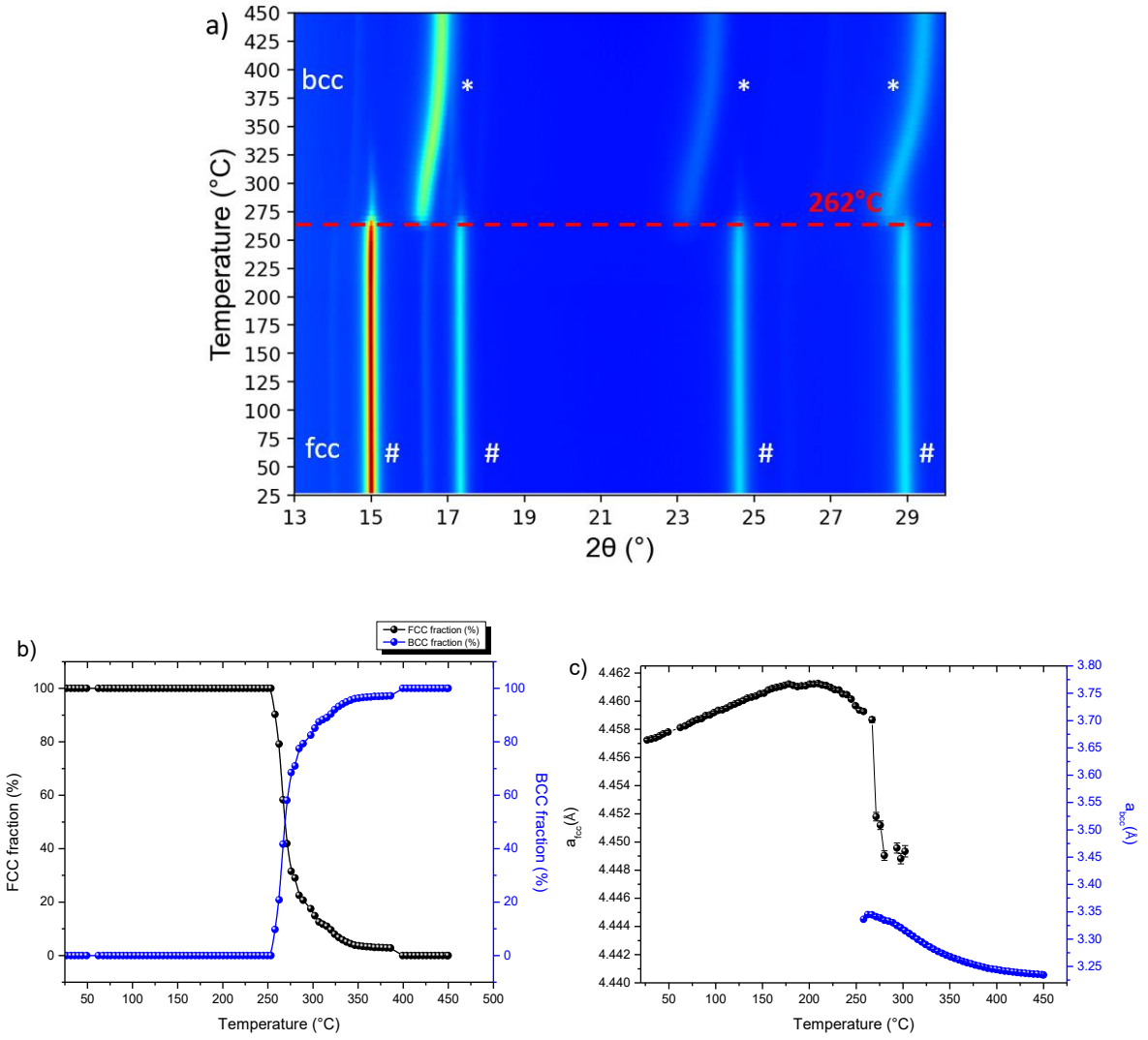

Figure 4.6. *In-situ* SR-XRD (λ=0.67156 Å) of $Ti_{0.30}V_{0.25}Cr_{0.10}Zr_{0.10}Nb_{0.25}H_2$ dihydride (a) during hydrogen desorption by heating from 25 to 450°C under dynamic vacuum. The thermal evolution of the *fcc* and *bcc* phase fractions (b). The variation of the lattice parameters of the *fcc* and *bcc* phases against the temperature (c).

Figure 4.6.a displays the thermo-diffractograms of $Ti_{0.30}V_{0.25}Cr_{0.10}Zr_{0.10}Nb_{0.25}H_2$ dihydride during hydrogen desorption. The *fcc* dihydride phase (marked with #) is stable until

reaching 262°C where a sharp phase transition takes place. Following the phase transition, a clear *bcc* desorbed phase (marked with *) is identified. The temperature of the phase transition is in a good agreement with previous *in-situ* neutron diffraction experiment on the $Ti_{0.30}V_{0.25}Cr_{0.10}Zr_{0.10}Nb_{0.25}D_2$ sample.

In order to characterize the evolution of the structure during the desorption of hydrogen, a Rietveld analysis was applied on all the diffraction patterns to obtain an in depth structural information upon the transition.

Figure 4.6.b and c represents the thermal variation of the phase fractions and the lattice parameters, respectively. When the temperature increased from 25°C to 180°C, a variation of the *fcc* lattice parameter is identified from 4.457 (1) Å to 4.461 (1) Å, this is due to the thermal expansion of the lattice (figure 4.7.c). For higher temperatures, the *fcc* lattice parameter stabilizes around 4.46 (1) Å due to the simultaneous occurrence of the thermal expansion and the start of the hydrogen desorption resulting in the shrinking of the lattice. In the range of 220°C and 250°C, a strong decrease of the *fcc* lattice parameter is noticed, hinting to a major hydrogen desorption event. Furthermore, in the temperature range of 250°C to 300°C, a phase transition takes place from *fcc* to a *bcc* phase. The temperature of the phase transition is in agreement with the neutron diffraction findings. At around 300°C, the *fcc* lattice parameter decreases drastically reaching 4.449 (4) Å which is followed by a complete vanishing of the dihydride phase, leaving only the newly formed *bcc* phase. Interestingly, the lattice parameter of the *bcc* phase constantly decreases from 3.336 (2) Å at 260°C to 3.234 (2) Å at 450°C. Thus, hydrogen is still desorbing from the sample after the phase transition from *fcc* to *bcc* lattice. The last value of the desorbed *bcc* phase (a_{bcc}= 3.234 (2) Å) is slightly higher than the *bcc* lattice parameter of the as-cast sample (a_{bcc}=3.225 (1) Å) (shown in chapter 3) probably due to thermal expansion.

As seen in previous results from PCI measurements and the *ex-situ* SR-XRD investigations at different steps of hydrogenation, the $Ti_{0.30}V_{0.25}Cr_{0.10}Zr_{0.10}Nb_{0.25}$ alloy showed a two-step reaction with hydrogen: *fcc* dihydride ↔ *bcc* monohydride ↔ *bcc* desorbed phase. However, the *in-situ* SR-XRD during hydrogen desorption of the dihydride sample showed only one transition from *fcc* to *bcc* phase. The absence of the second transition from *bcc* monohydride to *bcc* desorbed phase could be explained by the similarity of the crystalline structures (*bcc*) and the very slight rearrangement of atoms during the second transition.

Similarly to the Cr containing alloy, the $Ti_{0.30}V_{0.25}Mn_{0.10}Zr_{0.10}Nb_{0.25}$ HEA is also studied by *in-situ* neutron diffraction with the same methodology.

The *in-situ* neutron diffraction was carried out on deuterated material $Ti_{0.30}V_{0.25}Mn_{0.10}Zr_{0.10}Nb_{0.25}D_2$ for the purpose of studying the phase transition during deuterium desorption, as illustrated in figure 4.7.

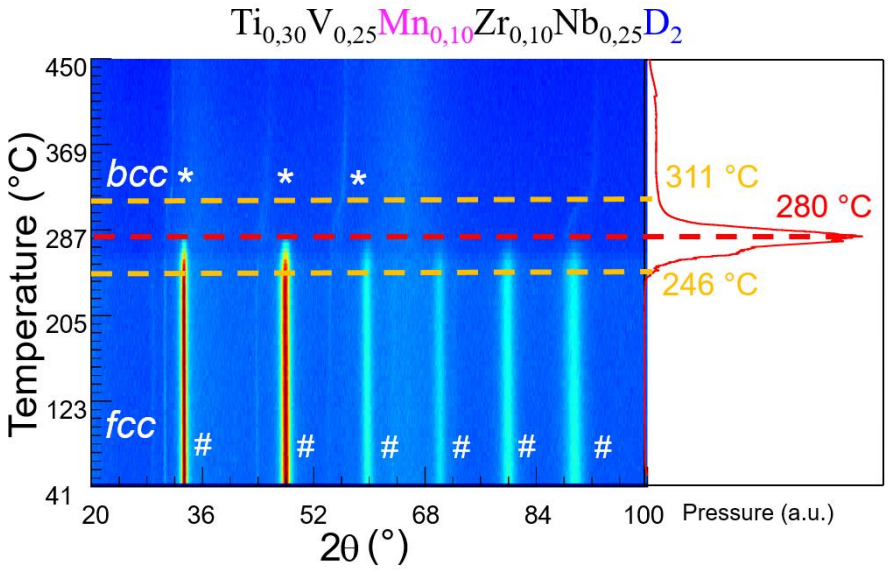

Figure 4.7. *In-situ* neutron diffraction of $Ti_{0.30}V_{0.25}Mn_{0.10}Zr_{0.10}Nb_{0.25}D_2$ (λ=1.28 Å) heated at constant temperature rate 1°C/min from 41°C to 450°C (left) and the vacuum pressure readings during deuterium desorption (right).

In figure 4.7 (left), the diffraction signals of the *fcc* phase of the $Ti_{0.30}V_{0.25}Mn_{0.10}Zr_{0.10}Nb_{0.25}D_2$ sample remain stable until reaching 246°C, where a smooth fading of signals intensity occurs. This is due to the starting of the deuterium desorption which is confirmed by the first peak shown in the desorption profile (figure 4.7.right). At 280°C, a sharp transition occurs, which is confirmed by the maximum desorption rate peak of the desorption profile. Following the transition, only three weak peaks are noticed (marked with *). The latter peaks were shifting towards higher diffraction angles (2θ) until reaching 311°C, hinting for a desorption of a slight quantity of deuterium from the *bcc* solid solution. The new appeared diffraction signals could be identified as the *bcc*-desorbed phase.

Next, for a thorough characterization of the phase transition during desorption, *in-situ* SR-XRD measurements were performed on the $Ti_{0.30}V_{0.25}Mn_{0.10}Zr_{0.10}Nb_{0.25}H_2$ hydride.

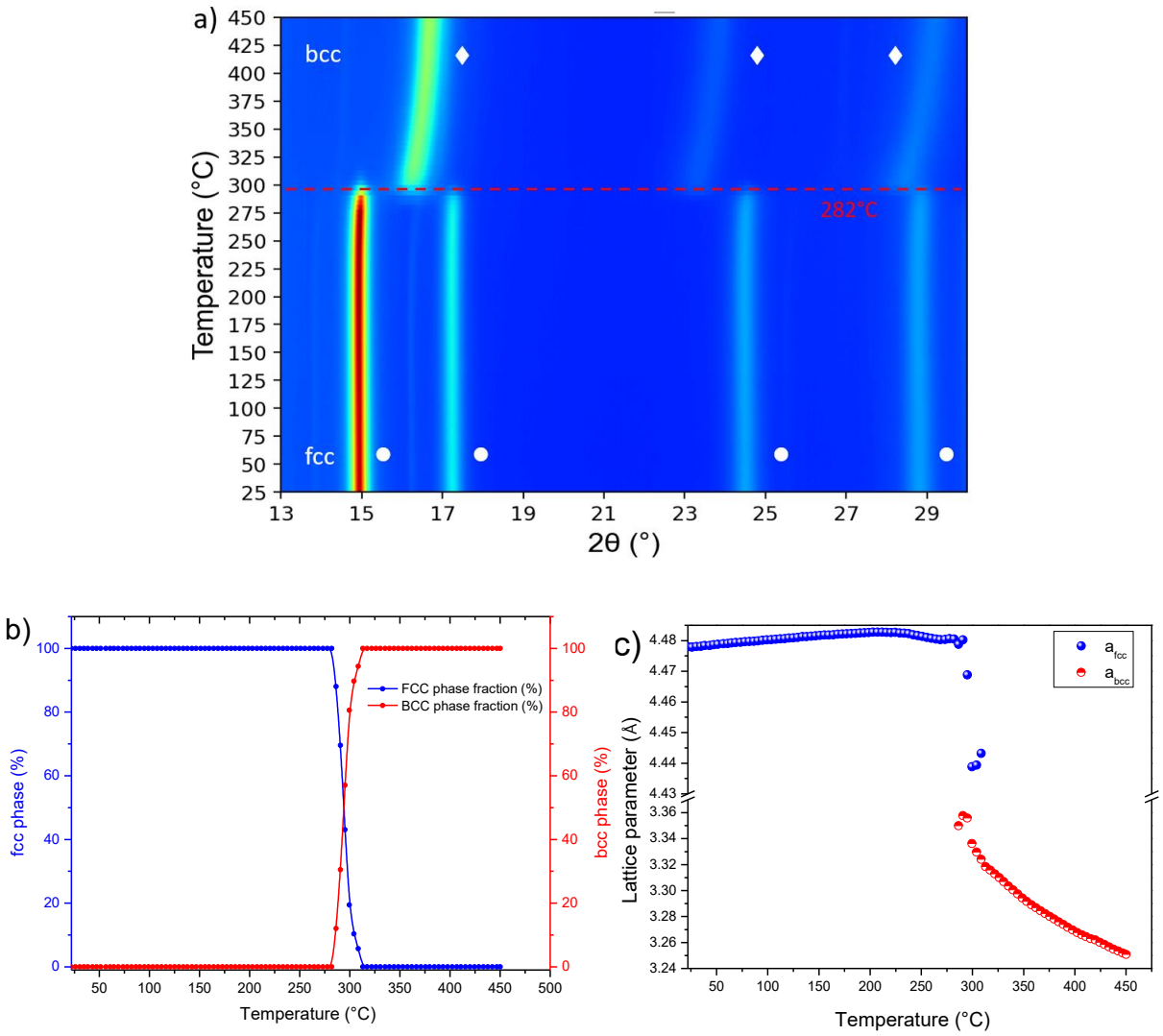

Figure 4.8. *In-situ* SR-XRD (λ=0.67156 Å) of $Ti_{0.30}V_{0.25}Mn_{0.10}Zr_{0.10}Nb_{0.25}H_2$ dihydride (a) during hydrogen desorption by heating from 25 to 450°C under dynamic vacuum. The thermal evolution of the *fcc* and *bcc* phase fractions (b). The variation of the lattice parameters of the *fcc* and *bcc* phases against the temperature (c).

Figure 4.8.a shows the performed *in-situ* SR-XRD during the hydrogen desorption from the $Ti_{0.30}V_{0.25}Mn_{0.10}Zr_{0.10}Nb_{0.25}H_2$ dihydride. The sample was heated from 25°C to 450°C with a constant heating rate of 2°C/min under dynamic vacuum.

Starting from bottom to top of figure 4.8.a, the *fcc* dihydride phase (marked with circles) remains stable up to around 282°C, where a sharp transition occurs from *fcc* dihydride to a desorbed phase. All the acquired data were analyzed by Rietveld refinement (figure 4.8.b.c). The *fcc* lattice parameter increased from 4.478 (1) Å at 25°C to 4.482 (1) Å at 211°C (figure 4.8.c) due to thermal expansion. For higher temperatures, the lattice parameter begins to slightly decrease hinting the beginning of the hydrogen desorption from the sample. In the range 282°C-

312°C, the diffraction peaks of the *fcc* dihydride starts to sharply vanish concomitantly with the formation of a newly *bcc* phase (marked with diamonds). At the same time, the *fcc* lattice parameter started to decrease from 4.482 (1) Å to 4.443 (1) Å. While the phase fraction strongly decreased from 100% to 6% (figure 4.8.c). For a temperature higher than 312°C, only the *bcc* phase exists. Interestingly, the *bcc* lattice parameter kept decreasing from 3.318 (1) Å at 312°C to 3.250 (1) Å at 450°C suggesting a continuous desorption of hydrogen from the *bcc* phase. The final lattice parameter of the *bcc* desorbed phase 3.250 (1) Å is slightly higher than the as-cast lattice parameter 3.239 (5) Å (chapter 3) due to thermal expansion that the *bcc* lattice is experiencing.

Regarding the *in-situ* neutron diffraction measurements on both Cr and Mn containing HEAs, it is worth comparing them with the study conducted on the quaternary alloy $Ti_{0.325}V_{0.275}Zr_{0.125}Nb_{0.275}$.

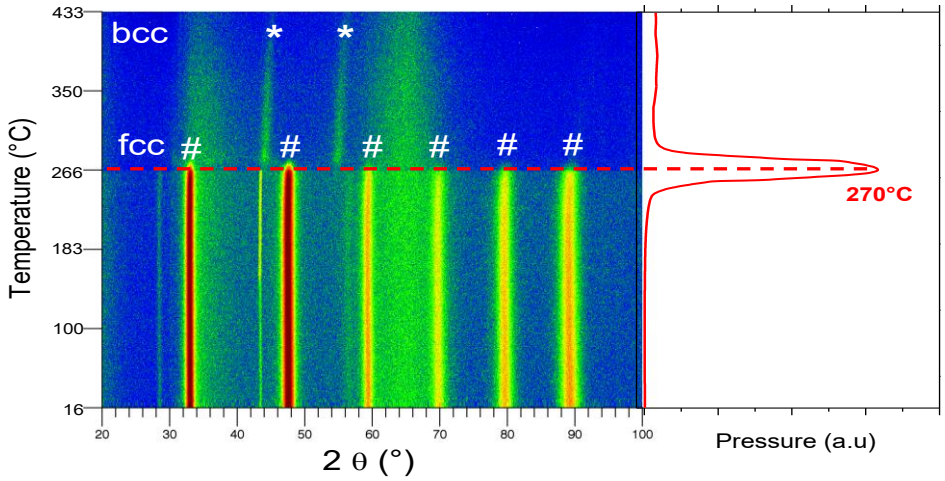

Figure 4.9. *In-situ* neutron diffraction (λ=1.28 Å) of $Ti_{0.325}V_{0.275}Zr_{0.125}Nb_{0.275}D_{1.8}$ heated at temperature rate of 1°C/min (left) and the corresponding desorption profile (right). The *fcc* and desorbed *bcc* phase are marked with the symbols # and *, respectively [9].

Figure 4.9 illustrates the thermo-diffractogram of the quaternary alloy recorded under the same experimental conditions. At around 270°C, a phase transition occurs from an initial *fcc* phase (marked with #) to a *bcc* desorbed phase (marked with *) [9]. Hence, the addition of 10 at.% of Cr to the quaternary alloy resulted in the decrease of the temperature of desorption to 264°C, leading to shorten the stability range of the *fcc* phase. Contrary to the latter case, the 10 at.% addition of Mn presented a negligible effect on the desorption temperature of the quaternary alloy.

Regarding the investigations of $Ti_{0.30}V_{0.25}Cr_{0.10}Zr_{0.10}Nb_{0.25}$, $Ti_{0.30}V_{0.25}Mn_{0.10}Zr_{0.10}Nb_{0.25}$, and $Ti_{0.325}V_{0.275}Zr_{0.125}Nb_{0.275}$ alloys by the *in-situ* neutron diffraction, the exploitation of the structural transition was not possible due to signal loss. The first reason for this result is the value of the coherent scattering length (b_c) that depends on the deuterium content in the samples as illustrated in figure 4.10. For the fully deuterated samples, the value of the b_c is around 15 and 14 fm for quinary and quaternary alloys, respectively. During the phase transition from the *fcc* to the *bcc* phase, the b_c decreases by half (8-7 fm) and when the samples are fully desorbed the value drops to approximately 2-1 fm. This suggests that the decrease of the b_c influences the scattered signals of the samples. Moreover, the phase transition occurs due to the desorption of approximately half of the content of deuterium from the sample, leaving the deuterium atoms located in random positions inside the lattice of the alloy. In principle, the diffraction occurs when the atoms of a crystal are arranged in a periodic array with long-range order, in the present case, the diffraction takes place when neutrons are scattered from deuterium which are arranged in a long range order (in the case of a fully deuterated sample). On the other hand, if the phase transition occurs, the deuterium atoms become randomly located in the sample, resulting in a short range order which will affect the produced diffraction. Thus, the intensity of the diffraction signals will be weakened (sample containing 1 D/M) or even lost (fully desorbed sample).

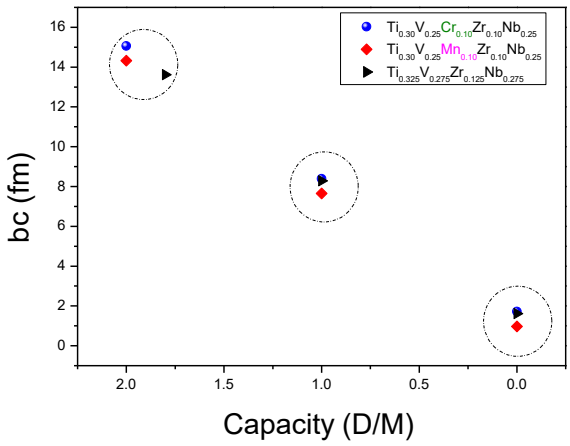

Figure 4.10. Coherent scattering length (b_c) of the Cr, Mn HEA and the quaternary alloy at different stages of deuterium desorption.

Nevertheless, the *in-situ* neutron diffraction findings are in good agreement with the *in-situ* SR-XRD regarding the temperature of the phase transition. Moreover, both investigations suggest a single step transition from *fcc* dihydride to *bcc* phase for the Cr and Mn containing alloys. However, the PCI measurements and the investigations conducted on samples with

different concentration of hydrogen showed a two-step reaction with hydrogen (*fcc* dihydride ↔ *bcc* monohydride ↔ *bcc* desorbed phase). The transition of *bcc* monohydride ↔ *bcc* desorbed phase is not detected in the *in-situ* investigations because of the very small displacements and rearrangement of atoms of the same type of crystal structure (*bcc*).

The $Ti_{0.30}V_{0.25}Cr_{0.10}Zr_{0.10}Nb_{0.25}$ and $Ti_{0.30}V_{0.25}Mn_{0.10}Zr_{0.10}Nb_{0.25}$ alloys presented a good structural reversibility during the hydrogen absorption/desorption experiment. Hence, it is interesting to study the cycling performances of both HEAs and to compare them with those of the quaternary alloy $Ti_{0.325}V_{0.275}Zr_{0.125}Nb_{0.275}$.

4.5 Hydrogen cycling performances

The hydrogen cycling performances of both $Ti_{0.30}V_{0.25}Cr_{0.10}Zr_{0.10}Nb_{0.25}$ and $Ti_{0.30}V_{0.25}Mn_{0.10}Zr_{0.10}Nb_{0.25}$ HEAs were investigated regarding the hydrogen capacity (wt.%) reversibility and kinetics of absorption during 20 cycles (absorption/desorption) (figure 4.11.a and b) (figure 4.12.a and b), respectively. For the sake of comparison, both cycling performances of HEAs were plotted and compared with the quaternary alloy $Ti_{0.325}V_{0.275}Zr_{0.125}Nb_{0.275}$ [10].

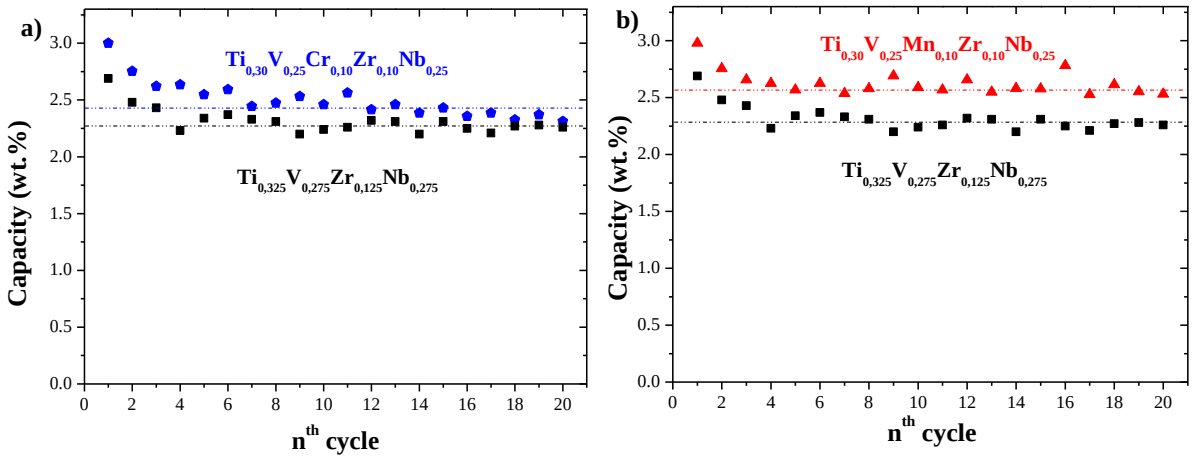

Figure 4.11. Reversible hydrogen capacity (wt.%) upon 20 absorption/desorption cycles for $Ti_{0.30}V_{0.25}Cr_{0.10}Zr_{0.10}Nb_{0.25}$ (a) and $Ti_{0.30}V_{0.25}Mn_{0.10}Zr_{0.10}Nb_{0.25}$ (b) alloys and compared to the quaternary alloy $Ti_{0.325}V_{0.275}Zr_{0.125}Nb_{0.275}$.

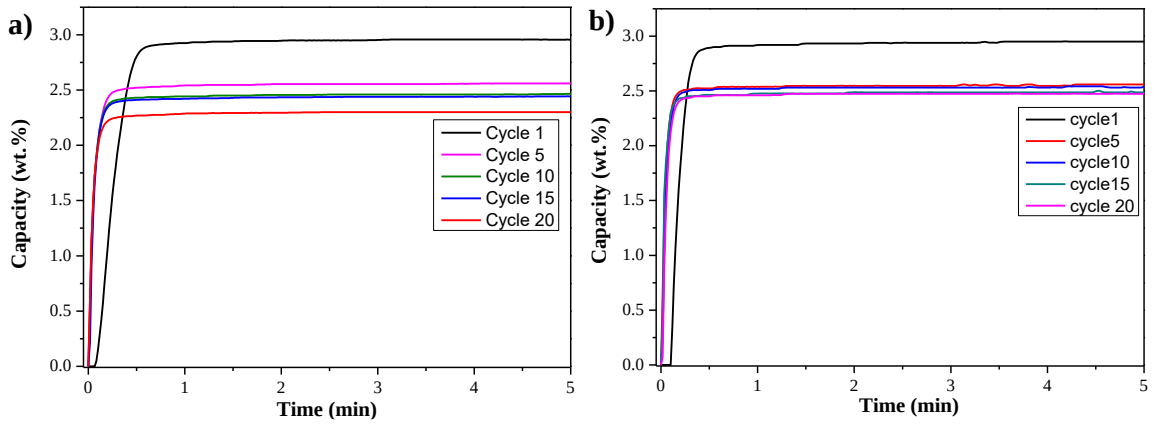

Figure 4.12. Recorded kinetic curves during hydrogen absorption (cycles: 1, 5, 10, and 20) under 50 bar at 25°C for $Ti_{0.30}V_{0.25}Cr_{0.10}Zr_{0.10}Nb_{0.25}$ (a) and $Ti_{0.30}V_{0.25}Mn_{0.10}Zr_{0.10}Nb_{0.25}$ (b) alloys.

All the hydrogen absorption measurements were performed at 25°C under 50 bar of hydrogen and the desorption was performed by heating treatment at 450°C for 3h under dynamic vacuum.

Figure 4.11.a illustrates the hydrogen absorption capacities during 20 cycles of $Ti_{0.30}V_{0.25}Cr_{0.10}Zr_{0.10}Nb_{0.25}$ alloy together with the quaternary alloy $Ti_{0.325}V_{0.275}Zr_{0.125}Nb_{0.275}$. During the first seven cycles, a fading of the hydrogen absorption capacity of the $Ti_{0.30}V_{0.25}Cr_{0.10}Zr_{0.10}Nb_{0.25}$ alloy from 3.0 wt.% to around 2.44 wt.% is measured (figure 4.11.a). Following the drop, a stabilization takes place for the rest of the cycles with a reversible capacity of hydrogen absorption around 2.44 wt.% (blue line in figure 4.11.a). Interestingly, a short incubation time is recorded on the first cycle (5 seconds), which was followed by a rapid hydrogen absorption reaching 90% of the full capacity within 30 seconds (figure 4.12.a). All the following cycles showed no incubation time and 90% of the full capacity is reached within only 15 seconds (figure 4.12.a). In fact, during the hydrogen absorption, the material undergoes a decrepitation resulting in the creation of a new fresh surfaces. The newly created surfaces will lead to higher interaction and faster dissociation of hydrogen molecules which increases the diffusion rates into the sample.

Similarly, the hydrogen cycling of the $Ti_{0.30}V_{0.25}Mn_{0.10}Zr_{0.10}Nb_{0.25}$ alloy was investigated under the same conditions. The hydrogen absorption capacity showed a drop upon the first five cycles from 2.98 wt.% to 2.60 wt.%, followed by a stabilization (figure 4.11.b). The reversible hydrogen capacity was around 2.60 wt.% (red line in figure 4.11.b). Moreover, the $Ti_{0.30}V_{0.25}Mn_{0.10}Zr_{0.10}Nb_{0.25}$ alloy showed similar kinetics of hydrogen absorption to the Cr

containing alloy. The kinetics of the first cycle showed a 6 seconds of incubation time, followed by an important absorption rate reaching 90% of the full capacity of absorption within 30 seconds (figure 4.12.b). Furthermore, all the following kinetic curves showed no incubation time and the full capacity of hydrogen absorption was reached only after 20 seconds. As explained for the $Ti_{0.30}V_{0.25}Cr_{0.10}Zr_{0.10}Nb_{0.25}$ alloy, the reason for the upgraded kinetics of hydrogen absorption during cycling is because of the formation of new fresh surfaces upon the first cycle of hydrogen absorption.

For the sake of comparison, the effect of addition of 10 at.% of Cr and Mn to the $Ti_{0.325}V_{0.275}Zr_{0.125}Nb_{0.275}$ alloy resulted in upgrading the capacity of the first cycle from 2.70 wt.% to 3.0 wt.% and 2.98 wt.% for $Ti_{0.30}V_{0.25}Cr_{0.10}Zr_{0.10}Nb_{0.25}$ and $Ti_{0.30}V_{0.25}Mn_{0.10}Zr_{0.10}Nb_{0.25}$ alloys, respectively. Moreover, the reversible capacity of hydrogen absorption was upgraded from 2.27 wt.% for quaternary alloy to 2.44 wt.% and 2.60 wt.% after the addition of 10.at% of Cr and Mn, respectively. Furthermore, the reversible capacity of the studied $Ti_{0.30}V_{0.25}Cr_{0.10}Zr_{0.10}Nb_{0.25}$ (2.44 wt.%) and $Ti_{0.30}V_{0.25}Mn_{0.10}Zr_{0.10}Nb_{0.25}$ (2.60 wt.%) alloys was higher than other materials such as the *bcc* alloy Ti-V-Cr with 1.8 wt.% and other intermetallics like TiFe and $LaNi_5$ with a reversible capacity during cycling of 1.89 wt.% and 1.7 wt.%, respectively [11].

The loss of the hydrogen absorption capacity during cycling could be due to many different factors which will be categorized as intrinsic and extrinsic factors. First, the intrinsic factors such as: the occurrence of phase disproportionation with a formation of stable monohydride from individual elements such as Ti-H, V-H, small inhomogeneities in the chemical composition [12], the reversibility issues of the cycles by incomplete absorption/desorption, and the decrease of the degree of crystallinity from hydrogen embrittlement.

Moreover, Kim *et al.* reported a study about the degradation of the reversible hydrogen storage capacity of the V-Ti alloys [13]. In this study, it was reported that during the absorption of hydrogen, a *bcc* monohydride will transform to a *fcc* dihydride phase by the stretching of the *bcc* lattice along one of its lattice vectors directions. The simultaneous growth of multiple *fcc* lattice will lead to their intersection and the creation of a lattice mismatch. This results in the formation of many lattice defects such as, dislocations, vacancies, stacking faults, and twin boundaries. Hence, due to many hydrogen absorption/desorption cycles, the tetrahedral interstitial sites will experience strong distortions, where they can no longer occupy hydrogen atoms resulting in the degradation of the reversible hydrogen storage capacity.

Second, the extrinsic factors could be impurities as contaminants from the vacuum or gas (N_2, O_2, and CO + CO_2...)[14] affecting the samples surface by oxidation or adsorption of hydrocarbons leading to inhibit the catalytic dissociation of H_2 and affecting the hydrogen diffusion in the structure.

Further investigations on the microstructure and chemical homogeneity were conducted by SEM-EDS on the samples of $Ti_{0.30}V_{0.25}Cr_{0.10}Zr_{0.10}Nb_{0.25}$ and $Ti_{0.30}V_{0.25}Mn_{0.10}Zr_{0.10}Nb_{0.25}$ HEAs following 20 absorption/desorption cycles (figure 4.13.a-b). Both BSE images show the effect of hydrogen embrittlement on the Cr and Mn containing alloys after 20 cycles of hydrogen absorption/desorption. It is a clear formation of multiple cracks when comparing the as-cast samples of $Ti_{0.30}V_{0.25}Cr_{0.10}Zr_{0.10}Nb_{0.25}$ and $Ti_{0.30}V_{0.25}Mn_{0.10}Zr_{0.10}Nb_{0.25}$ alloys (chapter 3, figure 3.2.e-f). Nevertheless, the EDS chemical mapping of Cr and Mn containing alloys after hydrogen cycling showed similar homogeneity as both as-cast samples. Interestingly, after hydrogen cycling of the $Ti_{0.30}V_{0.25}Cr_{0.10}Zr_{0.10}Nb_{0.25}$, there are dendritic regions present in the sample and the chemical mapping of the alloy showed the same variation: Nb rich regions (dendritic), Zr rich regions (interdendritic), and the overall composition is close to the nominal one (figure 4.13.a). Similarly, the analysis of the $Ti_{0.30}V_{0.25}Mn_{0.10}Zr_{0.10}Nb_{0.25}$ sample after hydrogen cycling showed the same chemical homogeneity of the as-cast material (figure 4.13.b). The difference between the Cr and Mn containing samples is the smaller grain sizes of the cycled $Ti_{0.30}V_{0.25}Mn_{0.10}Zr_{0.10}Nb_{0.25}$, this hints to the high decrepitation on the sample from hydrogen absorption/desorption cycles.

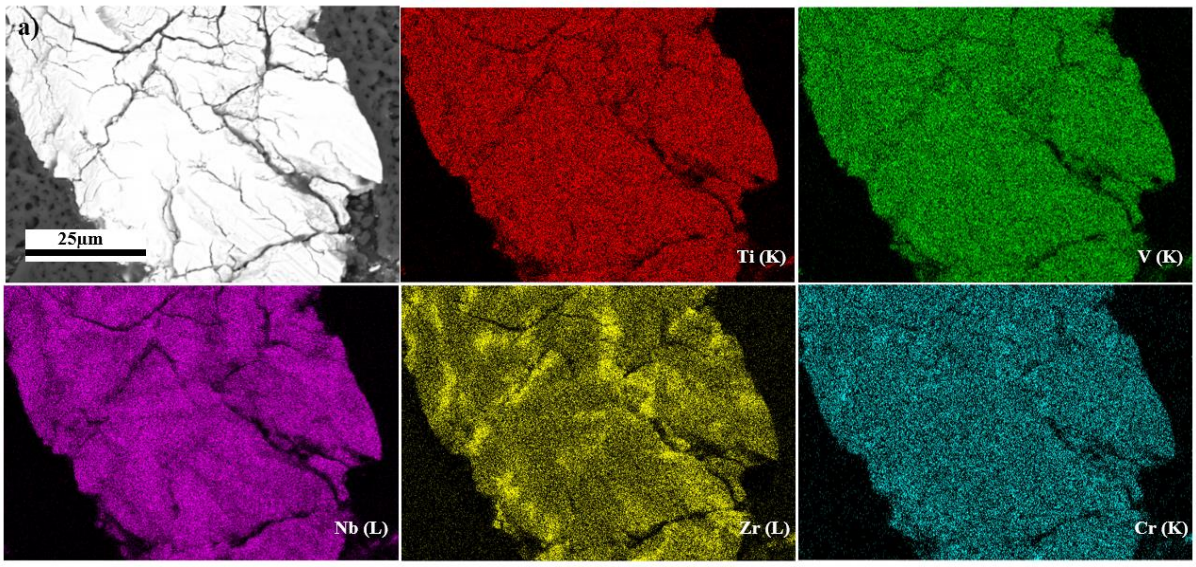

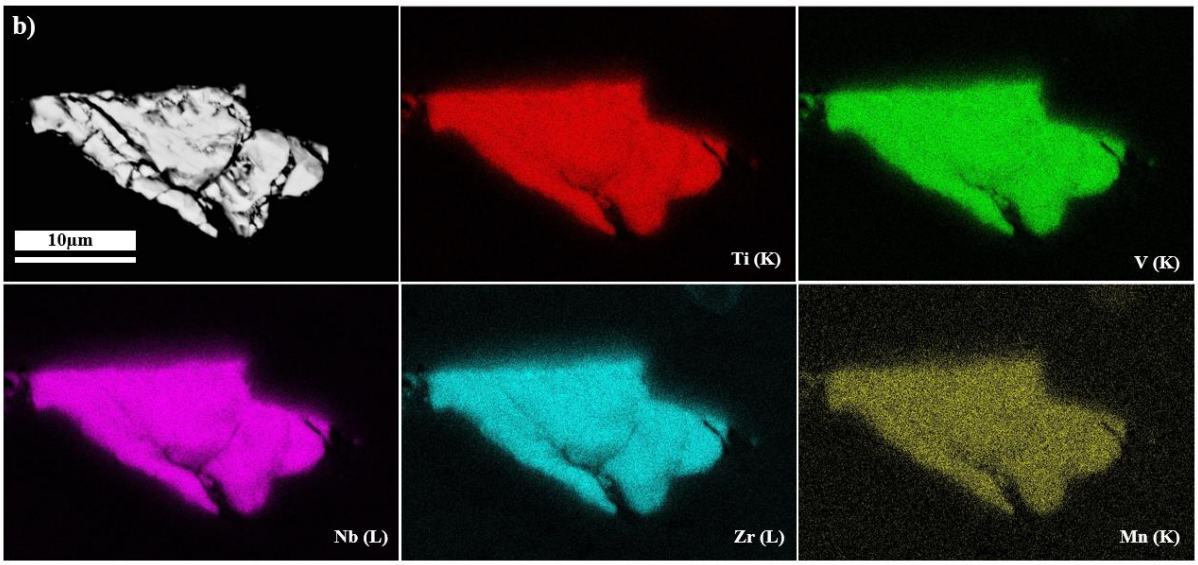

Figure 4.13. BSE image and EDS mapping analysis of $Ti_{0.30}V_{0.25}Cr_{0.10}Zr_{0.10}Nb_{0.25}$ (a) and $Ti_{0.30}V_{0.25}Mn_{0.10}Zr_{0.10}Nb_{0.25}$ (b) alloys after 20 hydrogen absorption/desorption cycles.

4.6 Conclusions

In the present chapter, an in-depth investigation was conducted on the hydrogen sorption properties of $Ti_{0.30}V_{0.25}Cr_{0.10}Zr_{0.10}Nb_{0.25}$ and $Ti_{0.30}V_{0.25}Mn_{0.10}Zr_{0.10}Nb_{0.25}$ HEAs.

Using *ex-situ* neutron diffraction, the occupation of hydrogen/deuterium was determined to be in the tetrahedral interstitial sites of the *fcc* deuterides $Ti_{0.30}V_{0.25}Cr_{0.10}Zr_{0.10}Nb_{0.25}D_2$ and $Ti_{0.30}V_{0.25}Mn_{0.10}Zr_{0.10}Nb_{0.25}D_2$.

The PCI measurements at several temperatures showed a two-step reaction of the HEAs containing Cr and Mn with hydrogen. Moreover, the Van't Hoff calculations allowed the determination of the enthalpy and entropy of the hydride formation which were close to other similar hydrides.

For an in depth investigation, the effect of (de)hydrogenation on the crystalline structure was studied on the $Ti_{0.30}V_{0.25}Cr_{0.10}Zr_{0.10}Nb_{0.25}$ and $Ti_{0.30}V_{0.25}Mn_{0.10}Zr_{0.10}Nb_{0.25}$ HEAs by *ex-situ* SR-XRD. The investigation confirmed the existence of two phase transitions following these steps: *fcc* dihydride ↔ *bcc* monohydride ↔ *bcc* desorbed phase.

Succeeding the PCI measurements and the SR-XRD characterization of the hydrides, two *in-situ* investigations using neutron diffraction and SR-XRD were conducted. The study showed full reversibility of the present studied HEAs during hydrogen/deuterium desorption.

Finally, the hydrogen cycling properties of $Ti_{0.30}V_{0.25}Cr_{0.10}Zr_{0.10}Nb_{0.25}$ and $Ti_{0.30}V_{0.25}Mn_{0.10}Zr_{0.10}Nb_{0.25}$ HEAs were studied and compared with the parent alloy $Ti_{0.325}V_{0.275}Zr_{0.125}Nb_{0.275}$. The reversible capacity of the quaternary alloy was upgraded after the 10 at.% addition of Cr and Mn. The effect of adding *3d M* elements to the quaternary alloy showed upgraded performances such as the higher capacity of absorption and better stabilization during cycling.

Hence, the interest will be to investigate the difference between the addition of *3d* elements (Cr and Mn) and the Mo as a *4d M* element to the quaternary alloy $Ti_{0.325}V_{0.275}Zr_{0.125}Nb_{0.275}$ regarding the phase transition, the hydrogen performances at high temperatures, and the cycling properties.

References

[1] J. Montero, G. Ek, M. Sahlberg, C. Zlotea, Improving the hydrogen cycling properties by Mg addition in Ti-V-Zr-Nb refractory high entropy alloy, Scripta Materialia. 194 (2021) 113699. https://doi.org/10.1016/j.scriptamat.2020.113699.

[2] M.M. Nygård, Ø.S. Fjellvåg, M.H. Sørby, K. Sakaki, K. Ikeda, J. Armstrong, P. Vajeeston, W.A. Sławiński, H. Kim, A. Machida, Y. Nakamura, B.C. Hauback, The average and local structure of TiVCrNbDx (x=0,2.2,8) from total scattering and neutron spectroscopy, Acta Materialia. 205 (2021) 116496. https://doi.org/10.1016/j.actamat.2020.116496.

[3] S. Bellini, Y. Sun, F. Gallucci, A. Caravella, Thermodynamic Aspects in Non-Ideal Metal Membranes for Hydrogen Purification, Membranes. 8 (2018) 82. https://doi.org/10.3390/membranes8030082.

[4] A. Bouzidi, L. Laversenne, V. Nassif, E. Elkaim, C. Zlotea, Hydrogen Storage Properties of a New Ti-V-Cr-Zr-Nb High Entropy Alloy, Hydrogen. 3 (2022) 270–284. https://doi.org/10.3390/hydrogen3020016.

[5] A. Bouzidi, L. Perrière, E. Elkaim, L. Laversenne, V. Nassif, G. Vaughan, C. Zlotea, Exploring the Hydrogen Sorption Capabilities of a Novel Ti-V-Mn-Zr-Nb High-Entropy Alloy, Inorganics. 11 (2023) 186. https://doi.org/10.3390/inorganics11050186.

[6] G. Ek, M.M. Nygård, A.F. Pavan, J. Montero, P.F. Henry, M.H. Sørby, M. Witman, V. Stavila, C. Zlotea, B.C. Hauback, M. Sahlberg, Elucidating the Effects of the Composition on Hydrogen Sorption in TiVZrNbHf-Based High-Entropy Alloys, Inorg. Chem. 60 (2021) 1124–1132. https://doi.org/10.1021/acs.inorgchem.0c03270.

[7] B.H. Silva, C. Zlotea, Y. Champion, W.J. Botta, G. Zepon, Design of TiVNb-(Cr, Ni or Co) multicomponent alloys with the same valence electron concentration for hydrogen storage, Journal of Alloys and Compounds. 865 (2021) 158767. https://doi.org/10.1016/j.jallcom.2021.158767.

[8] R. Griessen, N. Strohfeldt, H. Giessen, Thermodynamics of the hybrid interaction of hydrogen with palladium nanoparticles, Nature Mater. 15 (2016) 311–317. https://doi.org/10.1038/nmat4480.

[9] J. Montero, G. Ek, L. Laversenne, V. Nassif, G. Zepon, M. Sahlberg, C. Zlotea, Hydrogen storage properties of the refractory Ti–V–Zr–Nb–Ta multi-principal element alloy, Journal of Alloys and Compounds. 835 (2020) 155376. https://doi.org/10.1016/j.jallcom.2020.155376.

[10] J. Montero, C. Zlotea, G. Ek, J.-C. Crivello, L. Laversenne, M. Sahlberg, TiVZrNb Multi-Principal-Element Alloy: Synthesis Optimization, Structural, and Hydrogen Sorption Properties, Molecules. 24 (2019) 2799. https://doi.org/10.3390/molecules24152799.

[11] E. Burzo, ed., Hydrogen Storage Materials, Springer Berlin Heidelberg, Berlin, Heidelberg, 2018. https://doi.org/10.1007/978-3-662-54261-3.

[12] S. Selvaraj, A. Jain, S. Kumar, T. Zhang, S. Isobe, H. Miyaoka, Y. Kojima, T. Ichikawa, Study of cyclic performance of V-Ti-Cr alloys employed for hydrogen compressor, International Journal of Hydrogen Energy. 43 (2018) 2881–2889. https://doi.org/10.1016/j.ijhydene.2017.12.159.

[13] H. Kim, K. Sakaki, H. Ogawa, Y. Nakamura, J. Nakamura, E. Akiba, A. Machida, T. Watanuki, T. Proffen, Origin of Degradation in the Reversible Hydrogen Storage Capacity of V1–xTix Alloys from the Atomic Pair Distribution Function Analysis, J. Phys. Chem. C. 117 (2013) 26543–26550. https://doi.org/10.1021/jp408766r.

[14] Hydrogène 6.0 Scientifique | Webshop Linde France – Commander vos gaz industriels en ligne, (n.d.). https://www.linde-gas.fr/shop/fr/fr-ig/hydrog%C3%A8ne-60-scientifique-p-hydrog%C3%A8ne-60-scientifique (accessed June 19, 2023).

CHAPTER V

Hydrogen sorption properties of $Ti_{0.30}V_{0.25}Zr_{0.10}Nb_{0.25}Mo_{0.10}$

Chapter 5. Hydrogen sorption properties of $Ti_{0.30}V_{0.25}Zr_{0.10}Nb_{0.25}Mo_{0.10}$

The last investigated HEA in this project is $Ti_{0.30}V_{0.25}Zr_{0.10}Nb_{0.25}Mo_{0.10}$. The purpose in this chapter is to evaluate the effect of 10 at.% addition of Mo to the quaternary alloy $Ti_{0.325}V_{0.275}Zr_{0.125}Nb_{0.275}$. As already mentioned in chapter 3, the $Ti_{0.30}V_{0.25}Zr_{0.10}Nb_{0.25}Mo_{0.10}$ alloy was only studied regarding its hydrogen absorption capacity at room temperature, as-cast/dihydride phase structures together with the temperature of desorption (from TDS).

In the present chapter, the occupation of hydrogen/deuterium atoms in the lattice of the Mo containing hydride, the structural reversibility during hydrogen/deuterium desorption, and the cycling properties will be investigated and compared against the parent alloy $Ti_{0.325}V_{0.275}Zr_{0.125}Nb_{0.275}$.

5.1 Hydrogen/Deuterium occupation in the lattice

An *ex-situ* neutron diffraction investigation was performed on a deuterated sample $Ti_{0.30}V_{0.25}Zr_{0.10}Nb_{0.25}Mo_{0.10}D_2$ to characterize the phase structure and the occupation of deuterium atoms inside the deuteride lattice. The *ex-situ* neutron diffraction pattern was performed by loading the $Ti_{0.30}V_{0.25}Zr_{0.10}Nb_{0.25}Mo_{0.10}D_2$ sample into a vanadium can while the measurement was conducted at room temperature.

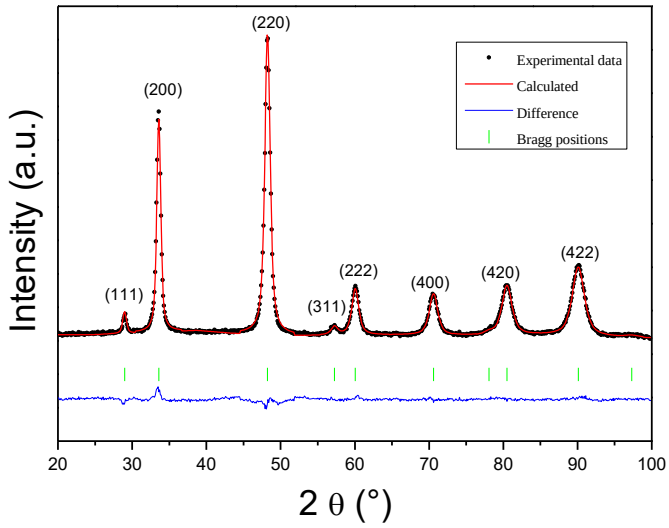

Figure 5.1. Neutron diffraction patterns (λ= 1.2858 Å) of $Ti_{0.30}V_{0.25}Zr_{0.10}Nb_{0.25}Mo_{0.10}D_2$ and the corresponding Rietveld analysis.

Figure 5.1 illustrates the *ex-situ* diffraction pattern of $Ti_{0.30}V_{0.25}Zr_{0.10}Nb_{0.25}Mo_{0.10}D_2$ together with the corresponding Rietveld refinement. The deuterated sample crystallizes in a single-phase *fcc* lattice ($Fm\bar{3}m$). For comparison purposes, in table 5.1 are listed all the *fcc* lattice parameters obtained from SR-XRD, *ex-situ* neutron diffraction, and PDF.

Sample	***fcc* lattice parameter (Å)**		
	SR-XRD	neutron diffraction	PDF
$Ti_{0.30}V_{0.25}Zr_{0.10}Nb_{0.25}Mo_{0.10}H_2$	4.459 (1)	-	4.467 (1)
$Ti_{0.30}V_{0.25}Zr_{0.10}Nb_{0.25}Mo_{0.10}D_2$	-	4.450 (1)	-

Table 5.1. The *fcc* lattice parameter of $Ti_{0.30}V_{0.25}Zr_{0.10}Nb_{0.25}Mo_{0.10}H_2$ and $Ti_{0.30}V_{0.25}Zr_{0.10}Nb_{0.25}Mo_{0.10}D_2$ obtained from SR-XRD, neutron diffraction, and PDF analysis.

The lattice parameter of the *fcc* phase (from dihydride/dideuteride samples) are in good agreement with a slight difference when comparing the SR-XRD and neutron diffraction against the PDF analysis. Furthermore, the neutron diffraction is a technique of characterization that provides data which allows the determination of the deuterium position in the deuteride lattice.

Using Rietveld analysis on the *ex-situ* neutron diffraction pattern, the deuterium atoms were located in the tetrahedral interstitial sites ($^1/_4$; $^1/_4$; $^1/_4$) of the *fcc* lattice (see figure 4.2). The same interstitial preferential occupation was found for the quaternary alloy $Ti_{0.325}V_{0.275}Zr_{0.125}Nb_{0.275}$ [1] as well as the Cr and Mn containing HEAs. Furthermore, this characterization is in a good agreement with previous HEA findings [2–5].

5.2 Pressure-Composition-Isotherms at different temperatures

In chapter 3, the PCI measurement at 25°C on $Ti_{0.30}V_{0.25}Zr_{0.10}Nb_{0.25}Mo_{0.10}$ alloy showed a single plateau pressure at very low pressure. The interest in this section is to study the effect of temperature on the PCI profile for the purpose of obtaining thermodynamic information. Hence, multiple PCIs were measured at higher temperatures from 75°C to 300°C (figure 5.2).

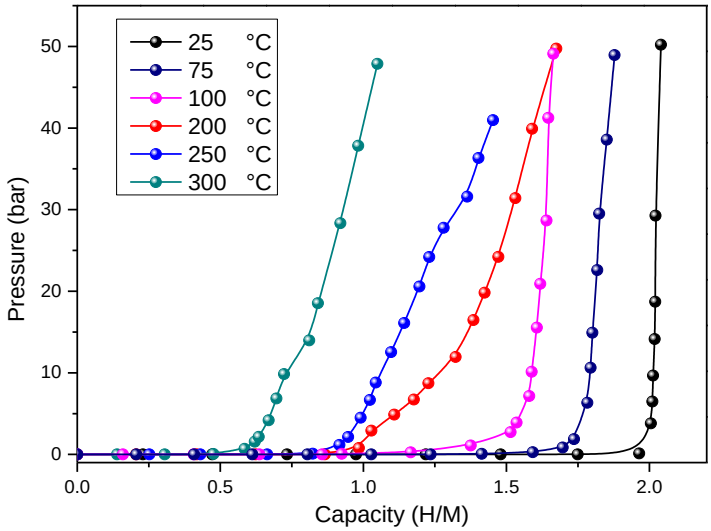

Figure 5.2. Pressure-composition isotherms of the $Ti_{0.30}V_{0.25}Zr_{0.10}Nb_{0.25}Mo_{0.10}$ alloy at 25°C, 75°C, 100°C, 200°C, 250°C, and 300°C.

All the PCI measurements from 25°C to 300°C are plotted in figure 5.2. All the PCIs present the same type of profile: one plateau at very low equilibrium non measurable pressure (below the range of the pressure gauge). As expected, the capacity decreases with the increase of the temperature. However, the equilibrium plateau pressure didn't increase in the measurable range. Similar PCI profiles measured at high temperatures were found in several other HEA studies [6,7].

The PCI measurements did not allow the obtention of thermodynamic properties of the hydride formation (ΔH_{abs}, ΔS_{abs}). Hence, to clarify the phase transition and the stability of the

hydride phase, an investigation of the hydrogenation effect on the structural properties will be conducted.

5.3 Phase transition studies by *in-situ* diffraction

For an in depth study of the effect of dehydrogenation on the structural properties, an *in-situ* thermo-desorption characterization was carried out by neutron diffraction. A deuterated sample $Ti_{0.30}V_{0.25}Zr_{0.10}Nb_{0.25}Mo_{0.10}D_2$ was loaded into a silica tube and linked to a vacuum. Next, the sample was submitted to a constant heating from room temperature to 450°C with a rate of 1°C/min. The collected diffraction data and the pressure readings of the evolved gas are plotted in figure 5.3.

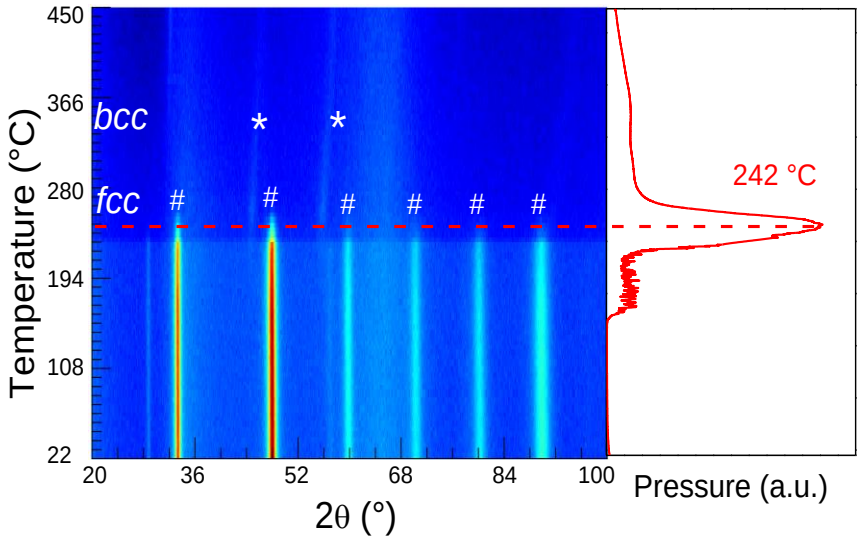

Figure 5.3. *In-situ* neutron diffraction of $Ti_{0.30}V_{0.25}Zr_{0.10}Nb_{0.25}Mo_{0.10}D_2$ (λ=1.28 Å) during deuterium desorption from 22°C to 450°C (left), the pressure reading of the evolved gas (right).

The interest in this experiment is to study the phase transition and the stability of the dihydride phase (dideuteride phase). The pressure profile reveals a starting of the deuterium desorption at around 160°C with a plateau like first desorption event. At 242°C, a main peak of desorption takes place. Finally, another plateau like desorption event is noticed and the amount of the desorbed gas decreases with the increase of the temperature (figure 5.3.right). Figure 5.3.left illustrates the *in-situ* neutron thermo-diffractogram. Starting from 22°C, a clear *fcc* phase is present (marked with #). At 242°C, a phase transition takes place from *fcc* to a desorbed phase that is suggested to be a *bcc* ($Im\bar{3}m$) phase (marked with *). For a temperature higher than 242°C, the *fcc* diffraction signals faded, leaving only weak signals from the desorbed phase. A slight shift is barely seen from the signals of the desorbed *bcc* phase. As already

mentioned in the previous chapter 4, the reason behind the decrease of the intensity of the signals is due to the decrease of the coherent scattering length (b_c) from ~15 fm to 2 fm for the fully deuterated sample and the desorbed sample, respectively. The same behavior is also observed in different HEA compositions [2,3,8]. Nevertheless, the studied HEA might represent a good candidate for an in-core, light water reactor environment [9,10].

The *in-situ* neutron diffraction investigation enabled the determination of the temperature of the phase transition, on the other hand, no information was obtained about the desorbed phase. For a clearer identification of the phase transition during the desorption experiment, an *in-situ* SR-XRD was conducted on a hydrogenated sample $Ti_{0.30}V_{0.25}Zr_{0.10}Nb_{0.25}Mo_{0.10}H_2$ (figure5.4). The SR-XRD patterns were recorded while applying a constant heating temperature rate of 2°C/min from 25°C to 450°C. The hydrogen desorption was done under dynamic secondary vacuum.

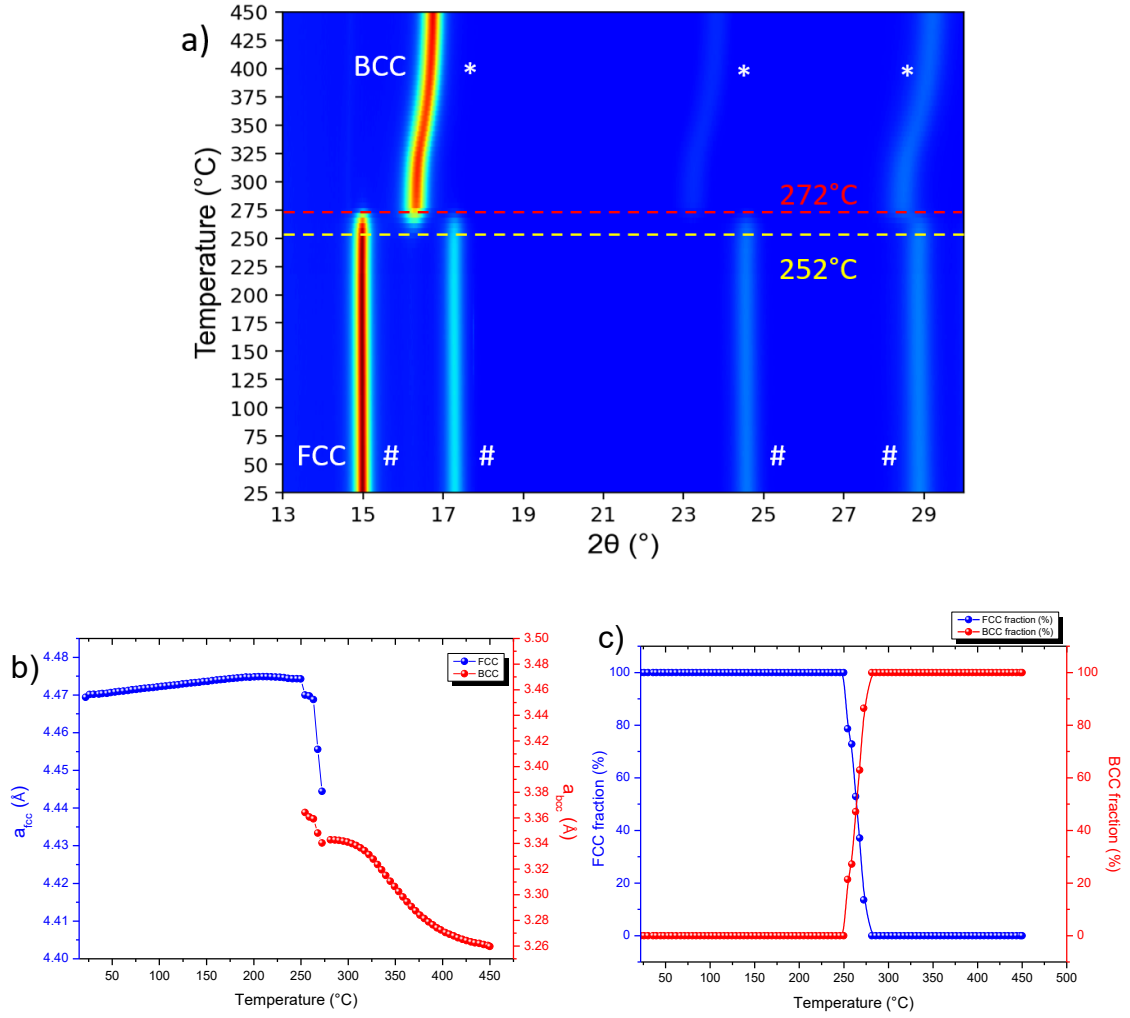

Figure 5.4. In-situ SR-XRD (λ=0.67156 Å) of $Ti_{0.30}V_{0.25}Zr_{0.10}Nb_{0.25}Mo_{0.10}H_2$ during hydrogen desorption from 22°C to 450°C (a), The evolution of the lattice parameters of both the *fcc* and the *bcc* phases (b) together with their phase fraction against the temperature (c).

Starting from the bottom to the top of figure 5.4.a, the *fcc* dihydride phase (marked with #) of the $Ti_{0.30}V_{0.25}Zr_{0.10}Nb_{0.25}Mo_{0.10}H_2$ sample is stable until reaching 252°C. In the interval 252°C-272°C, a phase transition occurs from *fcc* dihydride phase to a *bcc* phase (marked with *). For a temperature higher than 272°C, only the *bcc* phase is identified and the *fcc* phase completely vanishes (figure 5.4.a). In SR-XRD, the temperature of the phase transition 252°C is slightly higher than the one of the *in-situ* neutron diffraction. This is probably due to different experimental conditions, where the rate of the heat treatment is different: 2°C for *in-situ* SR-XRD against 1°C/min for *in-situ* neutron diffraction.

The SR-XRD patterns were all analyzed by Rietveld refinement in order to obtain information about the phases evolution together with their lattice parameters. In figure 5.4.b, from 22°C to 191°C, the *fcc* lattice parameter increases from 4.469 (1) Å to 4.474 (1) Å because of the thermal expansion. From 191.7 °C to 249.8°C, the *fcc* lattice parameter stabilizes at 4.474 (1) Å which is explained by the thermal expansion concomitant with a starting of hydrogen desorption from the sample. A phase transition occurs from 254°C to 272°C, where a coexistence of two phases takes place: a *fcc* and a *bcc* phases. At this interval of temperature, the *fcc* lattice experiences a shrinking from 4.474 (1) Å to 4.444 (1) Å, whereas the *bcc* lattice parameter decreased from 3.364 (1) Å to 3.343 (1) Å and the *bcc* phase fraction increased from 22 % reaching 94% at 276°C. Finally, the *bcc* lattice parameter keeps decreasing reaching 3.259 (1) Å at 450°C, hinting to a desorption of hydrogen after the phase transition. The final analyzed lattice parameter (3.259 (1) Å) is higher than the *bcc* lattice parameter of the as-cast material (3.240 (3) Å) probably because of the thermal expansion at 450°C.

The quaternary parent alloy $Ti_{0.325}V_{0.275}Zr_{0.125}Nb_{0.275}$ showed the same single phase transition, suggesting that the 10 at.% addition of Mo did not affect the nature of the initial nor the hydride phase [2]. Interestingly, both *in-situ* investigations (neutron diffraction and SR-XRD) showed that during the desorption of the Mo containing hydride a phase transition occurs from a *fcc* dihydride to a *bcc* phase. These findings are in agreement with previous reported studies [2,3,11,12].

The conducted investigation of hydrogen absorption/desorption demonstrated that the $Ti_{0.30}V_{0.25}Zr_{0.10}Nb_{0.25}Mo_{0.10}$ HEA have a complete structural reversibility as follows: *fcc* dihydride ↔ *bcc* phase. Interestingly, these findings demonstrated that the HEA series $Ti_{0.30}V_{0.25}Zr_{0.10}Nb_{0.25}M_{0.10}$ (*M* = Cr, Mn, and Mo) have the same phase transition as identified by both *in-situ* SR-XRD and neutron diffraction. However, the temperature of the phase transition is different for the three studied alloys. In fact, the addition of Mo to the parent alloy

$Ti_{0.325}V_{0.275}Zr_{0.125}Nb_{0.275}$ showed a decrease 270°C to 242°C during the *in-situ* neutron diffraction investigation, whereas the Mn addition increased the temperature from 270°C to 280°C and the Cr addition decreased it by around 10°C (shown in chapter 4). Following the confirmation of the structural reversibility upon hydrogen absorption/desorption, the following section will be dedicated for investigating the hydrogen cycling properties of the $Ti_{0.30}V_{0.25}Zr_{0.10}Nb_{0.25}Mo_{0.10}$ HEA.

5.4 Hydrogen cycling performances

The hydrogen cycling properties of the $Ti_{0.30}V_{0.25}Zr_{0.10}Nb_{0.25}Mo_{0.10}$ alloy were measured by the following conditions: for the absorption the sample was subjected to a single dose of hydrogen with a final pressure ≈ 25 bar at 25°C, whereas the desorption was carried out by heating the sample to 450°C for 10 h under dynamic vacuum.

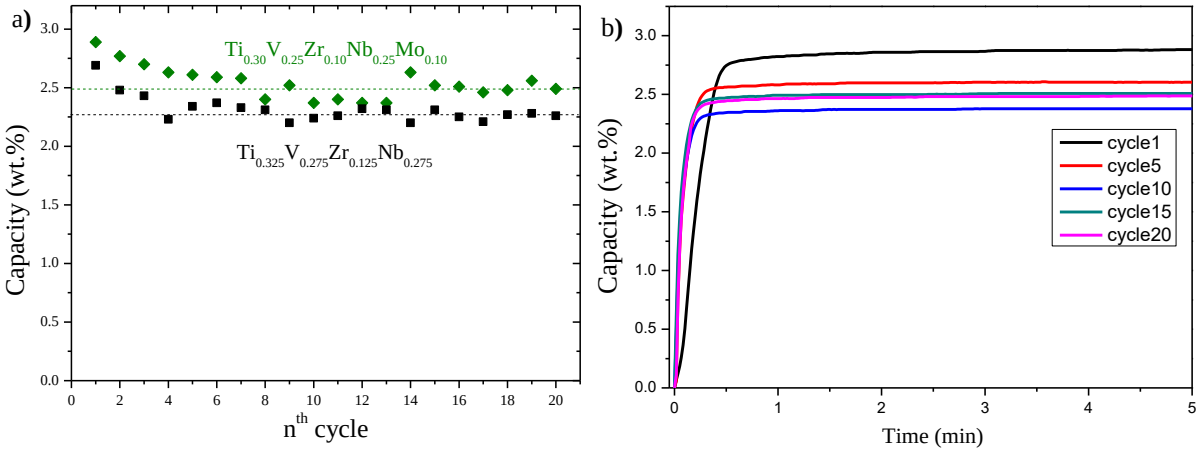

Figure 5.5. Evaluation of the hydrogen absorption capacity of $Ti_{0.30}V_{0.25}Zr_{0.10}Nb_{0.25}Mo_{0.10}$ and $Ti_{0.325}V_{0.275}Zr_{0.125}Nb_{0.275}$ alloys (a), kinetics of 1, 5, 10, 15, and 20 cycles of hydrogen absorption (b).

The results of the hydrogen cycling are plotted in figure 5.5.a. The storage capacity of the $Ti_{0.30}V_{0.25}Zr_{0.10}Nb_{0.25}Mo_{0.10}$ alloy drops from 2.8 wt.% to 2.47 wt.%. A stabilization of the hydrogen absorption capacity is noticed at the 5^{th} cycle and the reversible capacity was around 2.49 wt.% (marked with the green dotted line). Interestingly, the parent alloy $Ti_{0.325}V_{0.275}Zr_{0.125}Nb_{0.275}$ showed similar behavior, the hydrogen storage capacity fades from 2.70 wt.% to 2.33 wt.% at the fifth cycle. A stabilization is reached for the quaternary alloy for the rest of the cycles with a reversible storage capacity of 2.27 wt.% (marked with the black dotted line).

Furthermore, in figure 5.5.b are plotted the kinetics of hydrogen absorption for several cycles of the quinary alloy. Interestingly, at the first cycle, 90% of the full storage capacity is reached only within 30 seconds and becomes faster in the following cycles with only 20 seconds. As seen for the $Ti_{0.30}V_{0.25}Cr_{0.10}Zr_{0.10}Nb_{0.25}$ and $Ti_{0.30}V_{0.25}Mn_{0.10}Zr_{0.10}Nb_{0.25}$ alloys, the kinetics became faster after the first cycle due to the decrepitation of the sample resulting of the creation of fresh large clean surfaces. These surfaces will rapidly dissociate the H_2 molecules into atoms which will diffuse into the smaller grains of the alloy.

The reversible capacity of the $Ti_{0.30}V_{0.25}Zr_{0.10}Nb_{0.25}Mo_{0.10}$ alloy (2.49 wt.%) was better than the Cr-containing alloy (2.44 wt.%), nevertheless, the 10 at.% addition of Mn showed the best reversible capacity reaching 2.60 wt.% among all the HEAs of this series.

As seen in chapter 4, due to multiple hydrogen cycles, the sample could be affected by decrepitation and embrittlement. Thus, a microstructural investigation was conducted in order to analyze the state of the $Ti_{0.30}V_{0.25}Zr_{0.10}Nb_{0.25}Mo_{0.10}$ alloy after 20 cycles (absorption/desorption).

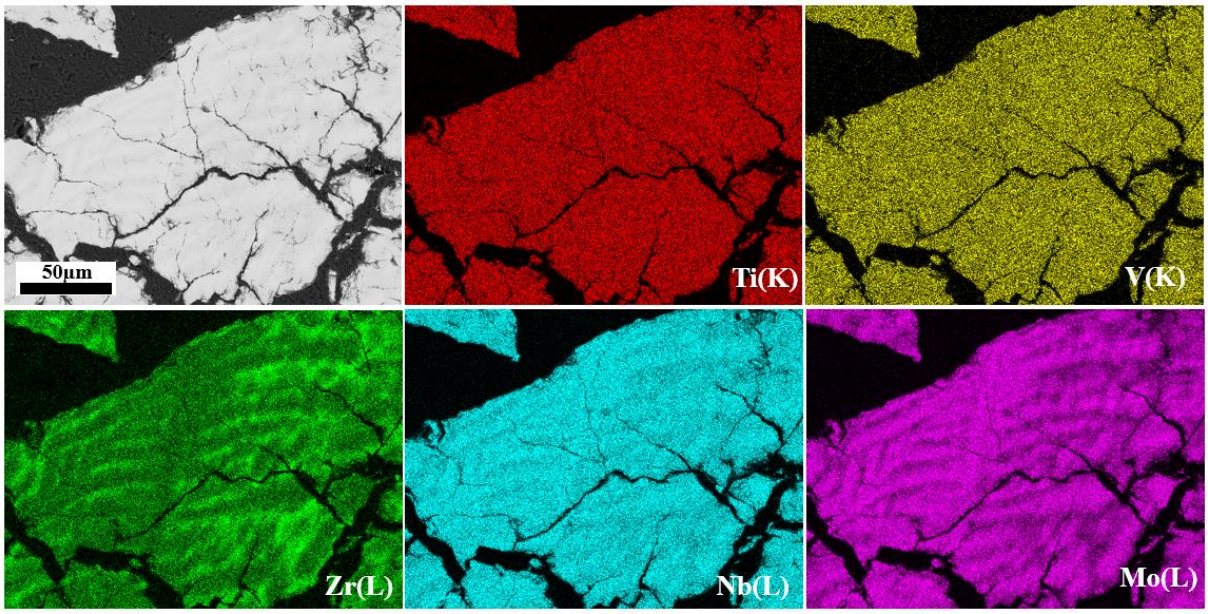

Figure 5.6. BSE image and EDS mapping analysis of $Ti_{0.30}V_{0.25}Zr_{0.10}Nb_{0.25}Mo_{0.10}$ HEA after 20 hydrogen absorption/desorption cycles.

Figure 5.6 illustrates the BSE and EDS analysis carried out on the sample after 20 cycles of hydrogen absorption /desorption. The BSE image presents a homogeneous phase throughout a section of the analyzed material, moreover, some number of cracks and fissures appeared after hydrogen cycling which wasn't the case for the as-cast (SEM of the as-cast shown in chapter 3). Next, an EDS analysis was performed on the sample after cycling to analyze the chemical

composition. The analysis revealed that the sample contained the same dendritic regions as already seen for the as-cast sample (shown in chapter 3). The dendritic regions are rich with Nb and Mo, whereas the interdendritic regions are rich with Zr, and Ti and V are well distributed in both regions. Nevertheless, the overall chemical analysis showed a composition very close to the nominal one and there is no evidence of a phase segregation or decomposition after 20 cycles of rehydrogenation.

Following the microstructure investigation, an XRD was performed on the sample of 20 cycles to assess the effect of the hydrogen cycling on the crystalline structure. Figure 5.7 illustrates the XRD pattern of the $Ti_{0.30}V_{0.25}Zr_{0.10}Nb_{0.25}Mo_{0.10}$ before and after hydrogen cycling.

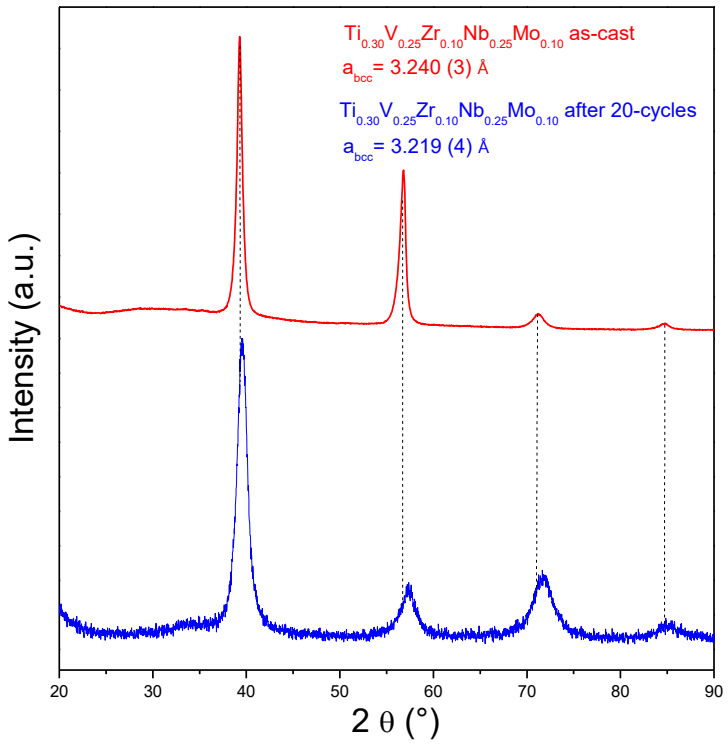

Figure 5.7. XRD patterns of $Ti_{0.30}V_{0.25}Zr_{0.10}Nb_{0.25}Mo_{0.10}$ before and after 20 hydrogen cycles.

The Rietveld refinement analysis revealed that the Mo-containing alloy recovered the same initial *bcc* phase of the as-cast material. The lattice parameter of the cycled material was a_{bcc}= 3.219 (4) Å. Interestingly, the lattice parameter of the cycled alloy was slightly smaller than the lattice parameter of the as-cast alloy a_{bcc}= 3.240 (3) Å. Moreover, the peaks of the cycled material were broad when compared to the initial as-cast material. Hence a comparison

between the full width at half maximum (FWHM) of the cycled and as-cast samples was performed and the results are listed in table 5.2.

	As-Cast		**After 20-Cycles**	
a (Å)	3.240 (3)		3.219 (4)	
Miller Indices	**2θ (°)**	**FWHM (°)**	**2θ (°)**	**FWHM (°)**
(110)	39.54	0.642	39.57	1.286
(200)	57.21	1.017	57.39	1.620
(211)	71.49	0.993	71.65	2.314

Figure 5.2. Lattice parameter, FWHM of the diffraction peaks for both the as-cast sample and the desorbed sample after 20 cycles.

As listed in table 5.2, the FWHM of the cycled material are larger when compared to those of the as-cast $Ti_{0.30}V_{0.25}Zr_{0.10}Nb_{0.25}Mo_{0.10}$ alloy, which confirms the peak broadening in the XRD of the sample after 20 cycles. This due is to the creation of certain defects (as explained in chapter 4) that take place during several hydrogenation cycles. The defects are formed because of several phase transitions from a *bcc* to a *fcc* hydride phase, where the *bcc* lattice will stretch along its vector directions to transform into a *fcc* lattice. The various *fcc* lattice growth following random directions will result in the formation of a lattice mismatch resulting in the creation of lattice defects such as dislocations, vacancies, and twin boundaries. Therefore, for upgrading the hydrogen cycling performances, one needs to focus on the restriction of the formation of the lattice defects during the hydrogenation process.

5.5 Conclusions

The present chapter investigated the effect of adding a 10 at.% of Mo (*4d M* element) to the quaternary alloy $Ti_{0.325}V_{0.275}Zr_{0.125}Nb_{0.275}$ on the hydrogen sorption properties.

An *ex-situ* neutron diffraction on the $Ti_{0.30}V_{0.25}Zr_{0.10}Nb_{0.25}Mo_{0.10}D_2$ dideuteride revealed that the deuterium/hydrogen atoms occupy the tetrahedral interstitial sites of *fcc* lattice, which is in agreement with Cr and Mn containing HEAs and the parent quaternary alloy $Ti_{0.325}V_{0.275}Zr_{0.125}Nb_{0.275}$.

Several PCI measurements were performed at different temperatures (from 25°C to 300°C) to obtain thermodynamic properties. The hydrogen absorption capacities decreased with the temperature increase, however, no information about the enthalpy and entropy of hydride formation were obtained due to the very low plateau pressures (within the limit of the pressure gauge 10^{-2} bar).

Using both *in-situ* neutron diffraction and SR-XRD, a phase transition was characterized from *fcc* dihydride to a *bcc* desorbed phase for the Mo containing alloy, which was similar to the Cr and Mn containing alloys and the parent alloy $Ti_{0.325}V_{0.275}Zr_{0.125}Nb_{0.275}$. Moreover, the temperature of the phase transition varies depending on the fifth added element, where the temperature decreased from 270 °C to 242°C following the addition of Mo to the quaternary alloy. Moreover, the $Ti_{0.30}V_{0.25}Zr_{0.10}Nb_{0.25}Mo_{0.10}$ showed full reversible reaction with hydrogen.

Finally, the cycling properties of the $Ti_{0.30}V_{0.25}Zr_{0.10}Nb_{0.25}Mo_{0.10}$ HEA were investigated to study the effect of 10 at.% addition of Mo to $Ti_{0.325}V_{0.275}Zr_{0.125}Nb_{0.275}$ alloy. Interestingly, the reversible capacity is increased from 2.27 wt.% to 2.49 wt.% for the $Ti_{0.325}V_{0.275}Zr_{0.125}Nb_{0.275}$ alloy and the $Ti_{0.30}V_{0.25}Zr_{0.10}Nb_{0.25}Mo_{0.10}$ HEA, respectively. Moreover, after 20 cycles of hydrogen absorption/desorption, the microstructure of the cycled sample was investigated revealing numerous cracks and fissures. Nevertheless, the chemical composition remained close to the initial one with a dendritic microstructure and the structure of the cycled sample was similar to the initial *bcc* phase with broadening of the diffraction peaks as a result of the formation of defects during the hydrogen cycling.

References

[1] J.M. Banuelos, Refractory high entropy alloys for hydrogen storage, (n.d.).

[2] J. Montero, G. Ek, L. Laversenne, V. Nassif, G. Zepon, M. Sahlberg, C. Zlotea, Hydrogen storage properties of the refractory Ti–V–Zr–Nb–Ta multi-principal element alloy, Journal of Alloys and Compounds. 835 (2020) 155376. https://doi.org/10.1016/j.jallcom.2020.155376.

[3] J. Montero, G. Ek, M. Sahlberg, C. Zlotea, Improving the hydrogen cycling properties by Mg addition in Ti-V-Zr-Nb refractory high entropy alloy, Scripta Materialia. 194 (2021) 113699. https://doi.org/10.1016/j.scriptamat.2020.113699.

[4] M.M. Nygård, W.A. Sławiński, G. Ek, M.H. Sørby, M. Sahlberg, D.A. Keen, B.C. Hauback, Local order in high-entropy alloys and associated deuterides – a total scattering and Reverse Monte Carlo study, Acta Materialia. 199 (2020) 504–513. https://doi.org/10.1016/j.actamat.2020.08.045.

[5] G. Ek, M.M. Nygård, A.F. Pavan, J. Montero, P.F. Henry, M.H. Sørby, M. Witman, V. Stavila, C. Zlotea, B.C. Hauback, M. Sahlberg, Elucidating the Effects of the Composition on Hydrogen Sorption in TiVZrNbHf-Based High-Entropy Alloys, Inorg. Chem. 60 (2021) 1124–1132. https://doi.org/10.1021/acs.inorgchem.0c03270.

[6] A. Kumar, T.P. Yadav, N.K. Mukhopadhyay, Notable hydrogen storage in Ti–Zr–V–Cr–Ni high entropy alloy, International Journal of Hydrogen Energy. 47 (2022) 22893–22900. https://doi.org/10.1016/j.ijhydene.2022.05.107.

[7] X. Ma, X. Ding, R. Chen, X. Chen, Q. Song, H. Cui, Study on microstructure and the hydrogen storage behavior of a TiVZrNbFe high-entropy alloy, Intermetallics. 157 (2023) 107885. https://doi.org/10.1016/j.intermet.2023.107885.

[8] J. Montero, G. Ek, L. Laversenne, V. Nassif, M. Sahlberg, C. Zlotea, How 10 at% Al Addition in the Ti-V-Zr-Nb High-Entropy Alloy Changes Hydrogen Sorption Properties, Molecules (Basel, Switzerland). 26 (2021). https://doi.org/10.3390/molecules26092470.

[9] Y. Lu, H. Huang, X. Gao, C. Ren, J. Gao, H. Zhang, S. Zheng, Q. Jin, Y. Zhao, C. Lu, T. Wang, T. Li, A promising new class of irradiation tolerant materials: Ti2ZrHfV0.5Mo0.2 high-entropy alloy, Journal of Materials Science & Technology. 35 (2019) 369–373. https://doi.org/10.1016/j.jmst.2018.09.034.

[10] D.J.M. King, High temperature, low neutron cross-section high-entropy alloys in the Nb-Ti-V-Zr system, Acta Materialia. (2019) 12.

[11] A. Bouzidi, L. Laversenne, V. Nassif, E. Elkaim, C. Zlotea, Hydrogen Storage Properties of a New Ti-V-Cr-Zr-Nb High Entropy Alloy, Hydrogen. 3 (2022) 270–284. https://doi.org/10.3390/hydrogen3020016.

[12] A. Bouzidi, L. Perrière, E. Elkaim, L. Laversenne, V. Nassif, G. Vaughan, C. Zlotea, Exploring the Hydrogen Sorption Capabilities of a Novel Ti-V-Mn-Zr-Nb High-Entropy Alloy, Inorganics. 11 (2023) 186. https://doi.org/10.3390/inorganics11050186.

CHAPTER VI

General conclusions and perspectives

Chapter 6. General conclusions and perspectives

The aim of this project is to investigate the hydrogen sorption properties of high entropy alloys. The challenge is to find a guideline to understand the effect of the chemical composition on several criteria such as the hydrogen uptake, the kinetics of absorption at ambient temperature, the desorption properties, the reversibility upon (de)hydrogenation, and the cycling performances. The known strategies are either the addition of multiple elements to a parent alloy or the change of the concentration of the elements for the purpose of upgrading the hydrogen storage properties.

In this project, a novel strategy is proposed to rationalize the effect of chemical composition on the hydrogen sorption properties in a series of HEAs. The idea is to start from a quaternary alloy composed of four refractory elements $Ti_{0.325}V_{0.275}Zr_{0.125}Nb_{0.275}$ and to study the effect of addition of 10% of a fifth element *M* (with *M* = Mg, Al, Cr, Mn, Fe, Co, Ni, Cu, Zn, Mo, and Ta). The main strategy is to minimize the degrees of freedom of the chemical composition with the variation of only the nature of the added fifth element at a fixed stoichiometry $Ti_{0.30}V_{0.25}Zr_{0.10}Nb_{0.25}M_{0.10}$. Hence, this novel methodology allowed the building of correlations between the storage properties of the HEA series with the following empirical parameters: lattice distortion parameter (δ) and the valence electron concentration (VEC).

The main part of this PhD project was focused on the synthesis, the (de)hydrogenation, and the structural and microstructural characterizations of the materials (as-cast/hydrides). Moreover, the obtained results were correlated with the earlier mentioned empirical parameters. The HEAs were synthesized by three methods depending on two criteria: the melting temperature of the added element, the obtention of a single-phase material. Thus, the used methods were arc melting, ball milling under Ar atmosphere, and reactive ball milling under hydrogen atmosphere.

First, the series of $Ti_{0.30}V_{0.25}Zr_{0.10}Nb_{0.25}M_{0.10}$ (where *M* = Al, Cr, Mn, Fe, Co, Ni, Cu, Mo, and Ta) was synthesized by arc melting. As a result, two classes of alloys were identified regarding the phase distribution. The first class of materials is composed of $Ti_{0.30}V_{0.25}Zr_{0.10}Nb_{0.25}M_{0.10}$ alloys with *M* = Al, Cr, Mn, Mo, and Ta which mostly crystallize in a single-phase *bcc* lattice ($Im\bar{3}m$). The microstructural analysis by SEM-EDS confirmed a dendritic microstructure and the overall composition was close to the nominal one for all the synthesized alloys.

The second class of materials is comprising the $Ti_{0.30}V_{0.25}Zr_{0.10}Nb_{0.25}M_{0.10}$ alloys with *M* = Fe, Co, Ni, and Cu. These alloys formed 2 phases: a *bcc* along with *C14* ($MgZn_2$) or *C15* ($MgCu_2$) Laves phases. Thus, another type of method of synthesis was used to obtain single phase *bcc* materials. The ball milling under Ar atmosphere method is an alternative method of synthesis of materials forming intermetallic phases by AM or containing elements with low melting temperatures (Zr and Mg) and high vapor pressure (Mg). Four HEAs with *M* = Fe, Co, Ni, and Cu were successfully synthesized by BM forming a single-phase *bcc* lattice.

The method of synthesis, the calculated δ and VEC, the initial phase and the corresponding hydride phase of all the HEA series are listed in table 6.1.

Alloy	Synthesis	δ(%)	VEC	Initial phase	Hydride phase
$Ti_{0.325}V_{0.275}Zr_{0.125}Nb_{0.275}$	AM	6.0	4.55	*bcc*	*fcc*
$Ti_{0.30}V_{0.25}Zr_{0.10}Nb_{0.25}Mg_{0.10}$	BM	6.6	4.3	*bcc*	*fcc*
$Ti_{0.30}V_{0.25}Zr_{0.10}Nb_{0.25}Al_{0.10}$	AM	5.5	4.4	*bcc*	*bct*
$Ti_{0.30}V_{0.25}Zr_{0.10}Nb_{0.25}Cr_{0.10}$	AM	6.7	4.7	*bcc*	*fcc*
$Ti_{0.30}V_{0.25}Zr_{0.10}Nb_{0.25}Mn_{0.10}$	AM	5.7	4.8	*bcc*	*fcc*
$Ti_{0.30}V_{0.25}Zr_{0.10}Nb_{0.25}Fe_{0.10}$	BM	6.8	4.9	*bcc*	*fcc*
$Ti_{0.30}V_{0.25}Zr_{0.10}Nb_{0.25}Co_{0.10}$	BM	6.7	5.0	*bcc*	*fcc*
$Ti_{0.30}V_{0.25}Zr_{0.10}Nb_{0.25}Ni_{0.10}$	BM	6.7	5.1	*bcc*	*fcc*
$Ti_{0.30}V_{0.25}Zr_{0.10}Nb_{0.25}Cu_{0.10}$	BM	6.4	5.2	*bcc*	*fcc*
$Ti_{0.30}V_{0.25}Zr_{0.10}Nb_{0.25}Zn_{0.10}$	BM	5.9	5.3	*bcc*	*fcc*
$Ti_{0.30}V_{0.25}Zr_{0.10}Nb_{0.25}Mo_{0.10}$	AM	5.7	4.7	*bcc*	*fcc*
$Ti_{0.30}V_{0.25}Zr_{0.10}Nb_{0.25}Ta_{0.10}$	AM	5.5	4.6	*bcc*	*fcc*

Table 6.1. The method of synthesis, the empirical parameters (δ and VEC), the initial formed phase structure with the corresponding hydride phase of the HEA series.

The *bcc* lattice parameter of the quaternary alloy decreased after the addition of Al, Mn, and Mo. Moreover, a correlation was drawn between the *bcc* lattice parameters of the HEA series and the lattice distortion parameter (δ) showing a weak increasing trend. This weakness is due to two factors: first the $Ti_{0.30}V_{0.25}Cr_{0.10}Zr_{0.10}Nb_{0.25}$ HEA contained an impurity affecting the *bcc* lattice parameter and secondly, the peaks of the XRD patterns of the BM materials were broad leading to a decrease of the accuracy of the refined *bcc* lattice parameters.

The RBM method was used to synthesize direct hydrides only for the BM materials. The SEM-EDS analysis showed a homogenous chemical composition for $Ti_{0.325}V_{0.275}Zr_{0.125}Nb_{0.275}$

and $Ti_{0.30}V_{0.25}Zr_{0.10}Nb_{0.25}M_{0.10}$ (*M* = Zn, Cu, Ni, Co, Fe, and Mg). A small impurity of ~ 4% of Fe was measured in all the RBM samples which is caused by a contamination from the friction of the balls and the vial during the milling. Nevertheless, all the synthesized materials crystallize in a *fcc* lattice ($Fm\bar{3}m$).

PCI measurements were conducted on the RBM and AM samples at 25°C demonstrated similar profiles: one plateau of absorption at very low equilibrium pressure which was followed by an ascendant branch in higher pressure. The addition of the elements (*M* = Cr, Mn, Mo, and Ta) to the quaternary parent alloy increased the capacity of hydrogen absorption from 1.75 H/M to 2 H/M which are interesting capacities when compared to those in literature. On the other hand, the Mg, Al, Fe, Co, Ni, and Cu containing HEAs showed lower capacities ranging from 1.1 to 1.6 H/M.

The reason for this diminishing of the capacity was revealed when a correlation between the capacity of hydrogen absorption capacity and the VEC was drawn. In fact, HEAs with VEC<4.9 showed a capacity that is either close to the one of the quaternary alloy or higher, whereas, if VEC $\geq$ 4.9 the hydrogen absorption capacity will decrease drastically. This correlation points out that the addition of elements to an alloy shouldn't be at random and the more the added element participates to fill the unoccupied valence states of the alloy the more the vacant electronic states will decrease.

Following the hydrogenation, all the resulting hydrides were single phase with *fcc* lattice except the Al-containing hydride which adopted a *bct* (I4/mmm) lattice. The latter is a similar structure of the *fcc* lattice with a small expansion on the *c* axis. Moreover, no phase separation or segregation was identified in the structure of the hydrides, hinting to a clear phase transition from an initial phase *bcc* to a *fcc/bct* hydride phase.

A selection of alloys $Ti_{0.30}V_{0.25}Zr_{0.10}Nb_{0.25}M_{0.10}$ (with *M* = Mg, Al, Cr, Mn, and Mo) and $Ti_{0.325}V_{0.275}Zr_{0.125}Nb_{0.275}$ was analyzed by PDF after full hydrogenation. Despite the different chemical compositions of the samples, all the PDF profiles were similar revealing a close local order and the analyzed structures were in agreement with *fcc*/*bct* lattices found by XRD. Furthermore, the PDF analysis of the Mg containing hydride revealed that the sample exhibited some structural defects which are originated from the RBM synthesis.

The thermo-desorption measurements demonstrated that the addition of a fifth element *M* to the quaternary alloy demonstrated a positive effect on the desorption properties by decreasing the T_{onset}, especially for the Al containing alloy where the temperature decreased from 271°C

to 114 °C. Moreover, a correlation was drawn between the T_{onset} against the VEC showing a very clear linear increase. Interestingly, HEAs with low VEC around 4.4 and 4.6, have the lowest T_{onset}. This is in a good agreement for HEAs with high capacity of absorption.

The correlations that have been drawn in this part of the PhD project revealed a guide criterion for the choice of an ideal candidate for an optimal hydrogen storage material, where a HEA with high hydrogen absorption capacity and low temperature of desorption should have low VEC values close to 4.9.

The final part of the PhD project focuses on three materials with the highest hydrogen absorption capacities: $Ti_{0.30}V_{0.25}Zr_{0.10}Nb_{0.25}M_{0.10}$ (with *M* = Cr, Mn, and Mo).

The neutron powder diffraction of the samples containing Cr, Mn, and Mo showed that the deuterium/hydrogen atoms are located in the tetrahedral sites of the *fcc* lattice. Similar findings were reported in several refractory HEAs.

The PCI measurement at 25°C showed only a phase transition from an initial *bcc* to a *fcc* dihydride phase, hence several strategies were implemented to conduct a thorough characterization:

The first strategy is by measuring PCIs at higher temperatures. This method showed that the profiles of the Cr and Mn containing alloys were interesting, where a half of the plateau pressure was observed at high temperatures (200°C-300°C). On the other hand, the $Ti_{0.30}V_{0.25}Zr_{0.10}Nb_{0.25}Mo_{0.10}$ alloy showed no measurable equilibrium plateau pressure at high temperatures. The PCI measurements of the Cr and Mn alloys allowed the determination of the enthalpy and entropy of absorption which suggested a stable hydride formation when compared to similar compositions.

The second strategy is to investigate samples at different stages of hydrogenation for the $Ti_{0.30}V_{0.25}Zr_{0.10}Nb_{0.25}M_{0.10}$ (with *M* = Cr and Mn) alloys. In both materials, the structural investigations demonstrated the existence of two-phase transitions from the as-cast to the dihydride phase as follows: *bcc* desorbed phase ↔ *bcc* monohydride ↔ *fcc* dihydride.

The study of the structural reversibility during desorption was conducted *via in-situ* SR-XRD and neutron diffraction. The investigations on the series $Ti_{0.30}V_{0.25}Zr_{0.10}Nb_{0.25}M_{0.10}$ (with *M* = Cr, Mn, and Mo) HEAs demonstrated a transition from dihydride *fcc* phase to a *bcc* monohydride followed by a transformation of the latter phase to a *bcc* desorbed phase. Furthermore, a full structural reversibility was confirmed for the three investigated HEAs.

The hydrogen cycling properties were upgraded following the addition of *3d* (Cr and Mn) and *4d* (Mo) as compared to the quaternary alloy $Ti_{0.325}V_{0.275}Zr_{0.125}Nb_{0.275}$. During 20 cycles of hydrogen absorption/desorption, the studied materials showed rapid kinetics during hydrogen absorption, a slight fading of the capacity in the first five/six cycles which was followed by a stabilization for the rest of the cycles. The microstructure of the cycled HEAs exhibited several fissures and cracks due to hydrogen embrittlement, nevertheless, the samples exhibited a good homogeneity, and no phase segregation was observed.

The studied alloys in this project showed interesting hydrogen performances, however, there are several properties that are worth mentioning for the purpose of obtaining the ideal candidate for hydrogen storage applications. Therefore, several perspectives could be drawn such as:

1- Prior to the hydrogenation, an activation *via* heat treatment is needed at 350°C under dynamic vacuum which affects the energy efficiency of the hydrogen storage system. For future studies, an investigation on the activation process should be conducted to understand and overcome it.

2- The PCI measurements at ambient conditions showed low equilibrium pressures ($< 10^{-2}$ mbar). Moreover, the studied hydrides were stable, and the hydrogen was only desorbed by raising the temperature. These disadvantages reveal the need to investigate the stability of the hydrides and to increase the equilibrium pressure at room temperature by adding new elements for the purpose of obtaining a material capable of absorbing and desorbing hydrogen close to ambient conditions.

3- A study on the microstructure stability during hydrogen cycling is needed to comprehend the role of the mechanical properties of HEAs. Furthermore, enhancing the mechanical properties will result in limiting the formation of dislocations that may cause the decrease of the reversible capacity during cycling.

4- Lastly, an investigation linking the equilibrium pressure with empirical parameters is needed to understand and depict the role of each element of the HEA in order to tune the stoichiometry and the nature of the constituent elements for targeted operating conditions.

The advantage of the HEAs is the wide range of the chemical combinations and the stoichiometries offering a huge and promising candidate as a hydrogen storage material. The

novel proposed methodology gave several criteria for obtaining HEAs with good hydrogen storage performances.